Title
Automated Experimentation and Machine Learning for Perovskite Photovoltaics

Author
Srivastava, Meghna

Publication Date
2022

Peer reviewed|Thesis/dissertation

Automated Experimentation and Machine Learning
for Perovskite Photovoltaics

By

MEGHNA SRIVASTAVA
THESIS

Submitted in partial satisfaction of the requirements for the degree of

MASTER OF SCIENCE

in

Materials Science & Engineering

in the

OFFICE OF GRADUATE STUDIES

of the

UNIVERSITY OF CALIFORNIA

DAVIS

Approved:

Marina Leite, Chair

Seung Sae Hong

Adam Moule

Committee in Charge

2022

ABSTRACT

As anthropogenic global warming and climate change continues to intensify, it is more important than ever to curb our use of fossil fuels for heat and electricity. The clean energy transition requires investment in photovoltaic (PV) technology to replace unsustainable generation sources and to meet increasing electrification demand. Most currently available PV modules use Si as the light absorber material. Advancements in the manufacturing process of Si solar cells has led to a reduction in cost over the past decade, yet there are still inherent difficulties in the refinement process. Next-generation PV must improve upon Si by maintaining or increasing device efficiency while simplifying manufacturing. Metal halide perovskite solar cells (PSC) have proven to meet these criteria, with >25% efficiency and cost-effective fabrication options such as blade coating and ink jet printing. However, degradation in perovskite materials under several environmental stressors (light, humidity, temperature, bias, and oxygen) precludes commercial adoption. Stability testing of PSC is time-consuming, particularly due to the large compositional space available. As a result, methods to quickly vet the stability of various perovskite compositions are critically needed. My Thesis addresses this open problem by applying automated, *in situ* characterization and machine learning (ML) forecasting to PSC degradation studies.

First, I present a generalized ML roadmap for perovskite PV. I delineate three levels of PSC design and provide examples of ML projects which could accelerate the development process. Next, I design and build a high-throughput setup for *in situ*, environmental photoluminescence (PL) spectroscopy, a technique which requires <2 seconds to acquire data. The system uses a custom chamber containing up to 14 samples and an x-y translation stage

to automatically move from one sample to the next. We select ten $Cs_yFA_{1-y}Pb(Br_xI_{1-x})_3$ perovskite thin films of varied composition and track changes in radiative recombination under repeated 6-hour temperature and rH cycles. Using the high-throughput setup, I obtain 240 PL spectra every hour and 14,000 spectra over the course of a single experiment. The temperature cycling results show increased non-radiative carrier recombination as samples are heated above 23°C. We show that FA-rich perovskites with 10-30% Cs^+ have minimal lattice strain which promotes high structural and thermal stability. During rH cycling, all compositions displayed a PL enhancement with increasing rH as H_2O passivates band gap trap states and suppresses non-radiative recombination. FA-rich films show the greatest PL increases over the course of the rH cycling while Cs-rich films reach a plateau in maximum PL value after 5-10 cycles. Finally, I apply ML models to the datasets and generate forecasts of environment-dependent PL responses. I use linear regression, Echo State Network (ESN), and Auto-Regressive Integrated Moving Average with eXogenous regressors (ARIMAX) algorithms. For the temperature cycling, I attain an average normalized root mean square error (NRMSE) over all compositions of 24.4% (linear regression), 16.6% (ESN), and 7.3% (ARIMAX) for prediction windows extending 70 hours into the future. For the rH cycling, NRMSE values of 72.5% (linear regression) and 44.0% (ESN) indicate difficulty in tracking long-term changes over a 50-hour window. Using ARIMAX with seasonality components, I achieve an error of only 10.3%, demonstrating the algorithm's capability to model complex, non-linear data from varied perovskite compositions. My high-throughput characterization results and accurate time series forecasts illustrate the potential of data-centric approaches for perovskite stability investigations and showcase the promise of automation, data science, and ML as tools to drive PSC commercialization.

Acknowledgements

The support from my mentors, collaborators, colleagues, friends, and family have been absolutely essential to the work described in this thesis. I would like to first thank my advisor, Prof. Marina S. Leite, for her consistent inspiration and enthusiasm. I am extremely grateful for the opportunity to work on cutting-edge problems in materials science while having the agency to lead experiments. My experience in your lab has strengthened my ability as a researcher, engineer, and scientific communicator immensely. I would also like to thank the members of my thesis committee: Prof. Seung Sae Hong and Prof. Adam Moule, for sharing their ideas and feedback.

I thank my fellow Leite Lab members: Ece Deniz, Margaret Duncan, Richa Lahoti, and Peifen Lyu, for your camaraderie, empathy, and support these past two years. Thank you also to my more recent labmates: Mansha Dubey and Abigail Herring, for helping me organize my thoughts (and my code). You are all capable and intelligent – I know you will continue to excel through graduate school and beyond. To Dr. Tao Gong and Dr. Mariama Dias: thank you so much for your assistance and feedback with the machine learning parts of this work. Your questions and insights have been indispensable. I would like to express special thanks to Dr. John Howard for laying the groundwork for this research, and for always making time to answer my questions and share your expertise. You have helped me countless times.

To our collaborators in the Correa-Baena Lab at Georgia Institute of Technology: Yu An, Sanggyun Kim, and Prof. Juan-Pablo Correa-Baena, thank you for your excellent work in fabricating the samples used in this thesis, and for your insights and discussions.

Many faculty and staff members at UC Davis have offered their kind assistance through all stages of my graduate school experience. Thank you to the staff at the Center for Nano-MicroManufacturing (CNM2), especially Siwei Li, Paula Lee, and Ryan Anderson. I would also like to thank Dave Hemer from the MPS Machine Shop for his help in designing and fabricating our sample chamber. I appreciate all the time and thought you invested in this project. I thank all of the University staff who assisted with logistics, payroll, and more. From the MSE department: Grace Woods, Ryan Gorsiski, Gwen Caramanica, Susan Lopez, and Dr. Bill Doering. From outside the department: Dave Griffiths, Shannon Chee, Yvette Garcia, and Dr. Bai-Yin Chen. I would also like to thank MSE department faculty members Prof. Sabyasachi Sen and Prof. Yayoi Takamura for their mentorship and support.

It is extremely important that I thank and acknowledge my previous mentors for first introducing me to research, materials science, and hands-on engineering: Prof. Jin Suntivich, Dr. John Eom, Prof. Lara Estroff, Dr. Lisa Thompson, Prof. Michael O. Thompson, Gibran A el-Sulayman, Prof. M. Stanley Whittingham, Dr. Natasha Chernova, and Dr. Carrie Siu.

I graciously acknowledge the funding agencies and organizations who have awarded me with financial support so that I could accomplish and complete this thesis: the National Science Foundation (NSF) grant number 2023974, the NSF Graduate Research Fellowship (grant 2036201) (2021-2022), the UC Davis Department of Materials Science & Engineering, the UC Davis Towards Outstanding Postgraduate Students (TOPS) Fellowship (2019-2020), the UC Davis Graduate Assistance in Areas of National Need (GAANN) Fellowship (2019-2020), the UC Davis GEMS Fellowship (2020-2021), and the UC Davis Graduate Studies Travel Award (Fall 2021). Other monetary awards include: MRS Best Poster Award (conference-wide), MRS Best Poster Award (Symposium F.EL08/S.CT02).

I thank all of my wonderful friends for their support, encouragement, and love. I want to especially acknowledge Rachel Diao (for listening to me and sending pictures of cute animals whenever I needed it – i.e., always), Lav Aprameya (for your endless empathy and good advice), Matt Boudreau (for being a bigger nerd than I am), Amber Pasha (for your humor and kindness), Megan Laney (also, for being a bigger nerd than I am), and Hannah Allison (for sticking by me, no matter what, for the past 15 years).

It is difficult, perhaps impossible, for me to fully express my gratitude to my family, but I will do my best to try. Thank you to my brothers, Shiven and Rishie, for loving me, goofing around with me, and always being there for me. I would also like to thank my Nani and Dadi for their constant love and interest in my studies. And, although they will never read this, I thank the goodest boys in the family, Finn and Simon, for their ineffable contributions. To my parents: thank you for listening and helping me at every step along the way. Your unwavering support and belief in me means more than I can say. Finally, to Nina McCloud: you have changed and improved my life in countless ways, which I won't get into here since I'm already pushing the mushiness quota as it is. I'll just say that you've made the bad times bearable and the good times wonderful, and that I am inspired every day by your courage, your empathy, and your stubbornness. I'm so excited to start a new chapter with you (and Finn) (and Subaru). I'll close by dedicating my thesis to all the individuals mentioned above. I could not have done this without you.

Meghna Srivastava

February 2022

Davis, CA

Table of Contents

List of Tables

List of Figures

Chapter 1: Introduction to Perovskite Photovoltaics

1.1 Motivation for photovoltaic development

The realities of global warming and climate change necessitate a rapid, efficient transition away from fossil fuels towards purely renewable energy sources. Global leaders have pledged transitions to net zero carbon dioxide emissions in the near future, with a common target year of 2050 and some targets as early as 2030.[1] Meeting these goals will require significant advancements in photovoltaic (PV) technology and deployment. In the United States, solar accounted for 3% of total energy generation in 2020. To meet the 2050 target, the US Department of Energy predicts that 20% of energy must be provided by PV.[2] Therefore, new PV technology must be efficient, inexpensive, and possess a range of deployment options including rooftop, ground-mounted, vehicle-mounted, and solar windows. The current state-of-the-art solar modules use silicon as the light absorber material, with monocrystalline, polycrystalline, and thin-film Si solar together accounting for >70% of the total solar market share.[3] However, Si is defect-sensitive and wafer production for high-efficiency cells requires expensive refinement through the Czochralski (CZ) process. Additionally, most Si solar modules are brittle and rigid, limiting the scope of their deployment. Novel materials with simple fabrication methods, comparable efficiency, and greater strain-tolerance could thus have an important niche in photovoltaic deployment over the coming decades.

1.2 Progress and challenges in perovskite solar cells

Metal halide perovskite solar cells (PSC) have attracted interest as a high-efficiency, low-cost alternative to Si photovoltaics. Additionally, perovskite devices are fabricated using cost-effective, scalable methods such as blade coating, ink jet printing, and vapor phase deposition.[4] The term "perovskite" refers to the ABX_3 structure of these materials, where the A-site contains a monovalent cation, B-site contains a divalent cation, and the X-site contains an anion. In photovoltaics, the perovskite A-site commonly contains organic cations such as methylammonium (MA^+) and formamidinium (FA^+), inorganic cations such as Cs^+ or Rb^+, or a mixture. The B-site is almost exclusively occupied by Pb^{2+}, though some work has explored lead-free alternatives using Sn^{2+}. However, tin-based PSC have yet to reach efficiencies and lifetimes comparable to those of the standard lead-based devices.[5] Halides – typically I^-, Br^-, or Cl^-, or some mixture of the three – occupy the X-site. Compositional tuning of the A- and X-sites enables tailoring of the band gap, an attractive property for optoelectronic applications. For example, substitution of I^- anions with smaller Br^- anions causes contraction of the atomic lattice and a more favorable orbital overlap with the B-site cation, increasing the band gap energy.[6] This band gap tunability makes perovskites suitable both for single-junction solar cells and for "tandem" devices which contain multiple absorber layers.

Recent advances in PSC have yielded power conversion efficiencies (PCE) exceeding 25% for single-junction devices and 29% for tandem perovskite-Si cells.[7, 8] The pace of the PCE increase is unprecedented in the field of photovoltaics, and the research interest in PSC has increased exponentially to match this historic trend.[4] The types of perovskite

absorber have also diversified, from the baseline methylammonium lead triiodide (MAPI) system to more exotic alternatives such as lead-free, mixed-cation/anion, and all-inorganic perovskites.[4]

As PSC approach commercialization, several experimental challenges slow their advancement, including the vast compositional parameter space available and the limited stability of perovskite materials under standard operating conditions (Figure 1.1). Various environmental stressors (light, humidity, temperature, bias, and oxygen)[9, 10, 11, 12, 13, 14] have been observed to initiate degradation in perovskite devices, impacting their optical and electronic performance and restricting photovoltaic (PV) device lifetimes to 3,000 hours.[15] For meaningful commercial deployment, these lifetimes must increase to >25 years for both all-perovskite and perovskite-Si tandem devices.[16, 17] Perovskite degradation occurs through different processes, including decomposition, degassing, phase transitions, and phase segregation, depending on the chemical composition and the set of environmental stressors applied.[7] Many compositions begin to degrade even in ambient conditions, including benchmark composition $MAPbI_3$. Related mixed-halide compositions ($MAPb(Br_xI_1 - x)_3$) suffer from ion migration.

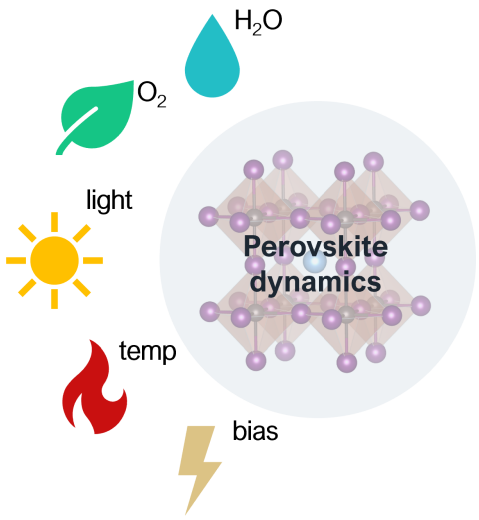

Figure 1.1: **Key environmental stressors promoting degradation pathways in perovskites**.

Several recent works identify the A-site cation as instrumental in suppressing halide segregation and increasing perovskite structural and phase stability. Alloying the A-site with inorganic cations such as Cs^+ increases the thermal stability and PV device lifetime.[18] However, pure $CsPbI_3$ has been shown to undergo phase changes in air, transitioning from the desired black cubic/tetragonal perovskite phase (α) to the photoinactive yellow hexagonal phase (δ). Utilizing mixed A-site compositions containing both Cs^+ and FA^+ is an effective approach to stabilize the α phase in ambient conditions, which is not possible for either of the pure compositions ($CsPbI_3$ and $FAPbI_3$), while simultaneously mitigating halide segregation. The smaller ionic radius of Cs^+ also promotes structural stability in the mixed perovskite by reducing lattice strain.[19] These observations are consistent with the prevailing trend in perovskite photovoltaics where mixed-site compositions yield the highest efficiencies and device lifetimes.[8] Further exploration of mixed Cs-FA and Br-I compositional spaces is

necessary to understand and improve their demonstrated structural and thermal stability.

1.3 Charge carrier recombination physics

Photovoltaic devices require generation of mobile charge carriers in order to function, which arise in the form of electron-hole pairs. Absorption of light energizes an electron in the valence band and causes it to move to the conduction band, leaving behind a hole (Figure 1.2a). Electrons in the conduction band often return to valence band energy states causing charge carriers to annihilate one another. This process, termed recombination, may either be radiative or nonradiative. Radiative recombination is unavoidable even in an ideal solar cell. Figure 1.2b shows this process schematically, in which an electron travels directly from the conduction band to the valence band and emits a photon produced with energy equal to the semiconductor bandgap (E_g). Nonradiative recombination in nonideal solar cells typically arises due to defects that add electronic states within the bandgap, known as traps. This trap-assisted recombination (also called Shockley-Read-Hall recombination) produces radiation in the form of heat and adversely impacts the electronic performance (Figure 1.2c). A second form of nonradiative recombination, Auger recombination, is also common in solar cells. In the Auger process, an electron travels directly from band-to-band, but the energy is transferred to another charge carrier within a band and no photon is produced (Figure 1.2d).[20, 21]

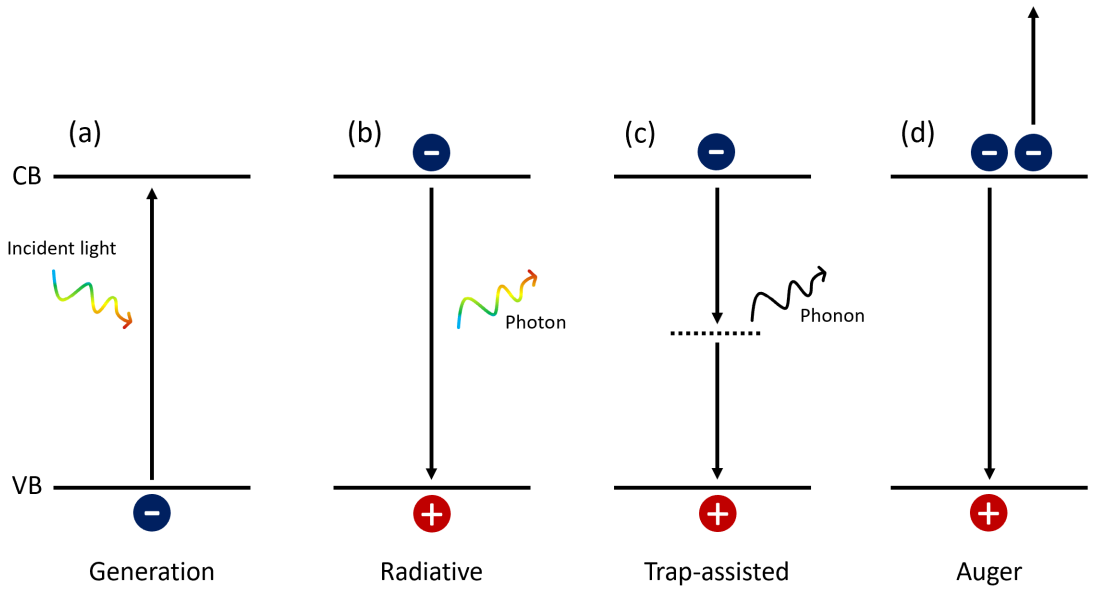

Figure 1.2: **Charge carrier generation and recombination in semiconductors.** (a) The standard generation process of photon excitation and creation of an electron-hole pair. Upon generation, charge carriers may recombine through several pathways. (b) Radiative recombination: an electron makes a direct band-to-band transition and emits a photon at the bandgap energy. (c) Trap-assisted nonradiative recombination: an electron travels to a mid-gap defect state and emits a phonon (heat) or a low-energy photon. (d) Auger nonradiative recombination: an electron makes a band-to-band transition but transfers energy to another charge carrier rather than emitting a photon.

1.4 The promise of machine learning and experimental automation

The current PSC design process involves careful compositional tuning,[22] systematic fabrication and/or characterization for each active layer,[23, 24] and time-consuming stability and aging tests.[25, 26] The high-dimensional perovskite parameter space and lengthy testing times motivate the use of machine learning (ML) to resolve the integral effects of environmental factors on the stability and performance of PSC without traversing every single stressor combination for all possible compositions.[27] ML comprises a growing set of

versatile techniques with a wide range of applications, including traffic speed prediction,[28] medical image screening,[29] and wind speed forecasting.[30] Thoughtful implementations of ML algorithms for materials science have already shown potential to alter research paradigms and drastically quicken the material design process. In energy generation, ML has been leveraged for Si PV to predict future system performance metrics or environmental conditions in real-time.[31, 32] Furthermore, ML has applications in related fields such as energy storage, where various research groups have implemented models to forecast the remaining useful lifetime in batteries and fuel cells.[33, 34, 35, 36] Likewise, the PSC community will benefit from novel research approaches involving ML, which greatly mitigate current experimental impediments.

Automated and autonomous experimentation are additional toolkits with the potential to accelerate perovskite research efforts. Automated experiments are defined as any which operate without human intervention. Automation can range from simple code to acquire data at fixed intervals to entire robotic systems to fabricate and characterize samples. These examples are distinct from autonomous experiments, which employ artificial intelligence (AI) to analyze data and determine subsequent experiments based on the previous results.[37] Coupling robotics and AI opens the door to closed-loop autonomous laboratories, which can advance materials discovery without any human input beyond initial setup and programming.[38, 39] ML, automated experiments, and fully autonomous laboratories all have important niches in PSC development, complementing more traditional materials science research techniques.[27] My Thesis utilizes these tools in concert with environmental PL to advance knowledge of temperature- and humidity-induced degradation in perovskite materials. I develop a novel, high-throughput experimental system for PL along with data

analysis and ML pipelines which generate forecasts of perovskite optical behavior under various operating conditions.

Chapter 2: Research Objectives

In this thesis I accomplished the following research objectives by building a high-throughput system for *in situ*, environmental photoluminescence (PL) spectroscopy which I then used to acquire >25,000 PL spectra from halide perovskite thin films, analyze the impact of temperature and relative humidity on radiative charge carrier recombination, and finally train machine learning (ML) models to forecast PL emission.

(i) Develop a machine learning roadmap for perovskite solar cell development. I conceptualized and illustrated a five-step framework for perovskite ML projects that I demonstrated through three proof-of-concept examples trained with literature data. The baseline projects are as follows: forecasting humidity-dependent PL in perovskite films (achieved with 14% error), predicting temperature-dependent device power fluctuations (6% error) and determining conductivity of a PV device layer via machine vision (19% error). A data-driven approach for perovskite development is proposed, which includes autonomous experimentation, ML, and feedback loops connecting compositional screening with long-term optoelectronic device performance.

(ii) Design and fabricate an automated PL characterization system for photovoltaic materials. I designed and fabricated a custom setup for *in situ*, environmental PL. Unlike most conventional PL systems, the setup acquires data from up to 14 samples

during a single experiment. This reduces the amount of time required 14-fold and ensures that all samples are exposed to completely identical environmental conditions. I also developed a Python code to completely automate experiments lasting up to seven days. Real-time monitoring and automated data processing further streamline the process.

(iii) Probe temperature- and humidity-induced photoluminescence dynamics in Cs/FA-containing metal halide perovskites. Using the automated environmental PL system, I investigated how light emission varies in $Cs_yFA_{1-y}Pb(Br_xI_{1-x})_3$ perovskites as a function of composition and environment. Temperature stress mimicking day-night cycles shows a strong linear correlation with PL in all compositions. We found that FA- and I-rich perovskites with 10-30% Cs content have high thermal stability, rapid recovery after heat-stressing, and negligible long-term degradation. Relative humidity cycling instigates moisture-induced PL enhancement as water passivates band gap trap states and promotes radiative recombination, with FA-rich compositions exhibiting the greatest effect. Analysis of spectral evolution over many cycles reveals red shifting and peak broadening in many samples as water accumulates and triggers halide segregation. Our measurements elucidate short- and long-term trends in PL as perovskites undergo repeated environmental stressing, providing insight into their stability under real-world operating conditions.

(iv) Generate quantitative time-series forecasts of environmental PL trends using machine learning. Applying the perovskite ML roadmap proposed previously, I used the PL datasets to develop models that predict photo-emission using only temperature and relative humidity as inputs. We explored linear regression, echo state neural networks, and auto-regressive integrated moving average algorithms and identify the last as the most promising approach. We achieved high accuracy for both the temperature cycling (7.3%

error) and humidity cycling (10.3% error) tasks over prediction windows covering 70+ and 50+ hours, respectively. This work validates our ML methodology and presents a broad framework that can be extended to other perovskite compositions and environmental stressors.

Chapter 3: Machine Learning Roadmap for Perovskite Solar Cell Development

In this chapter, we describe the utility of ML as a toolkit to accelerate PSC research and development to an unprecedented pace. We begin with an overview of relevant ML concepts, then detail our framework for applying learning algorithms to perovskites. We dedicate a large portion of the discussion to three important stages in the PSC design pipeline: compositional screening, perovskite layer synthesis and analysis, and full device fabrication and testing. In each of these sections, we delineate the key questions to answer and provide literature examples that apply ML to these questions. Next, we discuss ML for spatially-resolved characterization and imaging projects. We also present three original proof-of-concept examples, which apply baseline models to data from the scientific community. These demonstrative examples include time-series forecasting, predicting trends in device degradation, and extracting information from images, with all associated data and code publicly available at https://github.com/mgsrivastava/ML-perovskites for easy reference. Finally, we conclude with our vision for an integrated ML pipeline that spans multiple stages of PSC design and highlight the most promising avenues for future work in ML for perovskites. This chapter is adapted from M. Srivastava et al., *J. Phys. Chem. Lett.*, **12**, 7866-7877 (2021).

3.1 Overview of ML Concepts

We begin with a description of key ML-related concepts mentioned in this chapter. ML algorithms for materials science research are often grouped into two broad categories: supervised and unsupervised learning. Supervised learning processes involve input data that is labeled with a known "correct answer," and include regression and classification.[40] In regression, the model predicts a continuous valued output based on one or multiple inputs. Regression is useful for numerical predictions and time-series analysis, for example to forecast PSC efficiency over time. Specific algorithms of interest are linear regression, ridge regression (RR), decision trees, random forests (RF), and neural networks. Classification also involves labeled input data, but the model output is non-continuous and instead sorts the input data points into known categories.[41] These algorithms (which include naïve Bayes classifiers, k-nearest neighbors, and support vector machines) are helpful for grouping data into classes, for example to analyze occurrences of different types of known defects in perovskite films. Note that many algorithms can perform both regression and classification. Unsupervised learning uses data that is not previously labeled and includes clustering techniques such as k-means.[42] Like classification, clustering sorts input data into groupings. This can elucidate hidden trends in the data, for example to discover which types of defects commonly exist in perovskite devices, where the defect classes are unknown.

Deep learning and neural networks are powerful techniques to make complex, accurate predictions and are excellent candidates for perovskite PV applications. However, these models lack the interpretability of simpler algorithms such as linear regression or decision trees. Artificial neural networks (ANN), which are often referred to simply as "neural net-

works (NN)," functionally mimic neurons in the brain.[43] Layers of neurons (or "nodes") perform calculations on input data then transfer the computed values to other layers. One common type of neural network is the convolutional neural network (CNN), which is often used for image analysis tasks such as object recognition or image classification.[44] CNN models work best with large data sets comprising of at least hundreds of images. Another class of NN is recurrent neural networks (RNN), which are unique in that they can retain a "memory" of previous events in the data. Thus, RNN are particularly well-suited for time-series prediction tasks. Echo state networks (ESN), one type of RNN, is often used to model nonlinear systems.[45] ESN is notable because of its sparsely connected hidden-layer nodes, an architecture which increases the model's computational efficiency. Another useful type of RNN is long short-term memory (LSTM), which can process data sequentially and learn long-term trends.[46]

Implementation of an ML model requires thoughtful data acquisition, pre-processing, visualization, and feature engineering. Normalization is common, especially if there are many input features with differing ranges of values. Obtaining enough data to train a model is vital, as we illustrate in later sections. Baseline models should be trained on the information available, then evaluated to determine if the data is sufficient or if more must be acquired. In cases where training data is lacking, augmentation can create a larger training set.[47] This may involve interpolation using linear combinations, adding noise, or image rotation and mirroring.[48, 49] Recent work has also developed physics-informed data augmentation strategies. For example, Oviedo et al. took advantage of physics domain knowledge to augment an XRD data set through peak scaling, peak elimination, and pattern shifting.[48] Such physics-driven augmentation is a rational, robust method to expand the sparse data

sets that are common in materials research problems.

Finally, to optimize an ML model, hyperparameters (parameters which control the learning process and must be set prior to training) are tuned to yield the best predictive performance on a validation data set. This process is often automated using iterative or grid-search approaches, which train many models with slightly different hyperparameters to pinpoint the optimal values. After the model is finalized and hyperparameters are set, it should be evaluated using additional data. Note that the data for this step (test set) is distinct from both the data used to tune the model hyperparameters (validation set) and the data used to train the model (train set). The question of what a "low" or "good" test error is depends on the specific ML project. Researchers should consider how the model compares to a human expert in terms of speed and accuracy. Some tasks, such as identifying subtle trends in images, may not be feasible for humans. In these cases, a higher model error may be acceptable.

If the test error is unreasonably high, several options exist to remedy the issue, including obtaining more training data, using a different model (or comparing several models and selecting the highest-performing), using different input features, and checking for overfitting. Overfitting is a common issue in ML, where the model fits the training data too closely and is unable to generalize. This issue is evident when the test error is significantly higher than the training error. To prevent overfitting, simplify the model to increase generalizability. Common approaches include removing data features, using more training data, and adding regularization terms (which impose penalties to discourage overfitting) during model training. Ensemble learning techniques such as bagging, which combines predictions from several models to "smooth out" the result, are also commonly used to mitigate overfitting.[50] Out-

side of the brief overview presented here, we direct readers to several recent papers for more detailed information on ML best practices focusing on materials science.[51, 52, 53]

3.2 Roadmap

The overarching goal of applying ML to PSC research is to elucidate novel physical insights and drastically reduce the time to develop, characterize, and optimize devices. With this in mind, we show how ML aids PSC design at three distinct stages: compositional screening (Figure 3.1a), material fabrication and stability analysis (Figure 3.1b), and full device development and testing (Figure 3.1c), as described in the following sections. At the compositional level, elemental site occupancies are selected based on chemical and lattice information. This elemental tuning is a time-consuming process, which ML expedites. For example, Saidi and colleagues used a hierarchical CNN to predict the lattice constant and octahedral tilt angle for ABX_3 perovskites, then used these features as the input for a second CNN to predict the material band gap.[54] Model input features were elemental and structural descriptors such as ionization energies, electron affinities, and tolerance factor. Using this network architecture, the authors predict band gap values varying from 0.2 to 6.0 eV, relevant for the design of optoelectronic devices such as tandem photovoltaics and LEDs. The CNN performed remarkably well, providing bandgaps with a root-mean-square error (RMSE) of only 0.02 eV (Figure 3.1d) compared to Density Functional Theory (DFT) results.

With suitable elemental compositions established, PSC development reaches the materials level (Figure 3.1b). At this stage, perovskite fabrication parameters are set with critical

absorber layer properties (such as light absorption and carrier mobility) in mind. Given perovskites' facile degradation, this focus also includes crucial stability testing to investigate the underlying physical mechanisms. ML models can use past data to predict future perovskite performance under various environmental stressors, including temperature, bias, humidity, light, and oxygen.[55] For instance, Howard et al. implemented an echo state network (ESN) to generate time-series predictions of humidity-dependent photoluminescence (PL) intensity of MAPI thin films (Figure 3.1e), and demonstrate a 12-hour prediction window with $<11\%$ normalized root-mean square error (NRMSE).[49] Extensions of this work to other combinations of environmental stressors can leverage ML to identify the leading factors associated with degradation under a given set of conditions.

At the full device level, investigations expand to include the remaining device layers, such as the electron- (ETL) and hole-transport layers (HTL). MacLeod et al. recently demonstrated a self-driving laboratory to select fabrication parameters for spiro-OMeTAD, a common HTL used in PSC devices (Figure 3.1f).[56] At this stage, characterizing stability under environmental stressors and standard operating conditions is again vital, and often yields different results than for the perovskite layer alone due to interfacial effects such as charge carrier recombination and contact resistance.[57]

Table 3.1 summarizes the key descriptors and common figures of merit for each development level. ML models at a given level may use characteristic descriptors to predict figures of merit, although they can also generate one descriptor using another or supply completely different information – for instance to classify failure modes in full devices. At each level, we highlight fruitful ML approaches and suggestions for future work. Some strategies, such as high-throughput experimentation, improved data curation, and physics-based ML, apply

equally to all levels and should be prioritized accordingly.

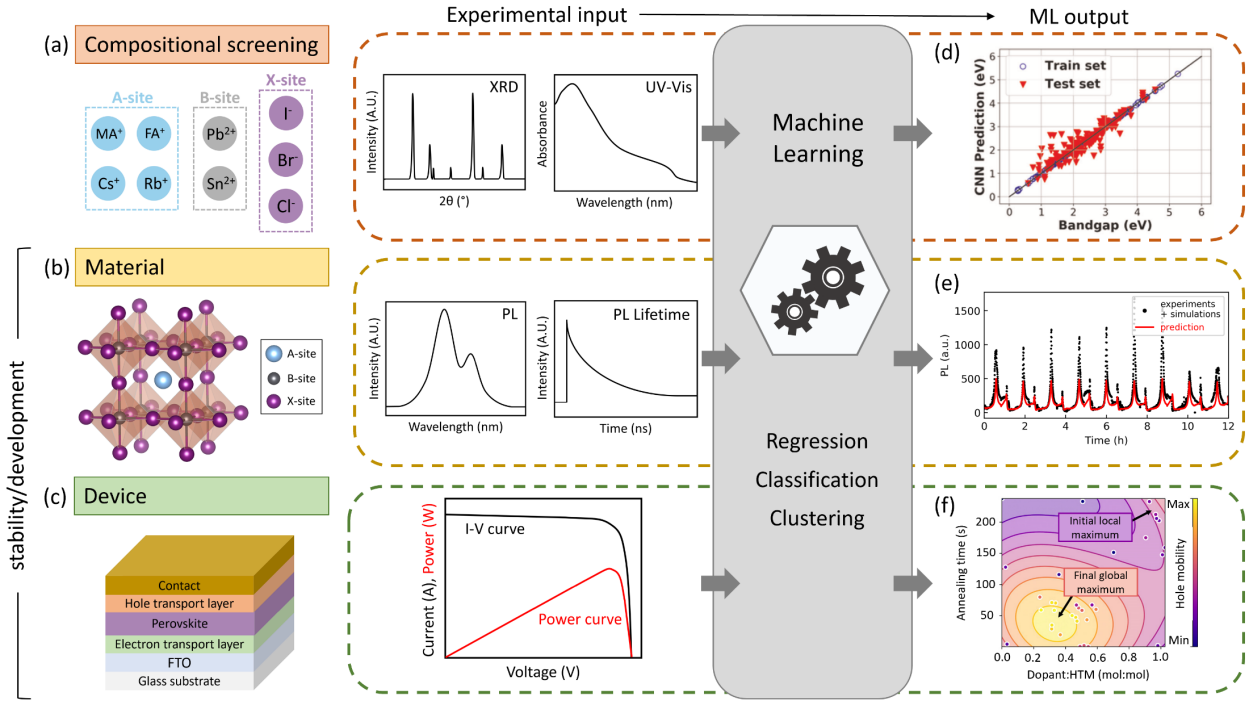

Figure 3.1: **Machine learning for perovskite solar cell development**.(a) Compositional screening, (b) material, and (c) device development/stability testing. At each stage, experimental data from techniques such as X-ray diffraction (XRD), ultraviolet-visible spectroscopy (UV-Vis), photoluminescence (PL), PL lifetime, and current-voltage (I-V) measurements is fed into ML models to obtain key physical quantities and device figures of merit or to generate predictions. Specific examples of model outputs from literature are shown in (d)-(f). (d) Band gaps for various perovskite compositions predicted using a convolutional neural network (CNN) with elemental, structural, and precursor-based data as the experimental inputs. Adapted with permission from reference [54]. Copyright 2020 The Authors, distributed under Creative Commons CC BY 4.0 license (https://creativecommons.org/licenses/by/4.0/). (e) Time-series prediction of humidity-dependent PL intensity from an echo state network (ESN) using past PL and rH data as inputs. Reprinted with permission from reference [49]. Copyright 2020 The Authors, distributed under arXiv.org non-exclusive license. (f) Map of fabrication parameters (annealing time and dopant ratio) to maximize hole mobility in spiro-OmeTAD, an organic hole transport material (HTM), from automated iterative experiments using the Phoenics global Bayesian optimization algorithm. Adapted with permission from reference [56]. Copyright 2020 The Authors, distributed under Creative Commons CC BY-NC 4.0 license (https://creativecommons.org/licenses/by-nc/4.0/).

Development level	Key descriptors	Common figures of merit	ML approaches and suggestions	
Compositional screening	Octahedral tilt angle, lattice constants, bond length and angle, ionization energies, XRD pattern, UV-Vis spectrum, dimensionality	Band gap, tolerance factor, thermodynamic quantities	Combining simulation (DFT) with ML, established pipeline to experimental validation	High-throughput data collection and analysis, physics-based ML, shared databases, standardized supplementary data files
Material fabrication and stability	Optical images and spectra, XRD pattern, PL spectrum, PL lifetime, fabrication and environmental conditions	Band gap, charge carrier mobility and lifetime	Time-series forecasting and stability predictions	
Device fabrication and stability	Optical images and spectra, J-V curves, fabrication and environmental conditions	Efficiency, stability (T80), V_{OC}, J_{SC}, charge carrier mobility and lifetime	Time-series forecasting and stability predictions, quality control, failure analysis	

Table 3.1: **Promising directions for perovskite machine learning at three design levels.** Lists key descriptors and figures of merit along with suggestions for future investigations.

Given the extensive variability of questions that ML can address, we present a generalized roadmap that applies to all three levels of PSC development. The steps of this paradigm are:

(1) identify the material question of interest;

(2) obtain sufficient data for model training;

(3) pre-process the data;

(4) apply feature engineering as needed;

(5) optimize and test the model.

ML model selection is a vital step in the framework and may occur at various points. The specifics of the selection process depend completely on the goals of the project. In the PSC field, there are opportunities for both numerical prediction models, as in time-series forecasting for PSC stability prediction, or classification algorithms, such as to classify types of defects in a failure analysis task. As stated earlier, one common approach is to train several models on the same data (step 5) and compare their predictive performance.[58, 59, 60] Another option is to choose an algorithm, or class of algorithms, immediately after determining the specific materials question of interest (step 1). At this stage, model selection requires a thorough understanding of the input data and of the desired output.

Step (2) underscores the importance of high-throughput systems, which involve drastically shortened experiment times. Conducting such research often necessitates automated data acquisition. Therefore, Figure 3.1 includes examples of suitable characterization methods for efficient collection of large amounts of data. At the compositional level, X-ray diffraction (XRD) and ultraviolet-visible spectroscopy (UV-Vis) are well-known techniques yielding key crystallographic and optical properties that then inform compositional selection.[39, 61]

At the perovskite material level, PL spectroscopy is a standard method to quickly characterize charge carrier dynamics in thin films without requiring a full device or electrical contacts.[20] Analysis of subtle patterns in spectroscopic PL or PL lifetime races is nearly impossible for the human eye, but is attainable using computer vision, enabling deeper physical insight. Device-level techniques include optical transmittance and reflectance, optical imaging, and current-voltage (I-V) measurements. These techniques are leveraged to calculate device parameters such as fill factor (FF), maximum power point, and power conversion efficiency (η).[62] The creation of shared data repositories can ease the burden of extensive data collection, supporting rapid ML model training without the need for time-intensive experimentation. In fact, large sets of crowd-sourced data have already been utilized for ML training in materials science and chemistry, for example to predict reaction outcomes.[63] Similarly, the baseline examples that we show in later sections rely on data shared by members of the perovskite scientific community, illustrating the importance of collaborative efforts. Searchable, centralized databases will streamline model training further, and likewise depend heavily on community contributions.

Steps (3) and (4) involve data pre-processing and feature engineering and are crucial in many ML pipelines. These steps often include data normalization, data augmentation, and feature selection and transformation.[48, 49] The final step of the process is (5) model optimization and testing, which includes hyperparameter tuning and evaluation on an unseen test set. We provide detailed overviews for how this paradigm applies to each stage of PSC development in this chapter, illustrated using specific examples from the literature and our own work. Additionally, we explore the question of establishing correlations between easily acquired characterization data and fundamental properties, which yields useful baseline

indicators for promising performance. ML is particularly well suited for this task because of its proven ability to quickly extract features from data that humans cannot, a capability that has a variety of practical applications (for example, to analyze medical scans).[64] In the following sections, we discuss the question of correlations in detail and provide our outlook for how ML approaches at each stage can be holistically integrated.

3.3 ML for Compositional Screening

The central goal at the composition level is to efficiently screen for material compositions suitable for PV that are thermodynamically and chemically stable. Traditional material discovery approaches of trial-and-error and incremental improvement are not sufficient given the vast parameter space of hybrid perovskite chemical compositions. Simulation-based approaches such as DFT are an option to narrow the parameter space but are slow and computationally expensive. One common approach is combining simulation data with ML, which extracts figures of merit such as intrinsic dielectric breakdown strength,[58] band gap,[65] and thermodynamic stability[59] from the data. In these studies, the ML component generates additional information from a time-consuming DFT process. Alternatively, ML algorithms can predict parameters such as lattice constants, octahedral angle, and band gaps from atomic data alone.[54, 66, 67, 68, 69] Carefully selected models also operate significantly faster and with less computational cost than DFT.

Another important facet of the compositional screening stage is high-throughput or automated experiments, which enable rapid perovskite synthesis and data acquisition.[70] Fewer studies have coupled ML models with automated experimentation, developing fully

autonomous, self-driving laboratories.[39, 71, 72] Further work centered on high-throughput structural characterization and analysis is needed to establish a coherent pipeline from broad materials down-selection to precise compositional tuning and experimental validation.

Finally, we emphasize the importance of large data repositories, which greatly expedite the compositional screening process. ML models require sufficient data to make high-quality predictions, and the amount of data needed generally increases with model complexity. In practice, the data size N needs to satisfy the condition for a good generalization: $N > O(W/\epsilon)$, where W denotes the number of free parameters in a model or neural network and ϵ signifies the fraction of permitted test error.[43] Many of the ML studies cited here used data from large online repositories, including databases from the National Institute of Standards and Technology (NIST) and the National Renewable Energy Laboratory (NREL).[38] The existence of these repositories is one reason why current ML work in the PSC scientific community is largely limited to compositional screening, as the material and device level lack a similar data-sharing infrastructure and reporting protocols to support the effort.[7] In this chapter, we therefore focus on the under-developed material and device levels, highlighting several fundamental research questions that may benefit from an ML-based approach.

3.4 Example Projects

To showcase the ML project development process, we present three example projects in the following sections using data currently available in the literature. Each project centers a different facet of PSC design: the perovskite absorber layer, the full PV device, and the hole-transport layer. Each example also uses a unique ML algorithm to demonstrate the

breadth of model types and applications possible.

3.4.1 ML for material development: echo state network to predict triple-cation PL output

The perovskite absorber material is the focus of a large proportion of investigations in the PSC field. Key research questions at this level involve finding optimal fabrication parameters while understanding and preventing material degradation. Numerous studies have probed perovskite degradation patterns and mechanisms under various environmental conditions,[9, 10, 11, 12, 13, 14] and there are many Review articles[62, 73, 74, 75] exploring this topic at both the material and full device stages. However, far fewer investigations apply high-throughput experimentation or ML models to perovskite material design, which can reduce laboratory hours and inform avenues of future study. Additionally, analysis of model features and weights can present unique physical insight.[60]

Like fabrication parameter selection, stability testing represents another major bottleneck in the PSC development process, especially as devices near commercialization and the perovskite absorber stability is thoroughly vetted. Once trained, predictive ML models overcome this holdup by drastically reducing the time required to assess degradation in perovskite materials. In recent work, Stoddard et al. used a linear regression model to forecast perovskite decay time under variable environmental conditions and achieved an average error of 12.8% while decreasing the required testing time by one order of magnitude.[76] Such single-point prediction, regression-based models have great utility and can achieve low error even with a limited data set. Larger data sets enable the use of complex models with more

powerful predictive ability, ultimately supporting long-term PSC performance forecasting that tracks variations in figures of merit over time periods of interest extending hours, days, or weeks ahead.

To demonstrate the power of a high-complexity model, we implement an Echo State Network (ESN), one class of RNN, to predict the PL intensity from a triple-cation $Cs_{0.05}FA_{0.79}MA_{0.16}Pb(I_{0.83}Br_{0.17})_3$ thin film (Figure 3.2) while applying the 5-step roadmap introduced earlier. The film was subject to cycling from 0-70% relative humidity (rH) while the absolute light emission was measured every 15 seconds. Environmental humidity is known to dynamically influence the PL response of perovskite films, as well as their underlying phase and structure.[12, 73, 77] The rH-dependent curve (black dots in Figure 3.2) shows clear cycling of the PL intensity in response to the 0-70% humidity cycles. Because this PL response represents a dynamic system containing physical information from the triple-cation film, there is strong indication that the response could be predictable, potentially using ML. Analogously, the PL response depends on both the ambient humidity at the precise moment of the measurement and on the changes that have already happened within the material – specifically, the partially reversible hydration of the perovskite film over time.[12] In other words, the material has "memory" of what has been experienced due to the history of the environment. We choose ESN for this task as this model maps an input property (rH) to an output (PL), where the output is a function of both the input property and the intrinsic historical state of the material itself.[45] This "historical state" manifests in the data through unique patterns over time, rather than a completely linear on-off PL response, and thus an algorithm with a "memory" is desirable.

When implementing complex ML algorithms such as neural networks, it is vital to

use sufficient training data. Our raw data set consists of five 4-hour runs on samples with identical compositions, where each run contains three humidity cycles and 240 data points. The PL traits observed are unique to the perovskites, following the on-off cycle of rH. Measurements under identical conditions were performed on a GaAs control solar cell and no significant changes in the PL signal were observed (not shown). We augment this data using a linear interpolation method[78, 79] to expand the data set to 60 runs (14400 points) total, which are then stitched together randomly to generate one coherent time-series. Note that such an augmentation routine assumes that the five collected runs are a fair representation of the underlying material behavior, assumes that they encompass sample-to-sample variance, and neglects effects from long-term degradation. The key assumption here is that the physical properties (e.g. PL and the state of the material) are a continuous function of parameters in the feature space (e.g. rH), thus similar parameters should yield alike output. This is a critical conjecture that applies to the use of most NN models to approximate solutions to complex problems. Researchers in materials science and beyond have adopted data augmentation methods using a similar strategy, as in the XRD peak-shifting example discussed in the "Brief Overview of ML Concepts" section.[48, 49, 80] For more information on data augmentation, we direct readers to several references which discuss this topic at length.[47, 78, 79, 81] We then supply the ESN with time-series training data tracking rH and PL from 2 hours (Figure 3.2a), 5 hours (Figure 3.2b), 10 hours (Figure 3.2c), and 20 hours (Figure 3.2d) of the expanded data set, holding out the remaining hours for testing. At 2 hours, the ESN diverges from the data, and the NRMSE is over 100%. As the model receives additional training data, the NRMSE decreases steadily, and the prediction (red line) visually shows the improved fit. By 20 hours, the ESN has

learned details about the data sequence, such as the horizontal, low-PL intensity regions between each humidity cycle, the slope of the PL increases and decreases, and the spiked responses that occur at the beginning of some rH cycles. We then optimize the 20-hr model, setting the network's noise and spectral radius through a grid search approach (Figure 3.2e). While the exact hyperparameters vary between different algorithms, this tuning step is crucial. The purposely poorly selected hyperparameters (Figure 3.2d, Prediction 1 and 2) lead to high prediction errors of 25.5% and 20.1%, respectively. By providing sufficient training data and tuning our model hyperparameters, we ultimately achieve an NRMSE of 14.3% over a 12-hour prediction window (Figure 3.2d, Prediction 3). Demonstrative code for this example, and all other example projects, is available on our github repository at https://github.com/mgsrivastava/ML-perovskites. The repository includes both the Python code necessary to replicate our analysis and a detailed outline of all computational steps written in plain English. Appendix B also contains the plain English descriptions of our code.

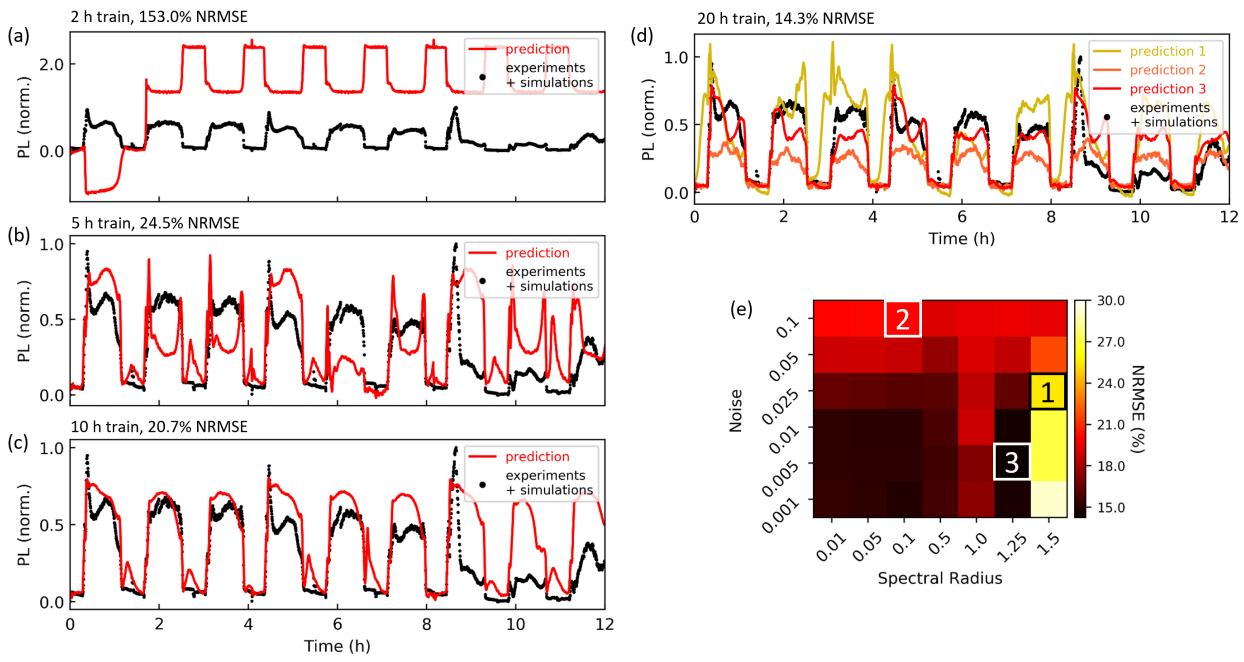

Figure 3.2: **Predicting the optical response of perovskite thin films** Echo state network (ESN) predictions of photoluminescence (PL) for a metal halide perovskite ($Cs_{0.05}FA_{0.79}MA_{0.16}Pb(I_{0.83}Br_{0.17})_3$) thin film after (a) 2 hours, (b) 5 hours, (c) 10 hours, and (d) 20 hours of training data. Augmented triple-cation data (black dots) is compared with the ESN prediction (red line). As the model receives longer lengths of training data, its predictions stabilize and the normalized root mean square error (NRMSE) decreases. Predictions 1, 2 and 3 in (d) are obtained after 20 hours of training data with various ESN hyperparameters (noise and spectral radius). (e) NRMSE for the three predictions shown in (d) as hyperparameters are optimized using a grid search approach. The minimum value found is 14.3%.

We envision further extensions of ML to several facets of the perovskite material stage, where it serves as a powerful tool for accelerated stability testing and rational fabrication of the perovskite layer. Future studies may involve integration with autonomous laboratories to streamline the workflow from compositional selection to thin film fabrication to long-term material stability testing. For the latter, the end goal is a model that generalizes to unseen combinations of environmental conditions. ML can also enhance imaging-based

investigations into degradation and defects at the material level, an exciting application which we discuss in-depth in a later section.

3.4.2 ML for device development: long short-term memory for MAPI device forecasting

Much of the work and key questions at the device level mirror those at the material level. However, the degree of complexity multiplies with each added layer. Understanding degradation under standard operating conditions and optimizing layer fabrication are essential goals. Therefore, work at the device stage typically involves engineering interfaces and architectures[82, 83, 84, 85] and investigating PSC stability (under stressors such as light,[86, 87] temperature,[88, 89] bias,[75] oxygen,[90] and humidity[91]). As with the material level, ML can quickly determine effective processing conditions for various layers.[56] Furthermore, by employing large shared data repositories that include fabrication methodology and *in situ* chemical information, ML techniques at the material and device levels can incorporate additional training features and potentially yield more accurate metrics to indicate degradation far in advance. Clarifying which fundamental properties and environmental conditions exert the most influence over long-term performance will, in turn, lead to more targeted compositional engineering.

As an example, we use data from reference[89] to predict temperature-dependent power output for MAPI cells at unseen temperatures, effectively using ML forecasting to interpolate to untested environmental conditions. The raw experimental data consists of five 500-hr runs at -10, 20, 50, 65, and 95°C, which track variations in the device power. Each run

contains one data point per hour, for a total of 2,500 points. We set aside one run (at 50°C) to serve as our test set, leaving only 2,000 points for training. To enlarge this sparse data set, we apply a linear interpolation technique to generate runs for temperatures between -10 and 95°C, with a 5°C step size. The resulting data set consists of 22 temperatures and 11,000 individual data points. Figure 3.3a shows a contour plot of the augmented data set, with the ground truth experimental data marked with black lines. We again use augmentation as a proof-of-concept in the ML workflow and assume that the experimental runs encompass property (power) data over the parameter (temperature) space, such that we can linearly interpolate to obtain sufficient training data and improve prediction accuracy.[81] In practice, we need experimental data with more finely resolved temperature steps to ensure that the data captures the full range of device behavior before augmentation. We then train a long short-term memory (LSTM) model – another class of RNN – on the expanded data set and attempt to predict cell behavior at the unseen temperature. LSTM processes data sequentially to learn trends and, like the ESN, retains a history of the data over time. Practically, the models differ in that the LSTM is more effective in learning long-term trends but is also more computationally expensive. The model architecture consists of an LSTM with five output units, a leaky rectified linear unit (ReLU) as the activation function, a dropout layer to reduce overfitting, and a dense layer to output the prediction.[46]

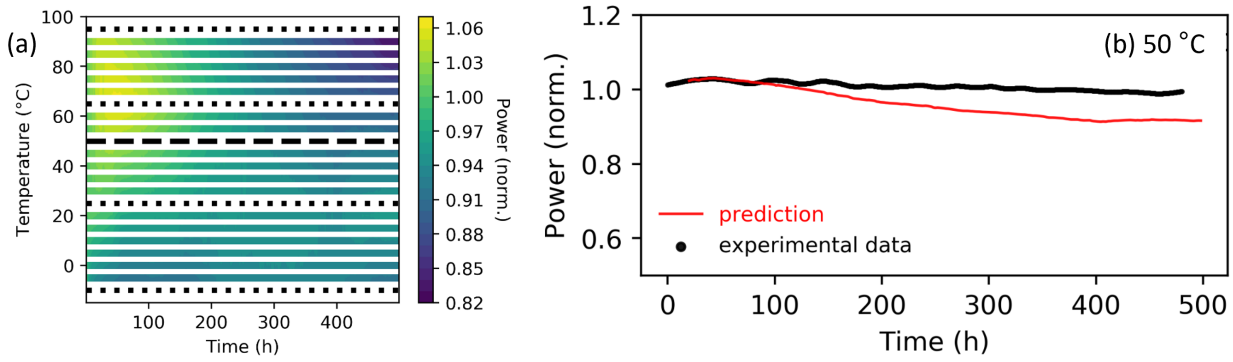

Figure 3.3: **Predicting power output for MAPI devices at unseen temperatures.** (a) Augmented data set of 500-hour runs at temperatures ranging from -10 to 95°C, tracking power output over time for $MAPbI_3$ PV device. Black lines indicate ground truth experimental data (from reference [89]) and colored lines indicate augmented data. Four experimental data sets (black, dotted) were used to generate the augmented training data while the final set (black, dashed) was used for testing. (b) LSTM prediction (red) for the experimental data run at 50°C (black). The data is normalized by its first point.

Using LSTM, we predict the full 500-hr power trace for the MAPI device at 50°C with an NRMSE of only 5.5%. We show the visual fit of our model in Figure 3.3b, which compares the LSTM prediction (red line) to ground truth experimental data (black dots). Because the model uses the 20 previous hours to generate a prediction, the red line begins at time = 20 hours. The LSTM learns the general trend of decreasing power and forecasts the temperature-dependent behavior at 50°C almost perfectly for the first 70+ predicted hours. Even as the prediction diverges over the course of 100s of hours, the overall NRMSE remains under 6%. Our example here illustrates the potential that lies ahead in using ML for time-series forecasting of device performance. We envision extensions to additional test conditions (and combinations of conditions) to attain a systematic understanding of how environmental stressors impact PSC over even longer time periods (years to decades).

3.4.3 Visualizing correlations through imaging: convolutional neural network to predict hole transport layer conductance

Finally, we discuss ML for spatially resolved characterization and imaging of perovskites, which is highly relevant to both the material and device stages of development. At the nanoscale, spatially resolved information is commonly used for defect analysis and investigations of structure-property relationships. Here, ML can illustrate powerful connections between global device performance and morphological or structural information such as surface roughness, grain inhomogeneities, and crystallinity. At the micro- and macroscopic levels, imaging methods have been extensively applied in inorganic PV to quickly diagnose where device drawbacks occur (e.g. cracks on encapsulation, loss of electrical contact). Characterization methods exist for several key device figures of merit, including carrier lifetime, band gap, external voltage, reflectance, and resistance.[92] These methods involve both scanning-based mapping and full-area capture techniques. Such approaches yield large, information-rich data sets, which are difficult for humans to parse but are efficiently analyzed using ML and multivariate statistics. There are then tremendous opportunities for combining ML methodology with 2D imaging/characterization techniques, which have garnered increasing attention lately in perovskite-related research.[93] Pairing ML with optical microscopy studies is another potentially valuable approach, as machine vision analyzes images faster than humans and quickly resolves trends. Recent work has used image-recognition to automate the identification of perovskite single-crystal formation[94] and to classify defects in spiro-OMeTAD thin films.[95] Both of these studies use a 2D CNN as a classifier. As stated earlier, CNN perform sophisticated image analysis tasks and can establish compelling

connections between images and key figures of merit while extracting hidden trends. Compared to a fully connected deep neural network, CNN has a much smaller number of free parameters available for adjustment and is more efficient in capturing key features in an image.[43]

While CNN is commonly used for classification, it can work equally well for regression to produce a numerical prediction. Nevertheless, CNN-based regression has rarely been attempted on hybrid perovskite materials. To illustrate the power of CNN in capturing underlying trends from images that is all but intractable for humans, we construct a CNN model to predict electrical conductance using dark-field (DF) images of spin-coated and thermally annealed Spiro-OMeTAD thin films (a common HTM for PSCs). There is an essential underlying correlation between material's electrical conductivity and optical properties via the dielectric function,[96] and consequently this is a potentially learnable problem. We use data from a previous reference, where the DF images were acquired in an automated sample synthesis and characterization experiment pipeline, and the conductance was measured using the traditional four-probe approach.[56] In total, we separate 210 original DF images into training and testing sets with an 80:20% split. We further divide the training data into train and validation sets with another 80:20% split. Each image has seven corresponding conductance measurements acquired at different locations using I-V data. We average all measurements into one value per image, and then normalize the data between 0 and 1. During the training process, image data is augmented through random rotations, width and height shifting, flipping, and zooming to ensure the model is fed with representative images. Our CNN architecture consists of three 2D convolution layers (3x3x32, 3x3x64, and 3x3x64, respectively), each of which is followed by a max pooling layer (2x2). To mitigate overfit-

ting, the convolutional layers are L2 regularized. The network ends with two fully connected layers (100 and 64 in size, respectively) prior to the output layer, which predicts a single conductance value for each image. The weights are updated using ADAM optimizer at a learning rate of 0.001.

Figure 3.4a-c shows examples of DF images on Spiro-OMeTAD thin films. The lighter regions of the images indicate annealing-induced bubbling and dewetting of the films during processing while the darker regions correspond to more uniform areas. However, the degree of dewetting does not have an obvious correlation with the conductance, as the example images in Figure 3.4 demonstrate. We emphasize that our close examination of all 210 DF images confirms that they do not possess visually distinguishable patterns for samples with high, medium, or low conductance. This renders impossible even qualitative visual correlation with conductance value using human visual analysis alone. Yet, as Figure 3.4d shows, the CNN model can analyze the underlying features of the images and successfully predicts the conductance values with a reasonable uncertainty (20% NRMSE). Considering the limited amount of image data tested here, the model has notably acquired the "knowledge" or trend of the correlation between the DF images and electrical conductance to an extent that would otherwise not be possible by human visual analysis. Our example here demonstrates the remarkable potentiality of using ML-based analysis to identify correlations hidden within microscope images and the opportunity that lies ahead in PSC imaging/spatially resolved characterization.

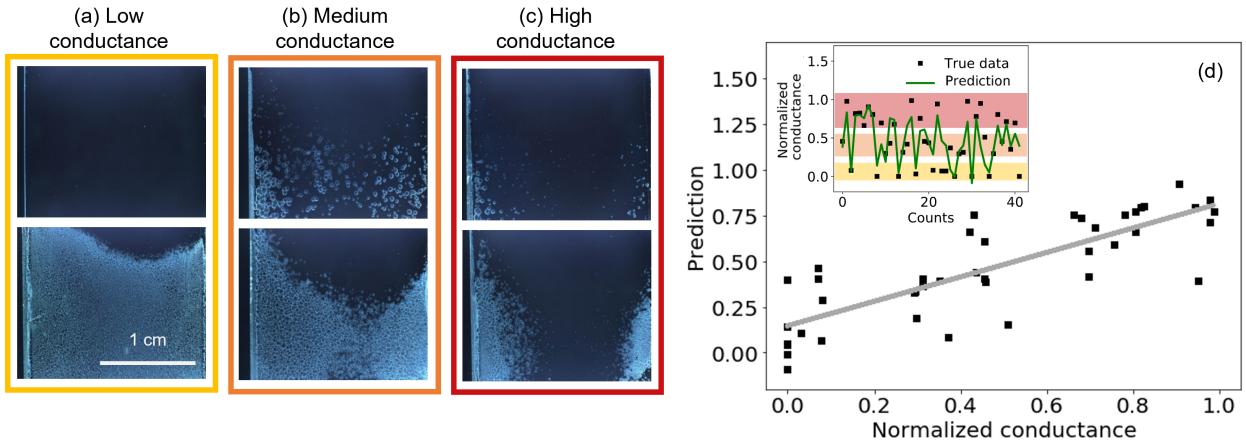

Figure 3.4: **Correlating electrical conductance with dark field images.** A CNN model is trained to predict conductance of Spiro-OMeTAD thin films based on their dark field images. Six examples of DF images are shown for samples with (a) low (b) medium and (c) high conductance values, which are normalized between 0 and 1 for simplicity without the loss of generality. No visually distinguishable patterns can be found in these images with different conductance value ranges. (d) The predicted conductance versus the true values using the trained CNN model. Inset shows how these predicted values compare with the true value for each dark field image in the test dataset. We present the conductance in a normalized form to match the CNN training and testing processes, which are both done using normalized values.

3.5 Challenges and Pitfalls

While ML serves as a powerful toolkit applicable to many problems in the PSC design process, we emphasize that it is not applicable to every problem. Researchers must carefully weigh the benefits of an ML approach and acknowledge the limitations to their results. The first item to consider is data sparsity. As mentioned in previous sections, ML models require adequate data for appropriate training, which is often a major precluding factor in materials research. In the perovskite field, we face a lack of large, well-represented, and cleaned experimental databases, which cover the full parameter space of PSC materials and devices,

including more than simple compositional information (i.e. morphological information, fabrication methods, and aging conditions). Automated experimentation and physics-driven ML are two promising pathways to address this issue. A standard supplemental data file which includes the previously mentioned parameters could also initiate the data-sharing infrastructure that is currently lacking. Researchers should also emphasize characterization techniques which yield large, quickly acquired datasets. For example, in imaging, optical microscopy methods are better suited for use in ML rather than advanced, time-consuming techniques such as electron microscopy. Additionally, models will only provide high-quality predictions if they are trained on high-quality data. Biased data collection and improper pre-processing are common pitfalls in practical ML implementation and will negatively affect the validity of the resulting model. It is equally important to train NN on negative examples – meaning material and device data showing poor performance – as well as positive, but negative examples are seldom reported in the literature. We again direct readers to recent papers discussing specific techniques and best practices for applying ML to research in materials science.[51, 52, 53] Ideally, NN and other models should be built to be robust to common data issues, such as excessive noise or biased reporting. Some algorithms and techniques have been widely adopted for these purposes, such as regularization penalty terms, drop-out layers and other structural simplification, and Hessian-based pruning approaches.[43]

The information gained from ML also often presents limitations. Models which predict promising perovskite compositions (through band gap or other key figures of merit) do not guarantee that these compositions will produce optimal devices, nor do they account for ease of material synthesis. Instead, ML at the compositional level narrows the parameter space for more focused research at the material and device levels. By a similar token, optimizing

parameters for a single device layer does not ensure optimized behavior in a complete device, and experimental verification is crucial. We also note that ML models developed using full devices will not inherently disentangle effects from each layer but may be trained to do so if features from separate layers are incorporated. Finally, advanced deep learning techniques produce models with convoluted architectures and parameters that tend to lack simple physical interpretation. This reflects the general trade-off between interpretability and prediction power seen in many ML algorithms, though analysis of global model predictions and use of a physics-driven model design may yield greater interpretability. Before applying ML, researchers must understand these and other limitations and develop a careful plan for data acquisition, management, and processing.

3.6 Conclusions

In this chapter, we outlined an ML roadmap for PSC development and demonstrated the principles using baseline models trained on currently available data. We included the steps from start-to-finish for a given perovskite ML project, including (1) identify the material question of interest, (2) obtain sufficient data for model training, (3) pre-process the data, (4) apply feature engineering as needed, and (5) optimize and test the model. We presented three examples showcasing this 5-step framework in action using MAPI and triple-cation perovskites. First, we applied ML to time-series forecasting and predict PL from thin films with an NRMSE of 14.3%. Second, we used ML to extrapolate device performance to unseen temperature conditions (NRMSE = 5.5%). Finally, we extract film conductivity from dark-field images alone (NRMSE = 19%). These example projects demonstrate the

versatility of ML and its broad applicability to the perovskite field, and we refer readers to our github repository to view all associated data and code, along with plain English descriptions of all computational steps. Future ML models will identify leading factors for perovskite degradation, integrate compositional discovery with long-term device stability, and leverage imaging datasets to understand fundamental properties. Our framework is also applicable to fields involving other renewable energy materials, such as thermoelectrics, batteries, and catalysis.

ML, coupled with high-throughput or automated experimentation, offers a new paradigm for conducting research in materials science and chemistry, with greater efficiency and more in-depth physical insight than traditional trial-and-error methods. Materials researchers in diverse fields ranging from phase mapping[97, 98] to quantum dots[99] to metallic glasses[100] to photonics[101, 102] have begun transitioning to this novel approach. In the perovskite scientific community, we propose a completely integrated ML pipeline that encompasses all three levels of PSC development (composition, material, and device) and includes screening, fabrication, characterization, and stability testing. Such a paradigm would include multiple models to establish feedback loops linking compositional discovery with long-term material and device stability. Use of extensive data repositories, standard supplemental data files, and physics-based ML strategies will facilitate tuning and testing steps for these models. There is a particular need for repositories of standardized perovskite stability testing data, which could inform sophisticated time-series forecasting models that extrapolate to unseen combinations of environmental stressors. This PSC pipeline takes advantage of our current technological capabilities in ML, data science, and autonomous experimentation and presents a rational pathway to accelerate the PSC commercialization process.

Chapter 4: High-throughput, Automated System for Environmental Photoluminescence

Traditional materials discovery and optimization relies on Edisonian, trial-and-error methods which lead to long delay times between the first laboratory demonstration of a promising technology and its commercial adoption. Perovskite solar cells (PSC) have seen a meteoric rise in efficiency and research interest, but their development is hampered by this slow, labor-intensive approach. One avenue to accelerate the process is high-throughput, automated experimental systems, which gather large amounts of data from many candidate materials in a short time. In this chapter, we design and fabricate an automated setup for environmental photoluminescence (PL) spectroscopy, a common technique for perovskite characterization requiring simple sample preparation and minimal time to acquire data ($<$2 seconds per spectrum). We construct a translation stage using two linear actuators and an Arduino, then integrate temperature and humidity control, optical components, and real-time monitoring and data analysis systems. Our *in-situ* PL system can accommodate up to 14 samples during a single experiment and collect $>$ 3000 data files over 24 hours.

4.1 Introduction to photoluminescence spectra in perovskites

Photoluminescence (PL) spectroscopy is a simple but valuable experimental technique used to study light-matter interactions in semiconductors by collecting and spectrally resolving photons emitted through radiative recombination.[20] PL can be measured through steady-state or time-resolved approaches. Steady-state PL uses a continuous laser excitation focused onto a semiconducting material and a spectrometer to collect the resulting photons (Figure 4.1).[20, 103] Time-resolved PL (TRPL) uses a pulsed laser and time-correlated photon counting to measure the decay in radiative recombination after brief exposure to the light source.[104, 105] In this thesis, we focus exclusively on steady-state PL, which we acquire over time as perovskite thin films are subjected to environmental stressors. We emphasize the distinction between this time-series PL data and the TRPL technique.

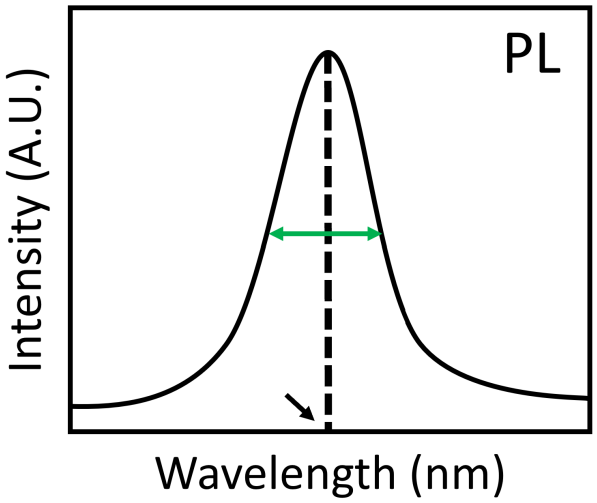

Figure 4.1: **Schematic representation of a steady-state PL spectrum**. The green arrows denote the FWHM, and the black arrow identifies the peak wavelength.

Features of a PL spectrum include the peak location, peak value, and the full width half max (FWHM). Each feature provides unique information about the structure and charge carrier dynamics within the material. In general, the PL peak should be located at or close to the semiconductor bandgap. In perovskites, E_g can be significantly modulated by adjusting ratios of ions on the A, B, and X lattice sites. Fundamentally, these changes influence the degree of frontier orbital overlap in the crystal structure. The BX_6^{-4} octahedron is critical since the B and X orbitals determine the valence band maximum (E_v) and the conduction band minimum (E_c).[103, 106] In this work, we explore modulations in Cs^+ to FA^+ ratio on the A-site and in Br^- to I^- ratio on the X-site. Although the BX_6^{-4} octahedron is what directly determines the band gap, changes to the A-site alter the lattice strain and impact the degree of overlap between the B and X orbitals.[107, 108] Density functional theory (DFT) calculations indicate further contributions from more complicated physical mechanisms, such as hydrogen bonding between the A-site cation and the octahedron, which also impact E_g.[109] As expected, X-site modifications have more dramatic effects since they directly influence E_v and E_c.[110, 111] Increasing electronegativity of the X anion correspondingly increases the PL peak energy, a trend referred to as a blue shift.[112]

The PL peak value indicates the level of radiative recombination in the perovskite. Defects in the material introduce localized trap states within the bandgap which promote nonradiative recombination and decrease the PL signal.[113] However, not all trap states are created equal. Some states are "shallow," meaning they are located close to the band edges. These states are likely to trap either electrons or holes, but not both, making them less active in SRH recombination. Conversely, "deep" trap states can trap both electrons and holes and are more active and therefore more harmful to solar cell performance. This

is one reason why Si solar cells must be manufactured from extremely high-purity, low-defect Si wafers.[114] Perovskites are known to be more defect tolerant compared to other semiconductors, another property that makes them attractive for PV.[115, 116] This is often attributed to a greater density of shallow traps, although the exact mechanisms behind this remarkable defect tolerance is still an open question.[117, 118, 119]

The FWHM is a useful check to quantify peak broadening in the spectrum. In theory, radiative recombination events should emit a photon equal to the semiconductor bandgap, but in practice we see a wider range of wavelengths in PL spectra. Peak broadening occurs for several reasons, including lattice defects, impurities, and phonon scattering, all of which shift the photon emission energy.[103, 120] Inhomogeneous chemical composition can also create bandgap variation between regions of the sample.

Environmental conditions such as light, humidity, temperature, bias, and oxygen affect PL peak location, peak value, and FWHM.[13, 88, 121, 122, 123] These changes are dynamic over time and often nonlinear. They are also heavily composition-dependent, making comparison difficult even between perovskites from the same family.[124] Traversing the large perovskite compositional parameter space and studying the effect of all stressors (and their combinations) is unfeasible on the time scale needed to commercialize and meet net zero carbon emissions goals. Machine learning (ML) can accelerate this process by learning trends between compositional ratios and responses to environmental stressors. Further, time-series predictions tracking PL over changing environmental conditions can simulate real-world operating conditions and provide an estimation of how the perovskite will perform in the future, akin to a weather forecast.

4.2 Measuring PL from multiple samples during a single experiment

To acquire sufficient data to train complex ML models such as deep neural networks, we require high-throughput sample characterization methods. Since perovskite thin film degradation occurs on a scale of days, it is extremely useful to measure multiple samples over the course of a single experiment. Typical bulk PL set-ups do not have this capability, consisting of a small, stationary sample chamber that is exposed to laser illumination either continuously or at fixed intervals while data is acquired.[20] Here, we introduce a novel characterization system enabling efficient data collection from many samples at once. The design objectives for the new system are:

(i) Acquires data from several samples during a single experiment

(ii) Exposes all samples to the same set of environmental stressors such that data can be directly compared

(iii) Allows for automated data analysis and real-time monitoring

(iv) Ensures reproducibility and consistent conditions throughout experiments lasting up to seven days

4.3 System design

The experimental setup consists of several parts that work in tandem to meet the design objectives. Environmental stressors are controlled and monitored using temperature and relative humidity setups. A custom enclosure houses multiple samples, and a translation stage allows all samples to be measured within a single experiment. These systems are

integrated into a bulk PL setup consisting of an excitation laser, various filters and collection optics, and a spectrometer to record the resulting spectra.

4.3.1 Temperature and humidity control

Temperature is regulated by a Linkam PE120 thermoelectric heating stage with structural modifications to interface with our sample chamber. Relative humidity is controlled using dry and wet N_2 lines. The wet line flow passes through a water bubbler to introduce moisture, and the rate of flow is adjusted using a mass flow controller (MFC) to ensure precise control and reproducibility. A temperature and humidity sensor with a $\pm 1.8\%$ relative humidity accuracy and a $\pm 0.2°C$ temperature accuracy is mounted in the chamber. All samples are located within 10 cm of the sensor. Sensor values are logged by an Arduino at regular intervals coinciding with acquisition of PL spectra.

4.3.2 Sample chamber

The chamber was machined from an Al alloy to reduce weight while retaining high strength. Figure 4.2 shows computer generated images of the final chamber, which measures 6 x 6 inches and can comfortably house up to 14 samples sized at approximately 0.5 x 0.5 inches. A sensor is mounted inside the enclosure to monitor the temperature and relative humidity levels. The exit wires for the sensor are sealed with epoxy to prevent oxygen or other contaminants from entering during the experiment. The lid is secured using a rubber O-ring and screws to prevent leakage. The samples are loaded and sealed inside the chamber while within a N_2-filled glovebox.

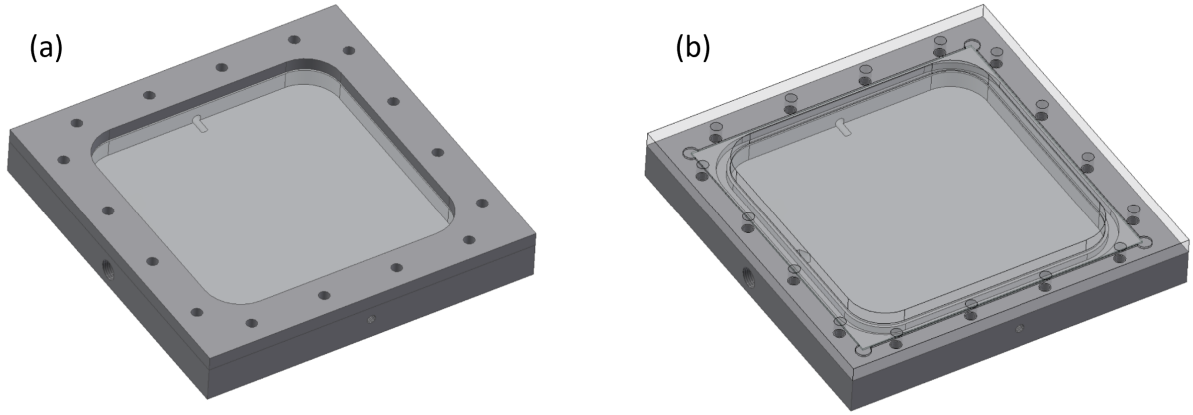

Figure 4.2: **Computer assisted design (CAD) images of the sample enclosure**. (a) View with opaque lid, (b) view with semi-transparent lid to show interior details.

4.3.3 Translation stage

The sample chamber is mounted onto a custom-built translation stage consisting of two linear actuators with NEMA 23 stepper motors. Both actuators are fitted with flat platforms to mount samples or other structures. We mount one actuator directly to the optical table, referred to as the "x-direction actuator." The second actuator, referred to as the "y-direction actuator," is mounted vertically onto the x-direction actuator platform such that rotation of the stepper motor moves the y-direction platform up and down relative to the optical table surface. Identical motor drivers control each of the stepper motors. An Arduino interfaces with both drivers, enabling synchronous motion of the stage in the x and y directions. Figure 4.3 summarizes the key components and interconnects for the experimental system.

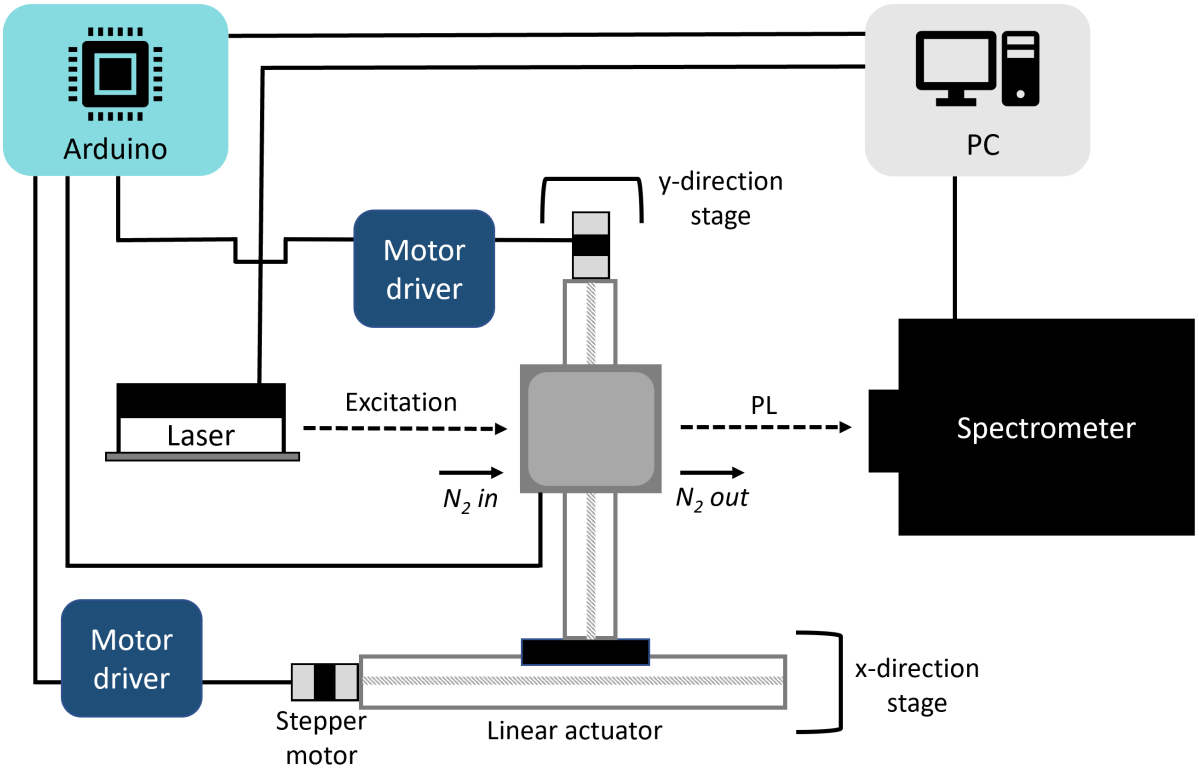

Figure 4.3: **Key experimental interconnects**. Python code on a PC coordinates the laser excitation source, spectrometer, and Arduino. Motion of the translation stage is controlled by two motor driver-stepper motor-linear actuator assemblies. The Arduino records environmental data from a sensor inside the sample chamber and operates both motor drivers. Inert N_2 gas is flowed through the chamber for the duration of the experiment.

4.3.4 Bulk PL optical path

All PL spectra are measured using a Princeton Instruments HRS-300 Spectrometer equipped with a CCD camera detector. A 532 nm power-tunable diode laser is used as the excitation source, set to achieve a power density between 50-100 mW cm^{-2} for all experiments. The excitation light is cleaned with a 532 nm center wavelength band pass filter (4 nm FWHM). The laser is directed to the sample using mirrors and remains fixed throughout

the experiment while the chamber moves via the x-y translation stage. Emitted light is partially collected using a condenser lens placed at its focal distance from the sample surface. A second lens focuses this light onto the spectrometer entrance slit. A 630 nm long pass filter is mounted inside a lens tube and attached to the spectrometer entrance to block stray reflected light from the laser. Figure 4.4 shows the complete optical path schematically. The spectrometer is operated using a grating (groove density: 300 gr/mm) which disperses the collected light to generate PL spectra. Custom python code coordinates data acquisition from the spectrometer with translation stage motion and sensor logging.

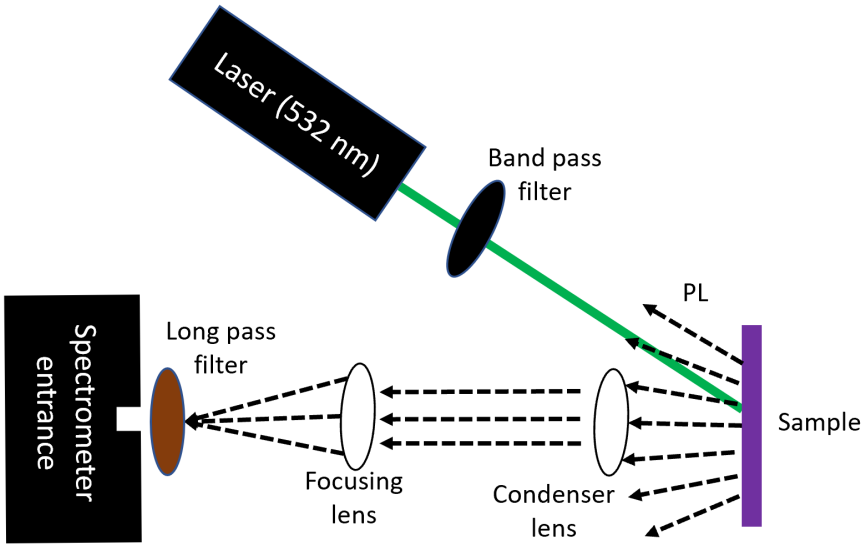

Figure 4.4: **Experimental optical path for bulk PL**. A 532 nm diode laser excites the perovskite sample, instigating PL. Condenser and focuser lenses collect the signal and direct it to the spectrometer. An initial band pass filter cleans the laser emission and a long pass filter mounted onto the spectrometer entrance blocks any reflected laser light.

Figure 4.5 contains photographs of all final system components, including a view of the environmental PL collection system in action (Figure 4.5d).

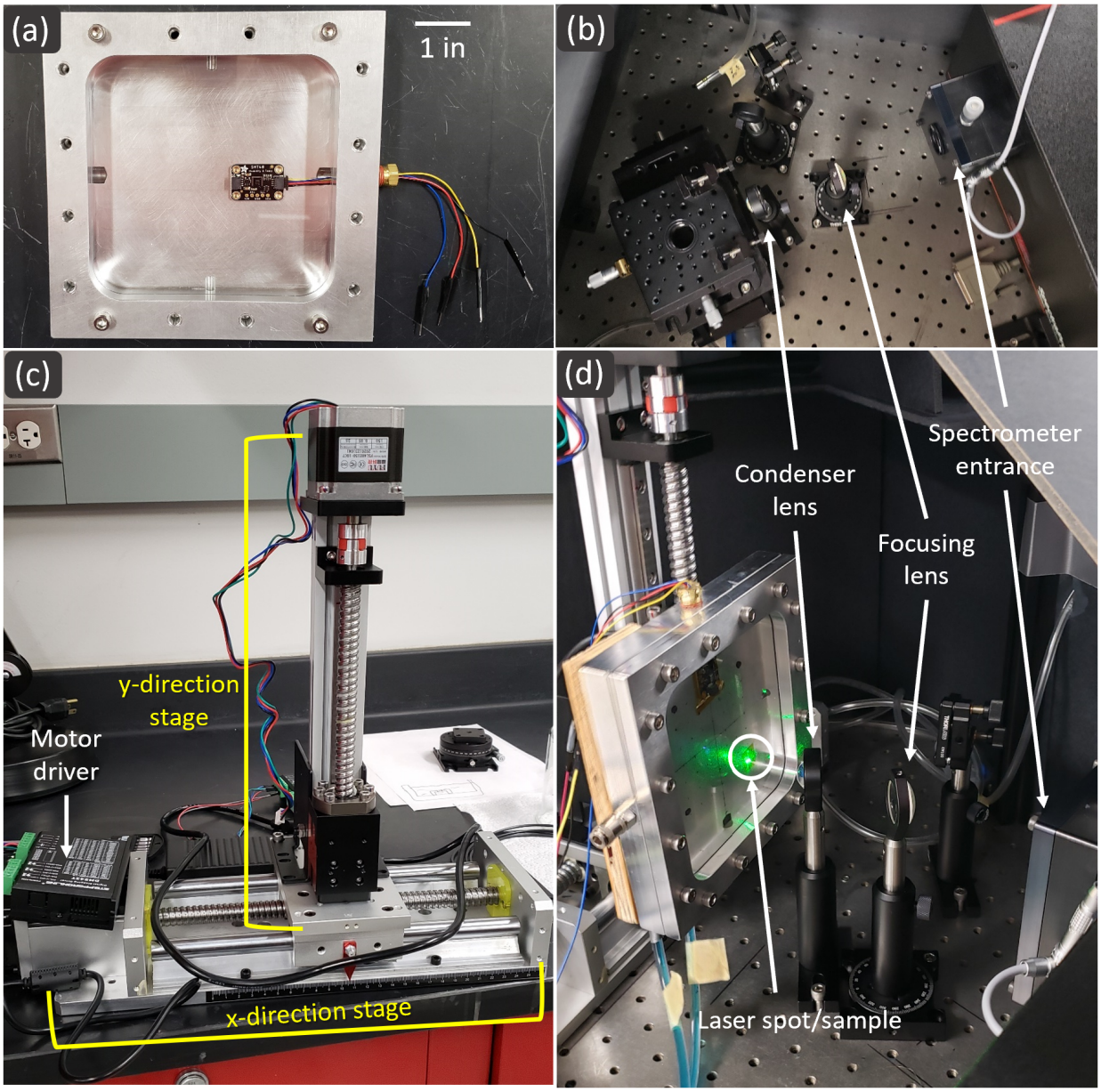

Figure 4.5: **Photographs of the final setup**. (a) Sample chamber with environmental sensor mounted. Wires exit through an epoxy-sealed plug to connect to the Arduino. Scale bar is one inch. (b) Aerial view with the two collection lenses labeled. The focusing lens directs PL onto the spectrometer entrance. A long-pass filter is mounted directly onto the spectrometer (not visible in the image) to block reflected laser light. (c) Assembled translation stage with x- and y-direction components marked in yellow. The x-direction motor driver is also shown (white arrow). (d) Close-up of the setup with the chamber mounted with one sample loaded and laser on.

4.4 Conclusions

This chapter introduces our custom experimental setup for bulk environmental PL. The system includes temperature and humidity control, optics to collect PL, and a spectrometer to resolve the emission wavelengths. One unique feature of the setup is its translation stage, which creates a mobile sample chamber and allows for measurements from multiple samples (up to 14) over the course of a single experiment. A "high-throughput" system is one that operates at a larger scale than the basic system, often integrating automation or robotics. Thus, our high-throughput environmental PL presents a scaled version of typical bulk PL which enables us to quickly obtain a suitable amount of data (>3000 files in 24 hours with the chamber loaded to capacity) to train ML models. We also introduce the PL technique, outline its fundamental physics, and describe key data features such as the peak location, peak value, and FWHM.

In the following chapters, we present results acquired from this system. Following the ML roadmap outlined previously, large amounts of training data are acquired from high-throughput optical measurements to develop ML models. This approach can be extended or applied to other perovskite studies and other optical measurements. For example, other researchers have developed robotic-driven "auto-labs" with an eye on ML integration.[38, 56, 71, 125] Continued advancements in technology will bring about even more sophisticated automation strategies and encourage a transition from the classical Edisonian model of scientific research to a streamlined, data-driven approach.

Chapter 5: Environmental PL Spectroscopy on Halide Perovskites

A thorough understanding of the effect of environmental stress on perovskite solar cells (PSC) is required prior to their commercial development. Fabrication of full devices is costly and time-consuming, while contactless measurements such as in situ photoluminescence (PL) spectroscopy require only thin films. Here, we study the environmental PL response of $Cs_yFA_{1-y}Pb(Br_xI_{1-x})_3$ perovskites, a promising compositional group for future PV applications. We probe the charge carrier recombination dynamics as the films are exposed (for 140 hours) to temperature and relative humidity (rH) cycles which mimic real-world weather conditions. Our results show decreases in radiative recombination and a blue shift in the emission spectrum of all compositions as temperature increases. We also find that FA-rich perovskites have greater structural stability, and their thermal degradation is almost completely reversible. Both Cs-rich and FA-rich compositions display an increase in PL as humidity increases, but the linearity of the response and long-term trends are highly variable. Red shifts in emission after several rH cycles indicate halide segregation, a known issue in PSC, is occurring in many samples. Combining both the temperature and rH results, we find that mixed-site occupancy tends to enhance perovskite stability, with FA-rich, I-rich compositions showing consistently high radiative recombination rates throughout the environmental stressing experiments.

5.1 Environmental PL on perovskites

Perovskite materials show great promise for next-generation photovoltaic devices. However, their long-term stability under standard operating conditions must be proven prior to commercialization and widespread use. Here, we focus on the effects of relative humidity (rH) and temperature, both of which are dependent on local weather patterns. These stressors are highly variable, with significant fluctuations during day-night cycles. Climate zones, elevation, and time of year also have profound impacts on rH and temperature. Therefore, thorough studies spanning wide ranges of environmental conditions are needed to accurately evaluate the effects of weather on perovskites of varying composition.

In this work, we probe the effects of environmental stress on mixed cation perovskites to increase understanding of the promising Cs-FA compositional space. We also explore halide-mixing using I^- and Br^- anions. The prototypical perovskite composition is methylammonium lead triiodide ($MAPbI_3$), which contains the MA^+ ($CH_3NH_3^+$) cation on the perovskite A-site, Pb^{2+} on the B-site, and the halide I^- on the X-site. However, $MAPbI_3$ is structurally unstable at elevated temperatures, and the MA^+ cation is chemically volatile.[89, 123] Consequently, $MAPbI_3$ quickly degrades to MAI and PbI_2 under thermal stressing, even in an inert atmosphere. To avoid the detrimental effects of MA^+, we instead occupy the A-site with formamidinium (FA^+) and cesium (Cs^+). Both of these cations form perovskites ($FAPbI_3$ and $CsPbI_3$) with greater thermal stability at high temperatures.[126] $CsPbI_3$ is of particular interest as a purely inorganic composition with superior resistance to temperature- and moisture-induced degradation.[127] Despite its high-temperature stability, $CsPbI_3$ undergoes a deleterious phase transition from the "black" photoactive cubic (α) phase to the "yellow"

photoinactive orthorhombic (δ) phase at room temperature.[128, 129] Further, its band gap (1.73 eV)[130] is wider than the ideal 1.4 eV for a PV cell to absorb the maximum number of photons from the solar spectrum. $FAPbI_3$ has a near-ideal band gap of 1.48 eV, but also lacks room-temperature phase stability.[107, 126]

The origin of phase stability in these materials lies within the perovskite structure itself. The ABX_3 structure consists of corner-sharing BX_6^{-4} octahedra with the A-site cation occupying cuboctahedral cavities formed by the octahedral network.[108] Changes to the A-site have direct impacts on the lattice strain and the degree of octahedral tilting. The impact of these lattice distortions on structural stability is quantified using the Goldschmidt tolerance factor (t) as in Equation 5.1 below, where r_A, r_B, and r_X are the A-, B-, and X-site ionic radii.

$$t = \frac{r_A + r_X}{\sqrt{2}(r_B + r_X)} \tag{5.1}$$

The ideal range of t for a perovskite is 0.9-1.0. Structures with tolerance factors 0.8-0.9 or 1.0-1.1 can still be stabilized, but exhibit greater octahedral tilt and lattice strain.[129] Adding Cs^+ to the A-site of $FAPbI_3$ shifts the tolerance factor into the ideal range and increases structural stability while reducing trap density.[131] Alloying also makes the α to δ phase transition unfavorable. This effect is driven by entropic gains from mixing FA^+ and Cs^+ and the high energy of formation for the δ phase containing both cations.[128]

Mixed halide perovskites are beneficial for semiconducting applications since they provide band gap tunability over a wide range and tend to produce highly efficient PV devices.[4, 127, 132] The complete compositional space investigated in this chapter is shown

in Figure 5.1. We focus on FA-rich compositions because their band gaps are more ideal for PV, as previously discussed. The 10 compositions displayed are referred to throughout this chapter using their ID number as assigned in Figure 5.1.

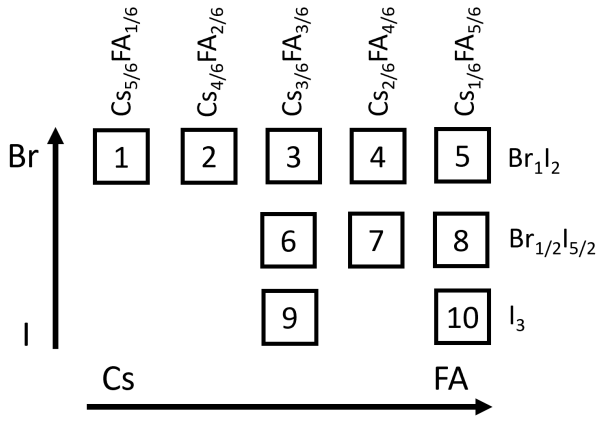

Figure 5.1: **Compositional space of the perovskite films**. Ratios of Cs:FA are varied, with a greater number of FA-rich samples since these have more promising band gaps for solar cell applications. The halide ratio is also varied, focusing on I-rich compositions. The samples are labeled 1-10 according to their compositional mix.

Here, we investigate the effects of repeated temperature and rH cycling on the optical response of $Cs_yFA_{1-y}Pb(Br_xI_{1-x})_3$ perovskite thin films by implementing environmental, in situ PL spectroscopy. The 6-hour cycles imitate day-night weather variations and are modeled based on typical summer weather in Sacramento, CA, where each cycle represents one day. For example, during a single temperature cycle the chamber environment will heat a typical summer high (30 to 50°C), cool to a typical summer low (15 to 25°C), then return to an intermediate temperature before beginning the next cycle. We quantify the thin films' real-time optical behavior using *in situ* PL spectroscopy, employing the high-throughput experimental system discussed in Chapter 4. The PL spectrum provides insight into the

radiative carrier recombination rate within the perovskites, which is directly linked to the presence of trap states and lattice defects. Additionally, the value of the integrated PL spectrum, termed absolute PL, is proportional to the V_{OC} and, thus, a strong indicator of PV device performance.

5.2 Experimental methods

5.2.1 Thin film fabrication

The samples investigated here were fabricated by our collaborators in the Correa-Baena group at Georgia Institute of Technology.[19] Due to the poor solubility of CsBr in common solvents like DMF and DMSO, 0.4 M perovskite precursor solutions are prepared for thin film fabrication. Ratios of Cs:FA and Br:I are tuned using four master solutions of 0.4 M $CsPbI_3$, $FAPbI_3$, $CsPbBr_3$, and $FAPbBr_3$. The master solutions are generated by dissolving combinations of chemical precursors under mild heat at 65°C for 1 hour. Solutions are prepared in a N_2-filled glovebox with $<$2 ppm of O_2 and H_2O. Perovskite solutions with desired $Cs_yFA_{1-y}Pb(Br_xI_{1-x})_3$ compositions are produced by mixing the master solutions in corresponding molar ratios.

The perovskite precursor solution is spin-coated onto a conductive glass, fluorine-tin-oxide (FTO) coated substrate pre-heated to 65°C using a two-step spin-coating process. The first spin-coating step is 10 seconds at 500 rpm with an acceleration of 250 rpm s^{-1}. The second step is 70 seconds at 2000 rpm with an acceleration rate of 1000 rpm s^{-1}. An antisolvent, CB (250 μL) is dripped onto the sample 5 seconds before the end of the second step. Following the spin-coating, all films are annealed for 5 minutes at 65°C.

5.2.2 Environmental PL spectroscopy

A 532 nm power-tunable diode laser is used as the excitation source for PL. The laser power is set to achieve a power density of 50-100 mW cm^{-2} for all experiments. The excitation light is cleaned with a 532 nm center wavelength band pass filter (10 nm FWHM). The laser is directed to the sample using mirrors and remains fixed throughout the experiment while the chamber moves via the x-y translation stage. Emitted light is partially collected using a condenser lens placed at its focal distance from the sample surface. A second lens focuses this light onto the spectrometer entrance slit. A 630 nm long pass filter is mounted inside a lens tube and attached to the spectrometer entrance to block stray reflected light from the laser. The spectrometer is operated using a 300 g/mm grating which disperses the collected light to generate PL spectra.

The environmental conditions of all measurements are controlled using a thermoelectric heating stage and dry and wet N_2 flow lines for tunable temperature and rH (see Chapter 4 for details). A temperature and humidity sensor is mounted in the chamber with all samples located within 10 cm of the sensor. The sensor is accurate to ±1.8% relative humidity and ±0.2°C. Sensor values are logged by an Arduino at regular intervals coinciding with acquisition of PL spectra. The sample enclosure is loaded in a sealed N_2-filled glovebox with a rH <1% to prevent exposure to air. The chamber is mounted onto a custom-built translation stage consisting of two linear actuators which enable x and y motion (Figure 4.3, 4.5). During the experiment, the stage shifts to expose each sample to the laser in turn, then holds so that spectral PL data can be acquired. The hold time is 15 seconds per sample, and data is collected from each sample every 6 minutes. All samples are simultaneously exposed

to the same environmental conditions and experience identical laser excitation for the same total amount of time.

5.3 Temperature cycling results

First, we investigate the effects of temperature on Cs-FA perovskites. To eliminate effects of other environmental stressors, N_2 gas is continually flowed through the sample chamber and the rH is kept <3%. Samples 7, 8, and 10 were subjected to regular temperature cycling from 15 to 45°C, a typical temperature range for summertime in Sacramento. Eight 6-hour temperature cycles imitate one week of summer weather. We choose these three FA-rich compositions for their ideal tolerance factors (0.9-1.0) and homogenous microstructure post-annealing.[19] PL spectra for each sample were acquired every six minutes, giving a total of 480 spectra per sample over the experiment. Figure 5.2a shows the maximum PL values for the three compositions in teal (sample 7), blue (sample 8), and gray (sample 10). The red dashed line indicates the synchronous temperature profile experienced by all samples. The trends in Figure 5.2a are as expected for perovskite materials, showing a substantial decrease in PL as the temperature increases followed by PL recovery as the temperature decreases.[103] Physically, this behavior is caused by the addition of thermal energy, which increases the probability of exciton dissociation and non-radiative recombination. The temperature dependence on PL is approximately linear throughout the duration of the experiment with no long-term degradation observed even after eight cycles. The peak shifting trends (Figure 5.2b-d) are also consistent with prior results for perovskites. All samples show a blue shift at high temperatures and a red shift at low temperatures, although the magnitude

of these shifts differs. Most semiconductors, including silicon, show the opposite behavior (red shift as temperature increases) due to changes in the Fermi distribution and weakened interatomic bonding as the lattice undergoes thermal expansion.[133] However, temperature also affects electron-lattice interactions, causing movement of the conduction and valence band edges. The exact origin of the temperature-induced PL blue shift in perovskites is still debated. Likely contributors are the reversed ordering of states in the electronic band structure[134] and unusually strong electron-phonon coupling that is sensitive to octahedral tilting.[135]

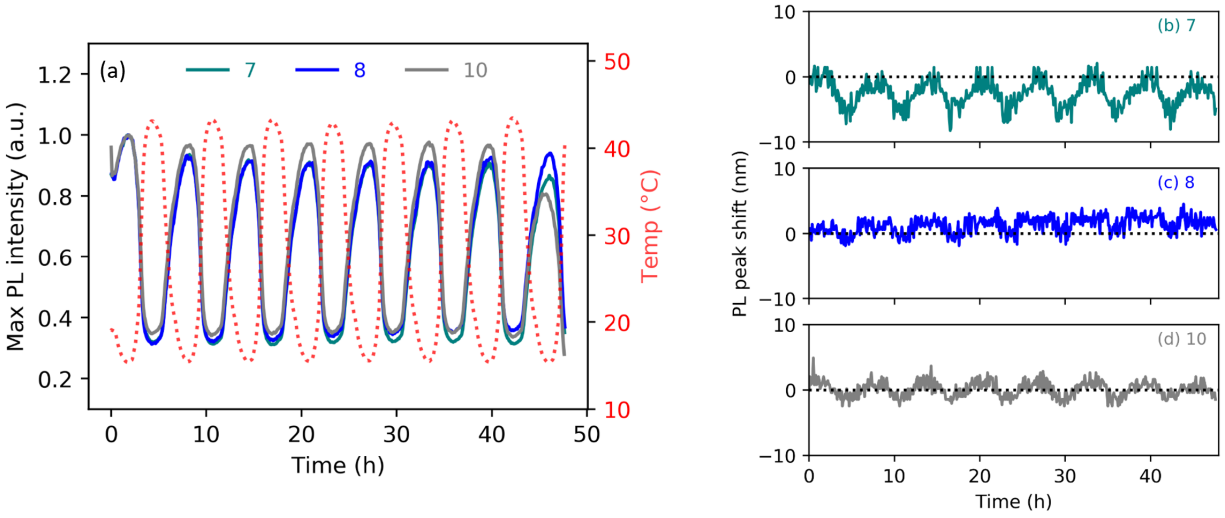

Figure 5.2: **Temperature-dependent maximum PL and peak shift of mixed-cation perovskites**. (a) Maximum PL intensity tracking for sample 7 (teal), 8 (blue), and 10 (gray) over time. The secondary y-axis denotes the temperature (red dashed line). (b)-(d) Shift in the PL peak location during the temperature cycling. The horizontal dashed line indicates the initial peak location in nm. Data was acquired simultaneously from the three samples.

To better illustrate the dramatic spectral evolution in the PL signal, we plot all collected spectra from a single temperature cycle (Figure 5.3), divided into those collected during heating, cooling, and holding at the coldest temperature. Note that during the temperature

hold there is no discernable change in the spectrum shape or peak value. This result verifies that temperature shifts are what gives rise to all observed variation in the PL time series.

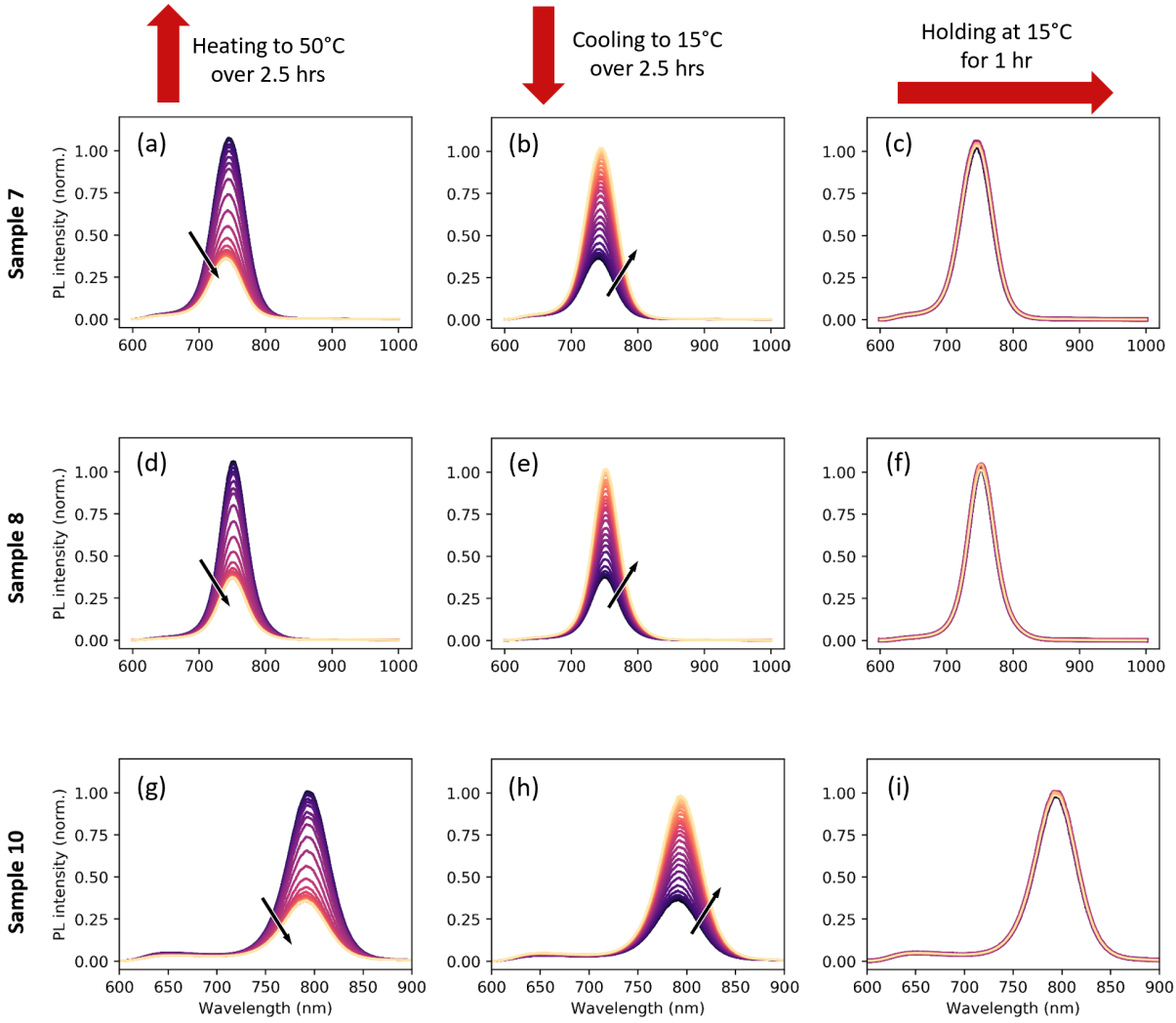

Figure 5.3: **Spectral evolution of PL emission during a single temperature cycle**. PL spectra plotted as the perovskite is heated to 50°C over 2.5 hours, cooled to 15°C over 2.5 hours, then held at 15°C for 1 hour for samples 7 (a-c), 8 (d-f), and 10 (g-i). Black arrows denote passage of time as the spectrum color changes from purple to beige. Spectra for all samples are collected every 6 minutes.

We further probe the effect of dynamic temperature changes by altering the temperature profile to reflect the irregularities in weather patterns. In the real world, it is very rare

for subsequent days to have the exact same high and low temperatures, though the range of high and low values will remain relatively consistent during a 1 or 2-week period of a season. With this constraint in mind we generate more realistic cycles, allowing the high temperatures to vary within a range of 30 to 50°C and the low temperatures within a range of 15 to 25°C. Figure 5.4 shows the final profile (black lines), which consists of 22 cycles each lasting 6 hours. We also expand the compositional space to include all samples 1-10. The evolution of maximum PL intensity for each of the 10 samples (Figure 5.5) maintains the previously observed linear dependence even with the added irregularity in temperature profile.

However, there is evidence of long-term degradation in many of the samples. Figure 5.4 tracks the PL peak for each of the samples. Again, we observe a strong correlation between the temperature (black lines) and PL intensity (colored lines). Over the course of 22 irregular temperature cycles some samples show a broader decrease in PL after repeated heat stress events. This decay is most stark for samples 1 and 3, with more subtle trends displayed by other samples such as 2, 4, and 9. Other compositions, like samples 7 and 10, show little decay.

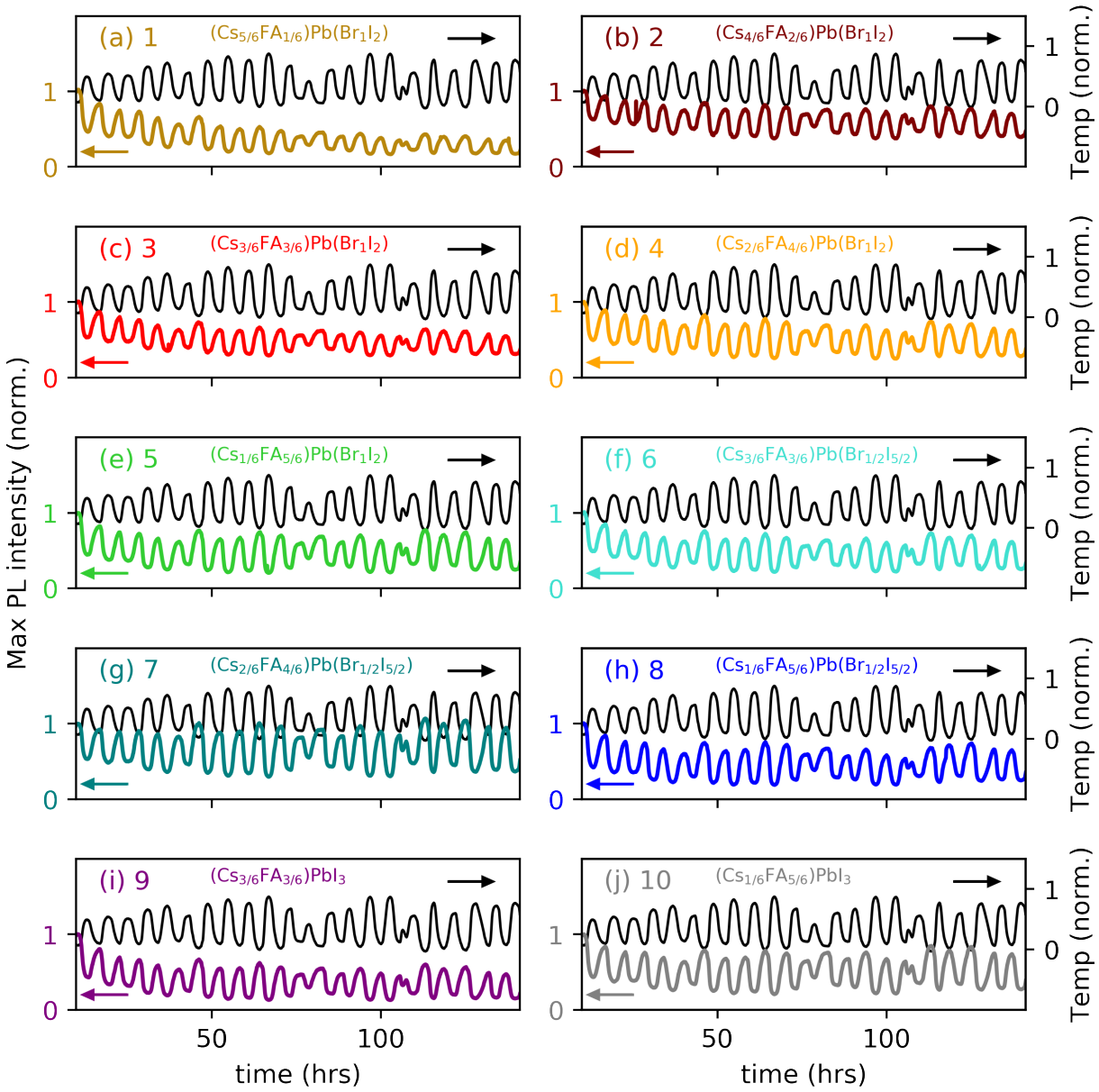

Figure 5.4: **Effect of irregular temperature cycling on PL**. Maximum PL intensity for samples 1-10, as indicated (a)-(j), subjected to irregular temperature cycling for 132 hours. The temperature profile is shown (black line) on each plot. The left y-axis denotes the normalized PL while the right y-axis is the normalized temperature (colored and black arrows are shown as a guide to the eye). Each temperature cycle is 6 hours with a high value between 30 and 50°C and a low value between 15 and 25°C.

To analyze these trends in more detail, we visualize the sample-dependent spectral

evolution in Figure 5.5a-j. Spectra are plotted from five time points during the experiment: 0 hours, 10.5 hours, 58 hours, 82 hours, and 137 hours. At each of these time points, the environmental conditions in the sample enclosure were identical (23°C, rH <3%). Therefore, although the conditions when the spectra were collected are consistent, their location within in the PL time series differs. In almost every sample, the PL shows a decay which accumulates over time. The recovery in PL from the first marked spectra (taken at 0 hours) to the final spectra (taken at 137 hours) ranges from 95% (sample 7) to only 35% (sample 1). The average recovery is 63% with a standard deviation of 15%. Lack of complete PL recovery could be indicative of irreversible changes in the material, which may be chemical or morphological in character. To verify this observation, we rested the samples in a dark, N_2-filled environment for 12 days and subsequently found significant increase in their PL response. Recovery in comparison to the PL spectra acquired at 0 hours ranges from 100% (samples 2, 7, and 9) to 61% (sample 3) with an average of 85% and standard deviation of 13%. This result indicates a strong time-dependence on perovskite optical recovery upon temperature stressing and is consistent with previous observations about rest and recovery in PSC.[55] One explanation for this behavior is that although degradation is reversible, it is driven by a kinetically limited process that requires days to complete. Therefore, over the fast time scale of the experimental temperature cycles (6 hours per cycle), the samples are unable to recover sufficiently, and a long-term trend of accumulated degradation appears. Contributions from irreversible degradation processes are also possible, particularly for samples which were not able to completely recover the PL even after 12 days rest.

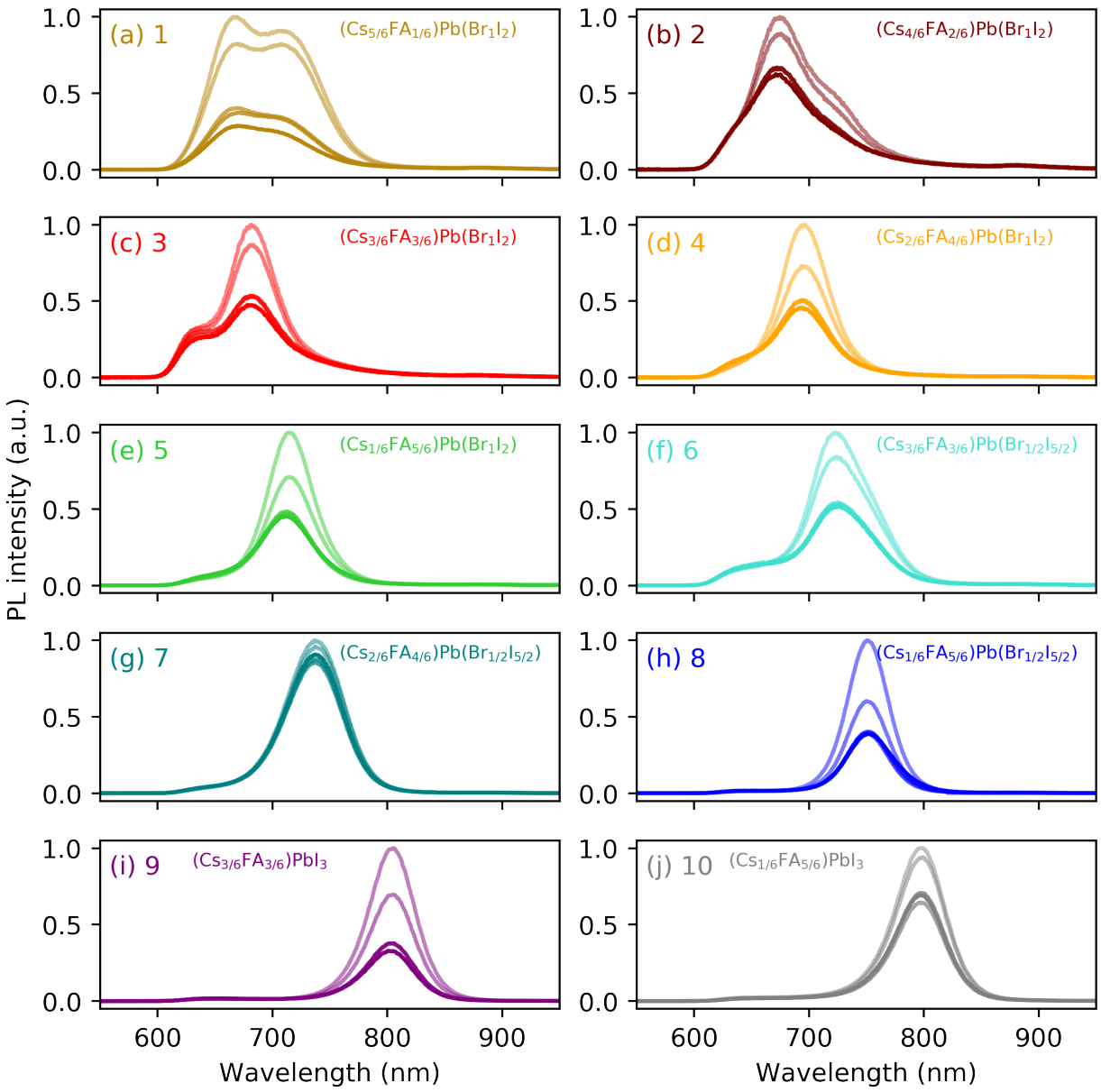

Figure 5.5: **Spectral evolution over 21 irregular temperature cycles**. PL spectra for samples 1-10 as marked in subplots (a)-(j) plotted at five time points during the 132-hour experiment. Each spectrum is taken under identical environmental conditions (23°C, rH <3%) at the following time points: 0, 10.5, 58, 82, and 137 hours. Spectra are normalized relative to the t=0 spectrum. Black arrows denote the passage of time from the lightest to darkest spectrum.

The response to temperature and subsequent recovery are also highly dependent on the

perovskite composition. Compositions with higher FA^+ content show more rapid recovery and resistance to long-term degradation. These observations are in line with fundamental understandings of phase stability in perovskites, which rely on minimizing lattice strain and maximizing enthalpy of formation for undesired photoinactive phases. This is because reduced lattice strain leads to lower defect concentrations which increases carrier lifetimes and decreases incidences of non-radiative recombination. In the FA-Cs system, adding the smaller Cs^+ cation increases the structural stability of the lattice. However, the effect is limited as too many Cs^+ ions will unfavorably shrink the lattice, imposing strain and pushing the tolerance factor below the ideal range for a cubic perovskite. Based on our results, a modest Cs^+ content of 10-30% yields the greatest thermal stability. This is consistent with previous results showing ease of fabrication and high efficiency for $Fa_{1-x}Cs_xPbI_3$ with 15-25% Cs^+.[108, 128, 136] Small amounts of Cs^+ have also been shown to produce highly oriented perovskite films, reducing non-radiative recombination by suppressing trap state formation.[137] By contrast, the two compositions with the highest Cs^+ content (samples 1 and 2) display irregular PL peak shapes and large decays over the course of the temperature cycling tests (Figure 5.5). The effects of halide content are more difficult to discern given only three Br:I ratios were studied. Of these, the Br-rich compositions (samples 1-5) show poorer PL emission and recovery compared to the high-performing samples. Previous studies have shown that a small amount of the Br^- anion stabilizes $FAPbI_3$ due to its higher electronegativity compared to I^-. This creates a stronger Coulombic interaction between the halide and the A- and B-site cations, which suppresses unwanted phase changes. Conversely, Br-rich compositions can lead to increased halide segregation, which generates defect trap states that act as centers for non-radiative recombination.[14] Sample 7, with composition

$(Cs_{2/6}FA_{4/6})Pb(Br_{1/2}I_{5/2})$ combines the positive effects of both A-site and X-site alloying, leading to a high-performing material that shows negligible long-term degradation even after 22 temperature cycles (Figure 5.4, 5.5).

5.4 Humidity cycling results

We also investigate the effects of rH on the same Cs-FA perovskite compositions. Here, we hold the temperature constant at 22°C and cycle the rH from 5-70%, again modeling based on typical Sacramento summer weather. Samples 1-10 are exposed to eighteen 6-hour rH cycles. All other experimental conditions are identical to the temperature cycling experiments. Note that while the sample compositions are consistent, we use fresh pieces of each and adjust optical fine-tuning between experiments. Therefore, any direct quantitative comparison between the temperature and rH cycling results must be done with caution. Here, we focus on qualitative and relative comparisons, tracking time series evolution of normalized figures of merit. Figure 5.6 illustrates the transitions in PL for three representative samples (7, 8, and 10) over the course of one rH cycle. Contrary to the temperature-induced degradation, the initial increase to 70% rH produces a significant enhancement in radiative recombination all samples. As the rH decreases to <5%, a corresponding decrease in PL peak value is observed.

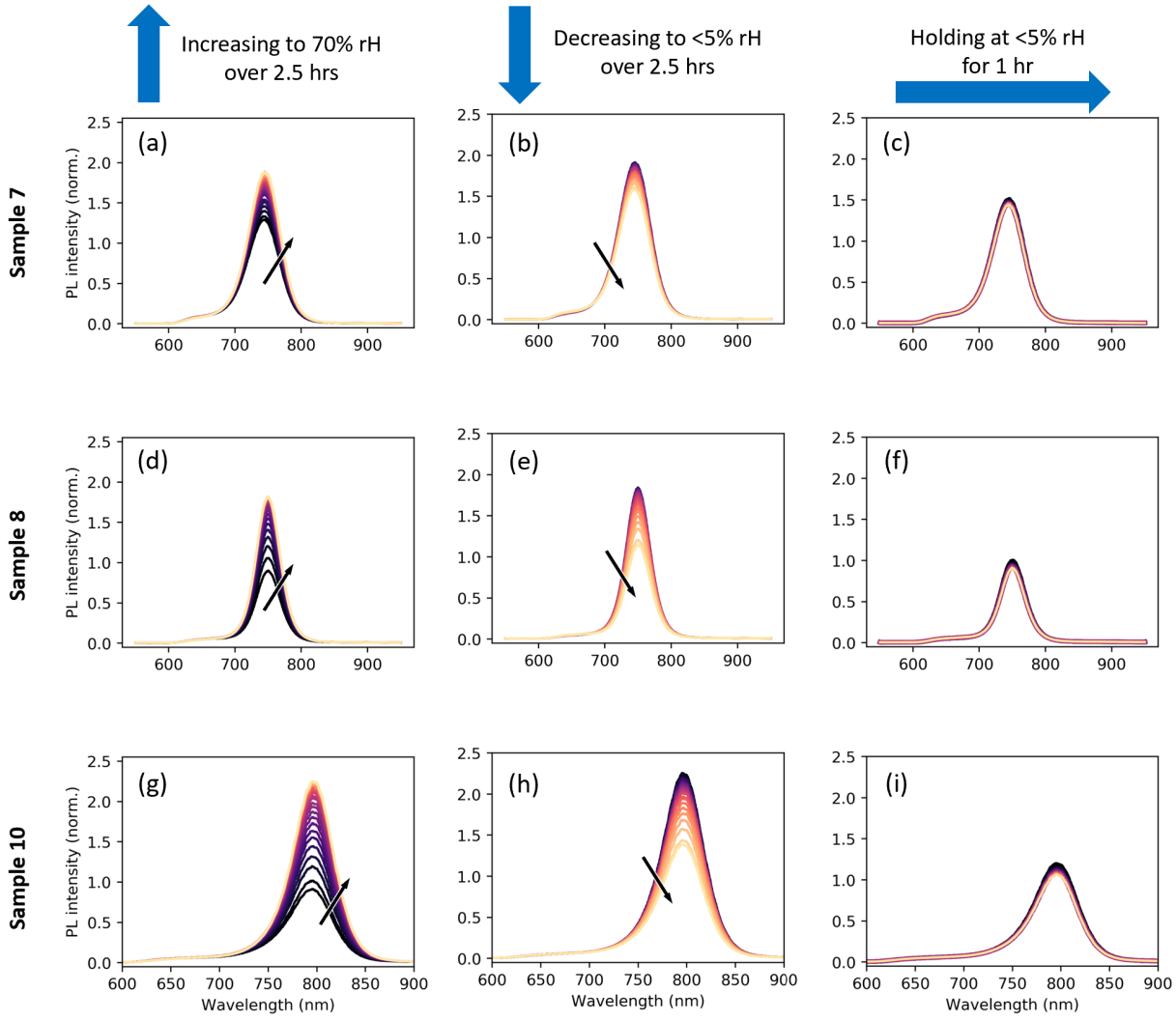

Figure 5.6: **Spectral evolution of PL emission during a single humidity cycle**. PL spectra plotted as the relative humidity (rH) is increased to 70% 2.5 hours, decreased to <5% over 2.5 hours, then held at <5% for 1 hour for samples 7 (a-c), 8 (d-f), and 10 (g-i). Black arrows denote passage of time as the spectrum color changes from purple to beige. Spectra for all samples are collected every 6 minutes.

This result is inverse to the behavior of typical solar cells, which show a loss in performance upon exposure to humid air.[138, 139] However, similar effects have been observed in perovskite material systems. The presence of moisture in the environment passivates trap states located within the semiconductor band gap. This reduces the prevalence of non-

radiative recombination events and gives rise to this seemingly counterintuitive behavior. While the general trend of humidity-induced PL enhancement is consistent for all samples, we observe composition-dependent fluctuations in behavior both across single cycles and over the course of several days of cycling (Figure 5.7). Most samples show an overall increase in the maximum PL intensity over many cycles, in some cases reaching the CCD detector saturation point (sample 5, 10). Higher FA^+ content (samples 5, 8, 10) show high sensitivity to the presence of moisture compared to those with lower FA^+ content (samples 1, 2). The low-FA^+ samples also display a plateau in PL increase after 5-10 rH cycles. Once this plateau is reached, the accumulated PL enhancement after each rH cycle is minimal. Two samples (3, 9) show drastically different behavior. Rather than accumulating PL enhancement over time, the material undergoes a decrease and subsequent plateau. Samples 3 and 9 have intermediate Cs:FA ratios and are located at the extremes in terms of tested halide content, with chemical formulas $(Cs_{3/6}FA_{3/6})Pb(Br_1I_2)$ and $(Cs_{3/6}FA_{3/6})PbI_3$, respectively. Interestingly, the intermediate halide composition $(Cs_{3/6}FA_{3/6})Pb(Br_{1/2}I_{5/2})$ (sample 6) does not display the same trend.

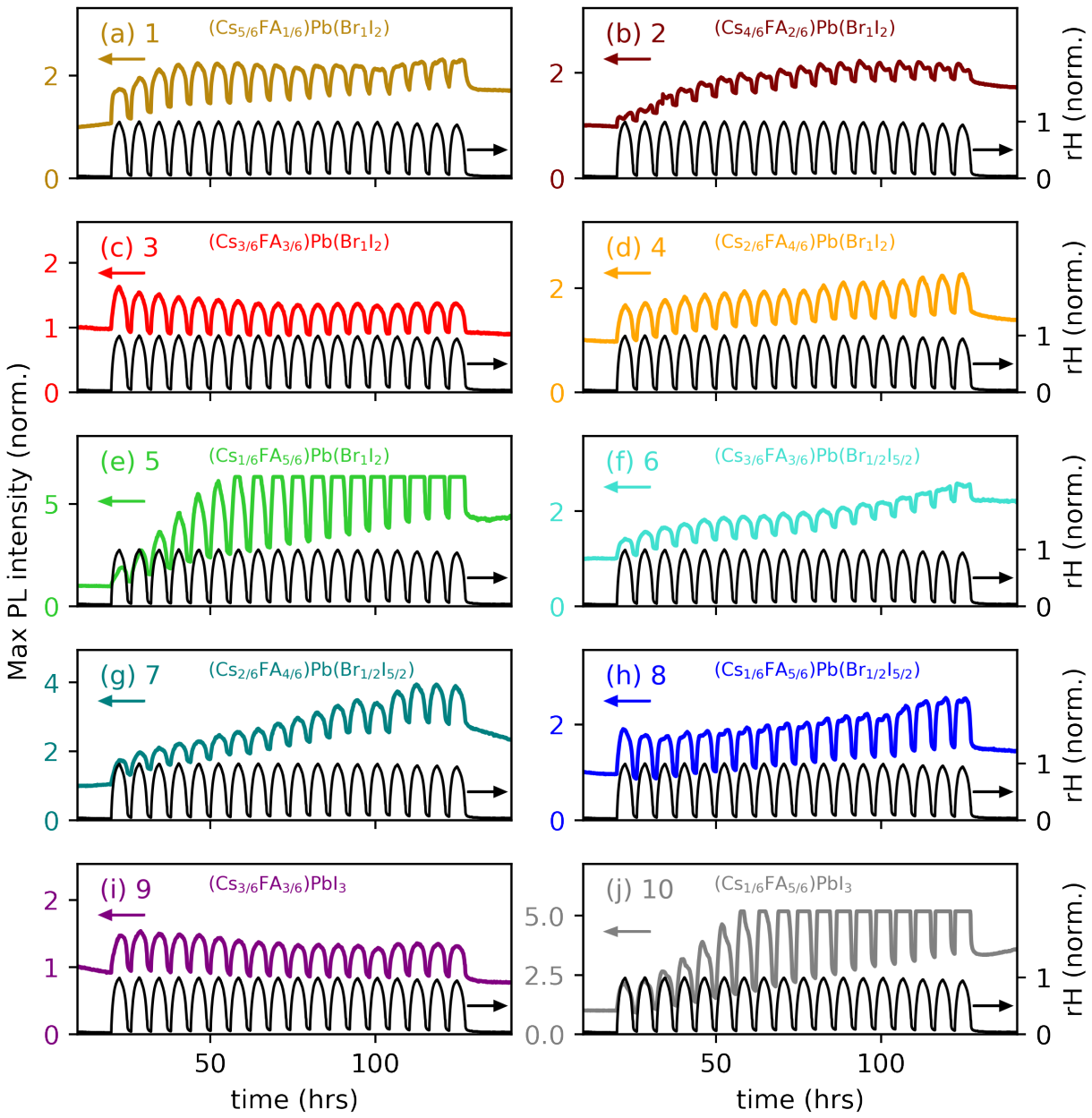

Figure 5.7: **Effect of humidity cycling on PL**. Maximum PL intensity for samples 1-10 (a)-(j) subjected to relative humidity (rH) cycling for 118 hours. The rH profile is shown (black line) on each plot. The left y-axis denotes the normalized PL while the right y-axis is the normalized temperature (colored and black arrows are shown as a guide to the eye). Each 6-hour cycle ranges from <5% to 70% rH while the temperature is held constant at 22°C.

To visualize the long-term spectral evolution from rH cycling, we again plot several spectra taken under identical environmental conditions (rH <5%, T = 22°C) for each sample (Figure 5.8). The spectra shown were acquired after the 2nd, 7th, 12th, and 17th cycles. The final, darkest spectrum was taken after all 18 rH cycles were completed and the samples were held an inert rH <5% condition for 10 hours. Most of the samples (1, 4, 5, 6, 7) exhibit a red shift in PL peak location and a broadening of the PL emission spectrum over repeated rH cycling. The observed peak shift ranges from 10 nm (sample 7) to over 20 nm (sample 1). Notably, the pure-I compositions (samples 9 and 10) show negligible peak shifting. Since I^- is larger than Br^-, it distorts the atomic lattice, weakening atomic orbital overlap and reducing the bandgap. Ion migration in mixed-halide compositions into I-rich and Br-rich domains will thus manifest macroscopically as a decrease in bandgap, a shift to longer PL wavelengths, and a broadening of the emission peak.[77, 129] Therefore, we can attribute the observed multi-cycle trends in peak location and width to likely halide segregation.

In terms of the peak PL value, the A-site composition exerts significant control over the multi-cycle behavior. FA-rich compositions (samples 4, 5, 7, 8, 10) display the greatest moisture-induced enhancement in radiative recombination, while the Cs-rich compositions (samples 1, 2) show limited improvement. Compositions with a 1:1 Cs:FA ratio display contrasting effects, some exhibiting a decrease in PL intensity (samples 3, 9) and one showing a significant increase (sample 6). These trends could be due to local phase segregation, microstructural inhomogeneity and voids, or structural distortions dependent on the Br:I ratio.[19, 129] Further investigation is needed to determine the specific physical mechanisms for PL enhancement and decay in these samples. Our results demonstrate the remarkably complex interplay between rH and PL in perovskite films, which we show is heavily dependent

on both composition and time of exposure.

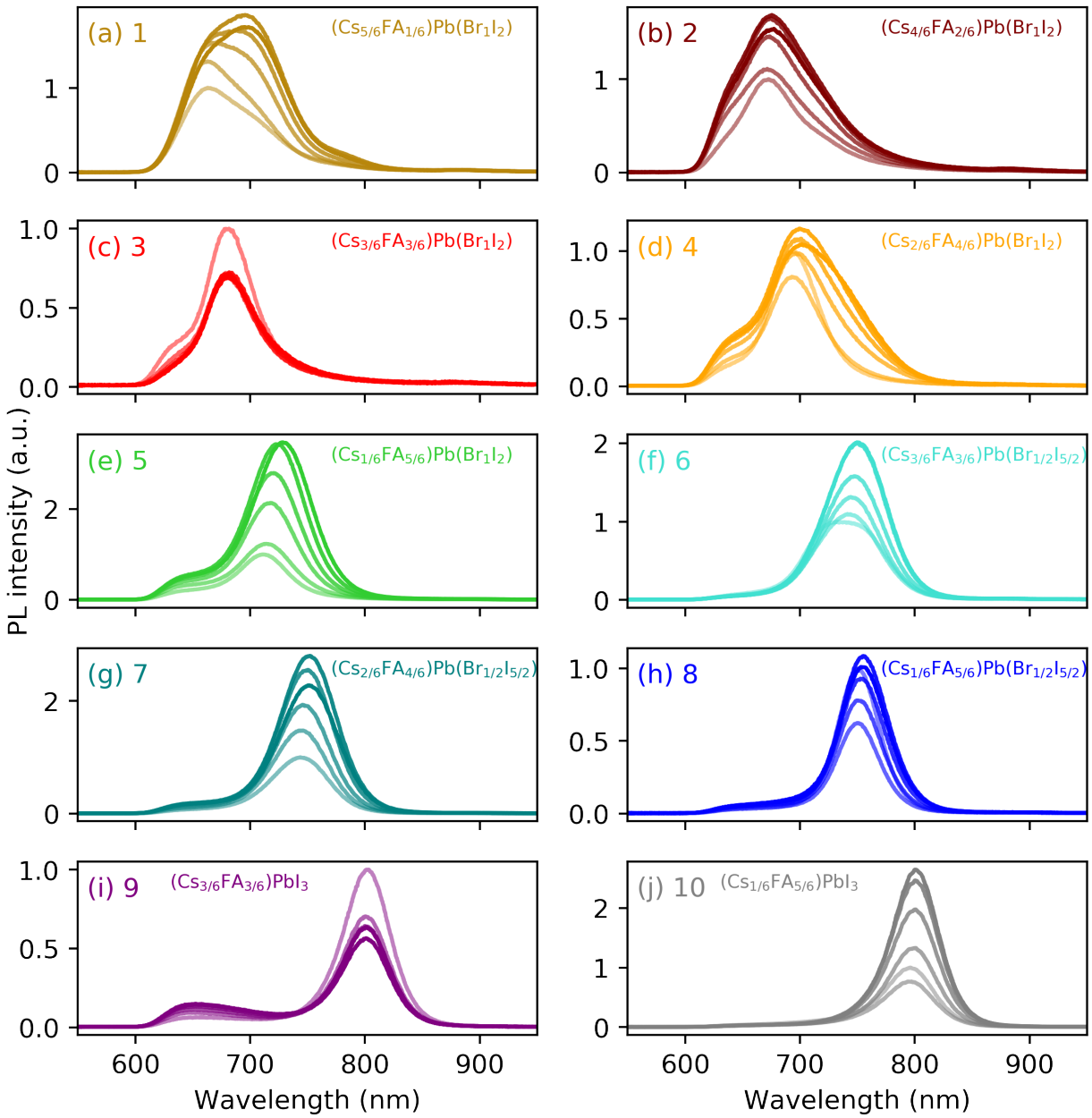

Figure 5.8: **Spectral evolution over 18 humidity cycles**. PL spectra for samples 1-10 (a)-(j) plotted at five time points during the 118-hour experiment. Each spectrum is taken under identical environmental conditions (22°C, rH <5%) after 2, 7, 12, and 17 cycles. The final spectrum is taken after 18 cycles and a 10-hour rest in an inert atmosphere. Black arrows denote the passage of time from the lightest to darkest spectrum.

5.5 Conclusions

To conclude, we have presented a study of environmental PL on 10 Cs-FA-containing lead halide perovskite films of varying composition. We employ a high-throughput optical characterization system using a translatable sample stage to acquire PL spectra from samples subjected to regular temperature and humidity cycling as well as irregular temperature cycling. Conditions were selected to mimic summertime weather in Sacramento, CA and each experiment consists of 8-18 cycles, representing several weeks of typical environmental exposure.

Our temperature-cycling results reveal a strong, near-linear PL response and blue shifting of the peak at high temperature. After 22 cycles of irregular temperature fluctuations, we observe irreversible degradation in several samples. The FA-rich compositions with modest (10-30%) Cs^+ content exhibited less irreversible losses in radiative recombination and greater thermal resistance due to their structural and phase stability. On the halide site, small additions of Br^- (17%) led to faster PL recovery as the increased anionic electronegativity also improves structural stability. Sample 7, composition $(Cs_{2/6}FA_{4/6})Pb(Br_{1/2}I_{5/2})$, showed the most advantageous A- and X-site mixing and recovered 100% of the initial PL output even after 22 cycles of thermal stressing.

The rH-dependent PL also supports the efficacy of mixed-composition perovskites. Most compositions studied showed increases in radiative recombination as band gap trap states are passivated by H_2O. The FA-rich perovskites had the starkest moisture-dependent responses, led by sample 5 and 10 (compositions $(Cs_{1/6}FA_{5/6})Pb(Br_1I_2)$ and $(Cs_{1/6}FA_{5/6})PbI_3$, respectively). The four weakest PL enhancements were all from sam-

ples with 50% or more Cs^+ content on the A-site, with two of these (samples 3 and 9) showing an overall decrease in PL after 18 rH cycles. Our results also show red shifting and broadening of the emission spectra over the course of multiple rH cycles in most of the mixed-halide compositions. This is a signature of halide migration. However, all of these samples still showed an overall PL increase over the course of the experiment. Based on both the temperature and rH results, the FA-rich samples (5, 7, 8, and 10) presented the greatest environmental resilience and consistently high levels of radiative carrier recombination, signaling their potential for use in perovskite PV devices.

The large amount of data presented in this chapter (>10,000 PL spectra per experiment) is also sufficient to train predictive ML models. In the following chapter, we apply various time series forecasting algorithms to the dataset which generate predictions of maximum PL intensity using only the environmental parameters (temperature and rH).

Chapter 6: Quantitative Time Series Forecasts of Perovskite Photoemission

Ensuring long-term stability is the largest remaining hurdle to perovskite photovoltaic (PV) commercialization. Current testing procedures are costly and time-intensive, making them infeasible to conduct for the entirety of the vast perovskite compositional space. Improved material screening processes, which leverage high-throughput data acquisition, automated analysis, and machine learning (ML) pipelines, can greatly accelerate the design process. In this chapter, we apply linear regression, recurrent neural networks, and auto-regressive moving average models to forecast the photoluminescence response in $Cs_yFA_{1-y}Pb(Br_xI_{1-x})_3$ perovskite films subject to temperature and rH cycling. The champion models achieve average errors of $<8\%$ (temperature cycling task) and $<11\%$ (rH cycling task) with forecast windows spanning 8 to 11 day-night cycles. This work demonstrates a broadly applicable ML framework that can be extended to other combinations of environmental stressors and perovskite compositions. Time-series forecasts, in concert with in-depth materials studies and real-world field testing, comprise a rational approach to stable perovskite device development and eventual commercial adoption.

6.1 Introduction to time series forecasting

Perovskite solar cells (PSC) have shown great promise as next-generation PV devices, but their degradation under standard operating conditions hinders their commercial adoption.[140, 141] Studies of PSC stability can last for weeks or months, making it untenable to fully investigate every possible perovskite composition. Machine learning (ML) serves as a toolkit to hasten the vetting and commercialization processes. Specifically, time series predictions of optoelectronic performance based on past behavior can quickly identify which candidate perovskites are likely to remain stable over long periods. This drastically reduces the amount of time needed to identify and thoroughly test promising compositions. Beyond materials screening, time series forecasting has applicability for real-time data analytics of PSC operating in the field. For example, a homeowner with PSC modules could receive an automated forecast of output from the solar system over the following several days and adjust their electricity consumption to better align with times of highest power production. Conceptually, this is similar to checking the weather forecast and planning an outdoor activity on a day with a low chance of rain. These predictions are especially important for PSC, which have reversible degradation pathways and are highly sensitive to changes in environmental conditions such as ambient temperature[75, 88, 89] and relative humidity (rH).[12, 77]

Time series prediction is a common task in ML and has been applied successfully in other energy-centric applications, such as predicting remaining lifetime in batteries based on discharge characteristics,[35] determining future solar irradiance using historical data,[32] and estimating production from Si solar panels from images of cloud cover.[31] However, few

researchers have applied similar techniques to PSC development. Many ML approaches in the field seek to accelerate the compositional screening process, often using simulations or high-throughput data acquisition systems to train the models.[54, 67, 70, 72] Other work includes defect identification and fabrication optimization for spiro-OMeTAD thin films[56, 95] and single point predictions of perovskite film degradation under environmental stress.[76]

Here, we implement time series forecasting models to predict the maximum photoluminescence (PL) emission from mixed-cation, mixed-halide perovskite thin films subjected to temperature and rH cycling. The details regarding the environmental PL measurements are provided in Chapter 4 and 5. Three ML algorithms are applied to the data: linear regression, Echo State Networks (ESN), and Auto-Regressive Integrated Moving Average with eXogenous variables (ARIMAX). Using these computational tools, we generate forecasts of PL performance 8+ cycles into the future with an average normalized root mean square error (NRMSE) of $<8\%$ for the temperature cycling prediction task and $<11\%$ for the rH cycling task. This work expands upon our previous ML research[27, 49] by extending the range of environmental stressors and widening the predictive window. Moreover, we develop computational frameworks that are composition-agnostic, applying identical steps to PL data from perovskites with varied Cs:FA and Br:I ratios. The low average error of our models shows the remarkable ability of ML to generalize across feature spaces and adapt to diverse datasets. This indicates that our methods can be extended to other environmental conditions and perovskite compositional groups, as well as to full PSC devices and, eventually, to operational PV arrays.

6.2 Computational methods

6.2.1 Data preprocessing

As described in Chapter 4, data is acquired in the form of PL spectra at sequential time points. The temperature and rH in the chamber are measured simultaneously and their values are associated with each spectrum. Sampling rates for all experiments were adjusted so that every sample was measured at 6-minute intervals, for a total of 10 spectra per hour per sample. With 10 samples, this amounts to 100 spectra per hour and 14,000 total spectra for our 140-hour experiments.

Data is sorted into a dictionary with keys for each sample ID. The PL .csv files are divided by sample and inserted into the dictionary as wavelength vs intensity. Calculations are performed on each file to extract the maximum PL value (a.u.), the peak location (in nm), the integrated absolute PL (a.u.), and the FWHM (in nm). In summary, each "data point" contains the following information:

(1) Full PL spectral data as wavelength vs intensity

(2) Time at which spectrum was acquired (in minutes, from beginning of the experiment)

(3) Temperature and rH at the time the spectrum was acquired

(4) Spectrum figures of merit (maximum PL, peak location, absolute PL, FWHM)

To prepare the data for ML, we first trim the dataset so that only the hours of temperature or rH cycling are included. In other words, we remove hours at the beginning and end of the dataset where the samples were held in steady environments to equilibrate (see

Figures 5.4 and 5.7). We are left with 132 hours of data for the irregular temperature cycling and 118 hours of data for the rH cycling (Figure 6.1). This is important because our time series forecasting models will learn long-term trends which imitate real-world weather conditions and segments where the environment is artificially held constant will negatively impact learning and predictive capability. Next, we normalize the temperature, rH, and maximum PL such that their values vary from -1 to 1. This is necessary for the neural network activation functions to avoid runaway growth of network weights.[52]

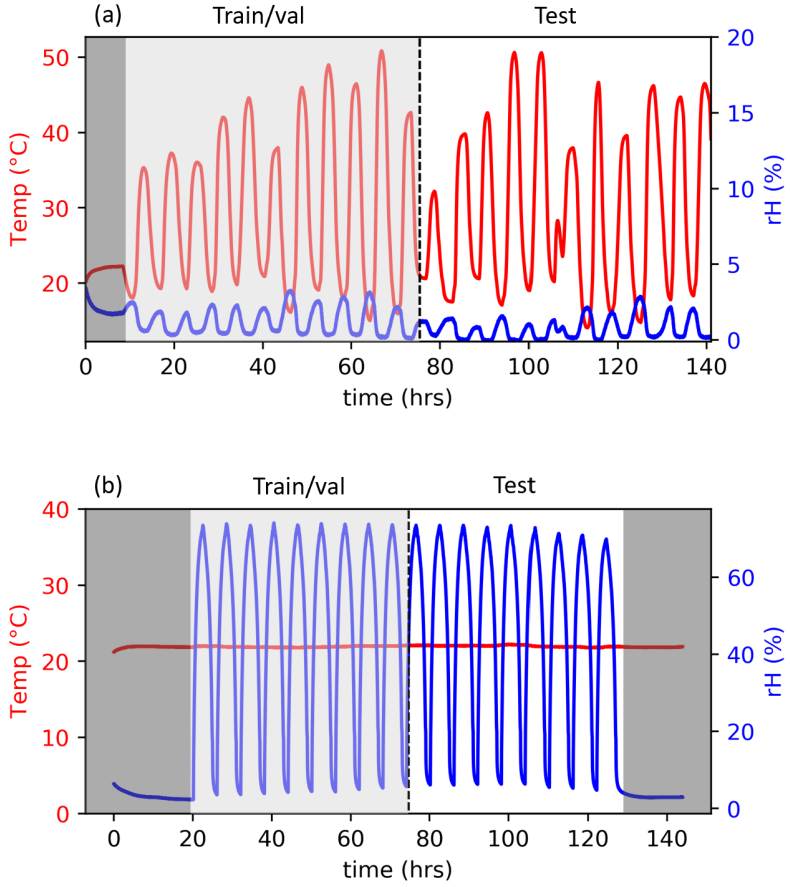

Figure 6.1: **Environmental datasets used for ML**. (a) Temperature cycling and (b) relative humidity (rH) cycling data are split into training/validation and testing sets. The dark gray regions are removed prior to ML model development.

6.2.2 Linear regression predictions on environmental PL data

We apply a baseline linear regression model to the PL time series. Temperature and rH (Figure 6.1) are the sole inputs to the regression. The model is trained on 50% of the data using a least-squares curve fitting method to determine the a, b, and c constants. The remaining 50% of the data is used for testing. The regression equation to predict the PL at time n is as follows:

$$PL_{pred}(n) = a * T(n) + b * rH(n) + c \tag{6.1}$$

The test performance is evaluated using the normalized root mean square error (NRMSE):

$$NRMSE(\%) = 100 * \frac{\sqrt{\sum_{i=1}^{n} \frac{(\hat{y}_i - y_i)^2}{n}}}{y_{max} - y_{min}} \tag{6.2}$$

Where n is the number of data points, $\hat{y}$ is the predicted PL, and y is the experimentally observed PL. The normalization step ($y_{max} - y_{min}$) enables direct quantitative comparison between all ML models.

6.2.3 Echo state network predictions on environmental PL data

An Echo State Network (ESN) is applied to the environmental PL data.[45] We use an open-source Python implementation (pyESN) as our ESN algorithm. See Appendix B for full descriptions of all code used in this chapter. The network contains 250 nodes with a sparsity of 0.1. We use 50% of the data for training and validation and 50% for testing. During training, the ESN updates the network states in a sparsely connected neural network

to minimize the NRMSE. The update equation for each network state (X) is:

$$X(n) = tanh(W_{in}[rH, T(n)] + WX(n-1)) + Cv(n) \tag{6.3}$$

The prediction function is:

$$PL_{pred}(n) = W_{out}[rH, T(n) : X(n)] \tag{6.4}$$

The hyperbolic tangent is used as the activation function for network updates. The network weights – input weight matrix W_{in}, output weight matrix W_{out}, and reservoir weight matrix W – are randomly generated at the start of the training. The update process uses the input weights for the incoming environmental data vector $rH, T(n)$ and the reservoir weights from the previous time step $X(n-1)$. Random noise is added as a regularization parameter to mitigate overfitting, where C is the noise scaling and $v(n)$ is the noise vector. The prediction function uses the output weight matrix, the environmental data vector, and the network states set during training to calculate the PL at time n. Network hyperparameters (noise and spectral radius) are set using a grid search approach on the validation set. The predictive performance is then evaluated using the test set, as will be shown in Section 6.3.

6.2.4 Auto-regressive integrated moving average predictions on environmental PL data

We generate statistical time series forecasting models for the PL data. The Auto-Regressive Integrated Moving Average with eXogenous regressors (ARIMAX) model is used

as the baseline for both the irregular temperature cycling and rH cycling data. In the latter case, we also introduce a seasonality component to the algorithm and use a Seasonal ARIMAX (or SARIMAX) model. The Python statsmodels module is used for implementation of both variants. Again, 50% of the data is used for training and 50% for testing. The (p, d, q) parameters for ARIMAX and the additional (P, D, Q, s) parameters for SARIMAX are determined using stationarity tests and examination of the autocorrelation and partial autocorrelation plots for the training data. The full SARIMAX equation is:

$$\Delta^d \Delta_s^D PL_{t,pred} = \theta(B)^p \Delta^d PL_t + \phi(B)^q \Delta^d \epsilon_t + \beta_{rH} rH_t + \beta_T T_t + \Theta(B)^P \Delta_s^D PL_t + \Phi(B)^Q \Delta_s^D \epsilon_t + \Delta^d \Delta_s^D \epsilon_t \quad (6.5)$$

Where Δ is the differencing operator and B is the backshift operator. Therefore, the $\theta(B)^p \Delta^d PL_t$ term represents a polynomial function with terms for each lagged time step up to p for the differenced time series. The coefficients for each term are included in θ and d is the order of differencing applied to the data. The other terms in the equation are interpreted as follows:

- $\Delta^d \Delta_s^D PL_{t,pred}$: predicts PL value at time t with differencing of order d and seasonal differencing of order D applied
- $\phi(B)^q \Delta^d \epsilon_t$: polynomial function of the lagged error terms with order q, coefficients ϕ, and differencing of order d applied
- $\beta_{rH} rH_t$: rH value at time t multiplied by coefficient β_{rH}
- $\beta_T T_t$: temperature value at time t multiplied by coefficient β_T

- $\Theta(B)^P \Delta_s^D PL_t$: polynomial function of lagged seasonal terms with order P, coefficients Θ, and differencing order of D applied
- $\Phi(B)^Q \Delta_s^D \epsilon_t$: polynomial function of the lagged seasonal error terms with order Q, coefficients Φ, and differencing order of D applied
- $\Delta^d \Delta_s^D \epsilon_t$: error term with differencing of order d and seasonal differencing of order D

For the ARIMAX model, the terms including seasonality (5th and 6th) and all seasonal differencing operators Δ_s^D are removed. During training, all coefficients $(\theta, \phi, \beta_{rH}, \beta_T, \Theta, \Phi)$ are set. The predictive performance is then evaluated using the test set.

6.3 ML results and discussion

6.3.1 Forecasting temperature-dependent PL response

We apply three ML algorithms of varying complexity to time series PL data from $Cs_yFA_{1-y}Pb(Br_xI_{1-x})_3$ perovskites. See the previous chapter for a detailed description of the samples used and the data acquisition methods. Table 6.1 reviews the compositions for the samples, which are numbered 1-10 (see Figure 5.1 for graphical representation of the sample space). Here, we focus solely on computational methods to identify the most promising approach for perovskite time series forecasting. To evaluate how well ML models can predict over a compositional range, we use standardized methods across the sample set. This adaptability is critical given the vast compositional space for metal halide perovskites. The practicality and time effectiveness of ML methods would be severely reduced if different optimization processes requiring human inputs were necessary to train a different model

for every sample (in this case, the human time cost to fit all samples would be increased 10x).

Sample ID	Chemical formula	Br:I ratio	Cs:FA ratio
1	$(Cs_{5/6}FA_{1/6})Pb(Br_1I_2)$	1:2	5:1
2	$(Cs_{4/6}FA_{2/6})Pb(Br_1I_2)$	1:2	2:1
3	$(Cs_{3/6}FA_{3/6})Pb(Br_1I_2)$	1:2	1:1
4	$(Cs_{2/6}FA_{4/6})Pb(Br_1I_2)$	1:2	1:2
5	$(Cs_{1/6}FA_{5/6})Pb(Br_1I_2)$	1:2	1:5
6	$(Cs_{3/6}FA_{3/6})Pb(Br_{1/2}I_{5/2})$	1:5	1:1
7	$(Cs_{2/6}FA_{4/6})Pb(Br_{1/2}I_{5/2})$	1:5	1:2
8	$(Cs_{1/6}FA_{5/6})Pb(Br_{1/2}I_{5/2})$	1:5	1:5
9	$(Cs_{3/6}FA_{3/6})PbI_3$	I^- only	1:1
10	$(Cs_{1/6}FA_{5/6})PbI_3$	I^- only	1:5

Table 6.1: **Sample compositions and ID numbers.**

First, we implement a baseline linear regression algorithm using a 50-50% train-test split. The model uses rH, temperature, and PL training data to determine the regression coefficients. For the test set, rH and temperature datapoints (Figure 6.1a) are inputted to the model, which then generates a PL forecast. The test results are displayed in Figure 6.2 for all samples, where the black line is the regression prediction, and the colored circles are the experimental data. We use the normalized root mean square error (NRMSE) metric, which is scale-invariant and enables direct comparison between models. The predictive performance is highly variable between samples, and the NRMSE values range from 82.8% (sample 1) to 4.9% (sample 7). However, the NRMSE is $<$20% in most cases, and the average across all samples is 24.4%, indicating the general linear correlation between temperature and maximum PL value observed during the experiment. Note that although a separate regression is generated for each sample, the process is completely automated, and the fitting takes $<$0.01 second per sample on a computer with 16 GB of RAM. Therefore, this is a composition-agnostic approach with very high computational efficiency.

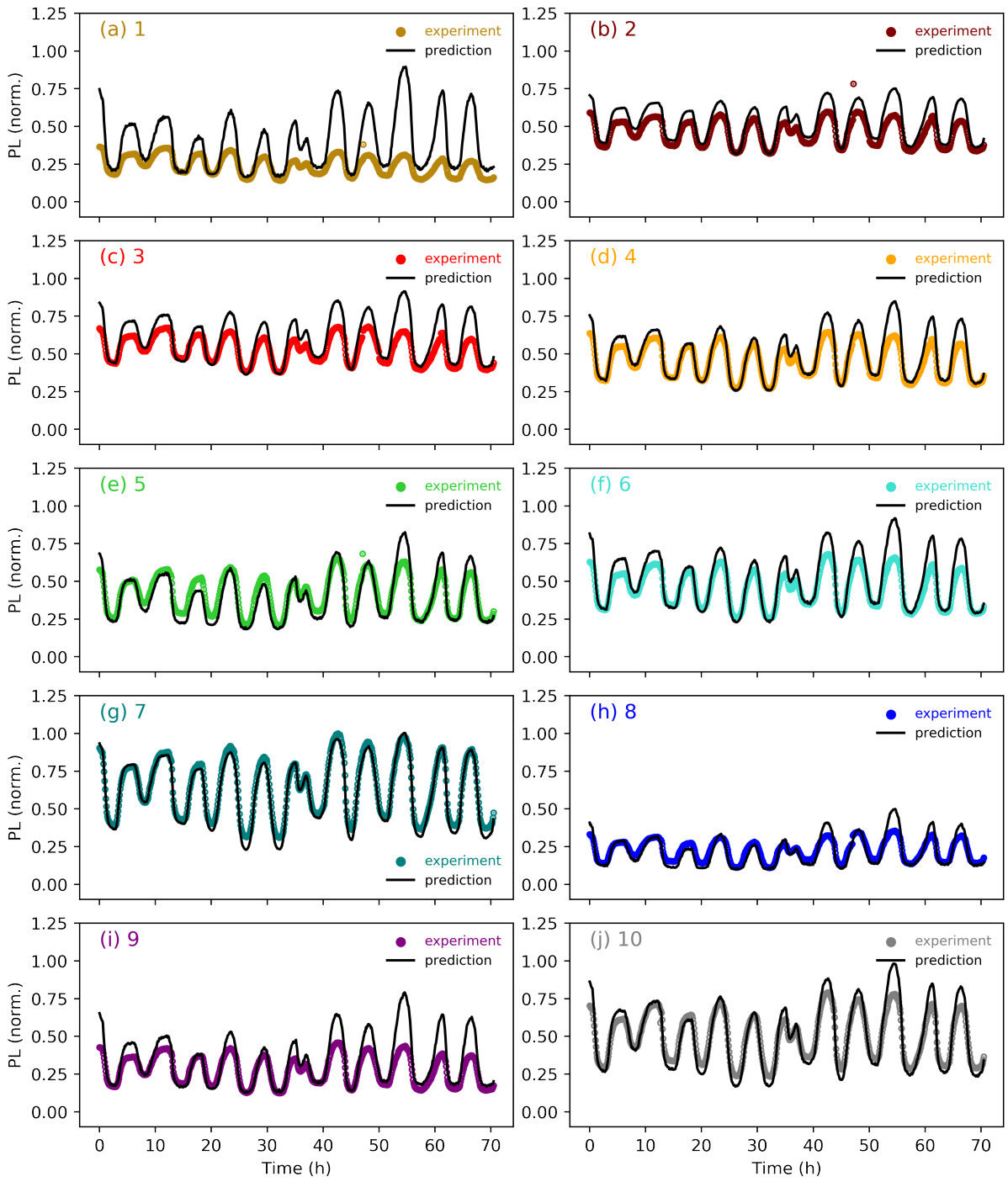

Figure 6.2: **Forecasting temperature-dependent PL using linear regression**. Test set predictions (black lines) and experimental data (colored dots) for samples 1-10 as indicated in each subplot (a)-(j). A 50-50% train-test split is used for all samples. Temperature and rH are the sole inputs to the regression during testing. Average NRMSE is 24.4%.

To improve upon the linear regression prediction accuracy while preserving computation efficiency, we develop Echo State Networks (ESN) to model the data. ESN are a form of recurrent neural network (RNN), where "recurrent" means that the network retains a dynamic memory of past states.[45] This makes RNN uniquely suited to time series analysis and allows them to learn historical trends in the data. ESN have a sparsely connected hidden layer, also called a "reservoir," in which not all neurons are linked to one another (Figure 6.3). This mitigates the vanishing gradient problem, where small values propagated through neural layers in a deep network go to zero as they are repeatedly multiplied. This is an issue because the network learns through gradient descent and requires nonzero gradients for effective. We can solve the problem with sparse connections as in ESN so that small values are not self-multiplied as often and better retained in the network. The structure of ESN also reduces the time required to train the network when compared to other RNN variants. ESN have been successful in time series prediction tasks across many applications, including forecasting fuel cell and battery lifetimes,[33, 34] wind speed,[30, 142] and energy consumption.[143]

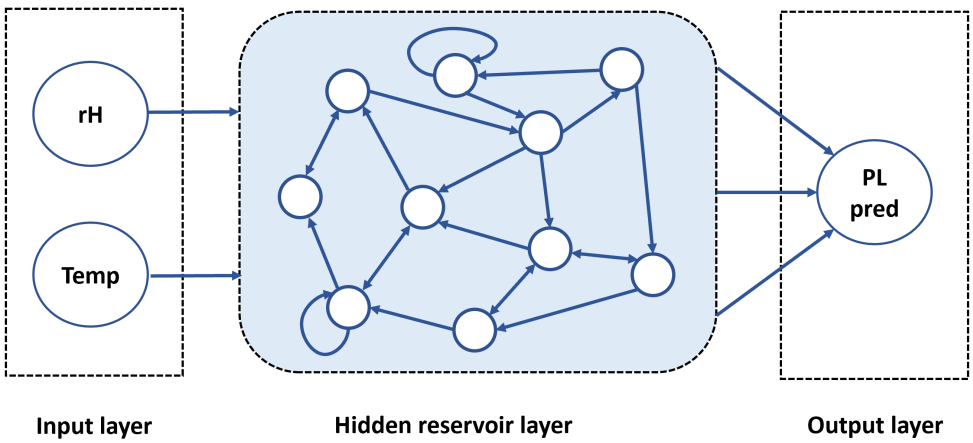

Figure 6.3: **Schematic of Echo State Network (ESN) to forecast environmental PL**. Environmental inputs (rH and temperature) enter a sparsely connected reservoir of neurons which outputs a prediction for the PL value. During training, the network updates the input, reservoir, and output weight matrices to minimize error between its PL predictions and the experimental data. At the testing stage, the weights are constant, and the ESN generates forecasts based only on the rH and temperature data at each time point.

We set aside the latter 50% of the data for testing. For all compositions, we implement a 250-node ESN with a sparsity of 0.1 (meaning 10% of recurrent weights are set to zero). These values were selected based to provide a balance between complexity and computational efficiency.[144] The network has two additional hyperparameters which must be tuned prior to model evaluation. These are noise, a regularization hyperparameter that adds random noise to each neuron, and spectral radius of the recurrent weight matrix, which is a scaling parameter for the matrix eigenvalues. We use a grid search approach to optimize these values for each sample (Figure 6.4). For this process, we subdivide the non-test data into training and validation sets, with a 25-25-50% train-validation-test split. This is a testing-heavy split which we select to probe the limits of ESN in long-term prediction tasks.

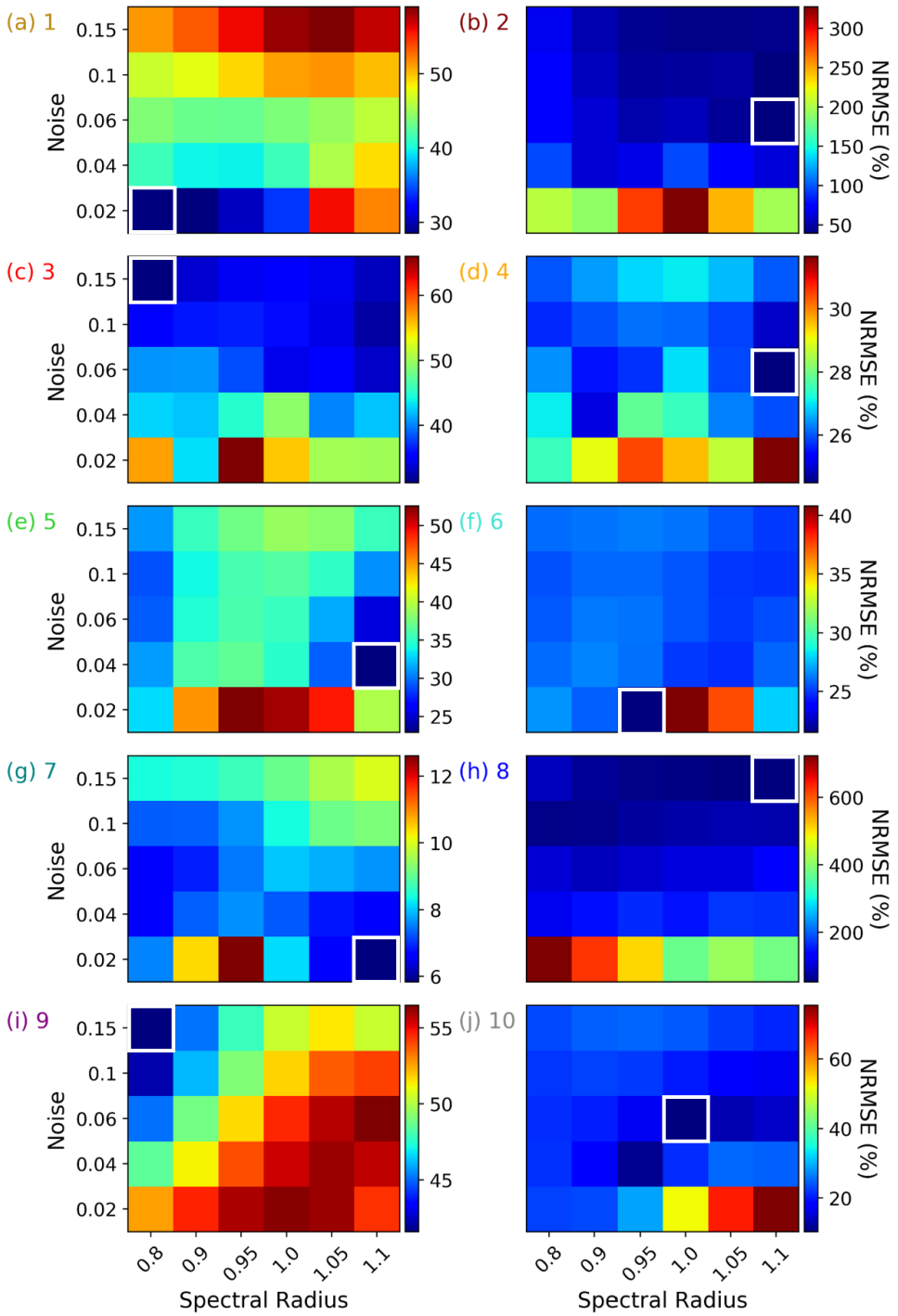

Figure 6.4: **Optimizing ESN hyperparameters for temperature-dependent PL with a grid search approach**. Heatmaps for samples 1-10 as indicated on each subplot (a)-(j). The network is trained on each combination of hyperparameters (noise and spectral radius) and the NRMSE is calculated from validation data predictions. The white boxes indicate the hyperparameters selected for each model.

Figure 6.5 shows the test set performance of the optimized ESN models for each composition. The qualitative fit and consistency of prediction accuracy across samples are both greatly improved from the linear regression results. Quantitatively, the average NRMSE drops to 16.2%, a >30% improvement from the regression. The model still struggles with sample 1 (NRMSE = 50.8%), likely due to the long-term decay exhibited by that sample. Although ESN can learn historical trends, this "memory" is limited and does not encompass the entire 132 hours of data. As in the linear regression, we train and optimize separate models for each composition, but use a standardized, fully automated process. Most of the time is spent on the hyperparameter tuning step, which here requires training and validation for 30 models per sample to fill in all of the hyperparameter combinations seen in the Figure 6.4 heatmaps. Even so, the time to train, optimize, and test each ESN is <4 seconds. These 4 seconds of computational time then yield a 70-hour prediction window with <15% NRMSE for most samples.

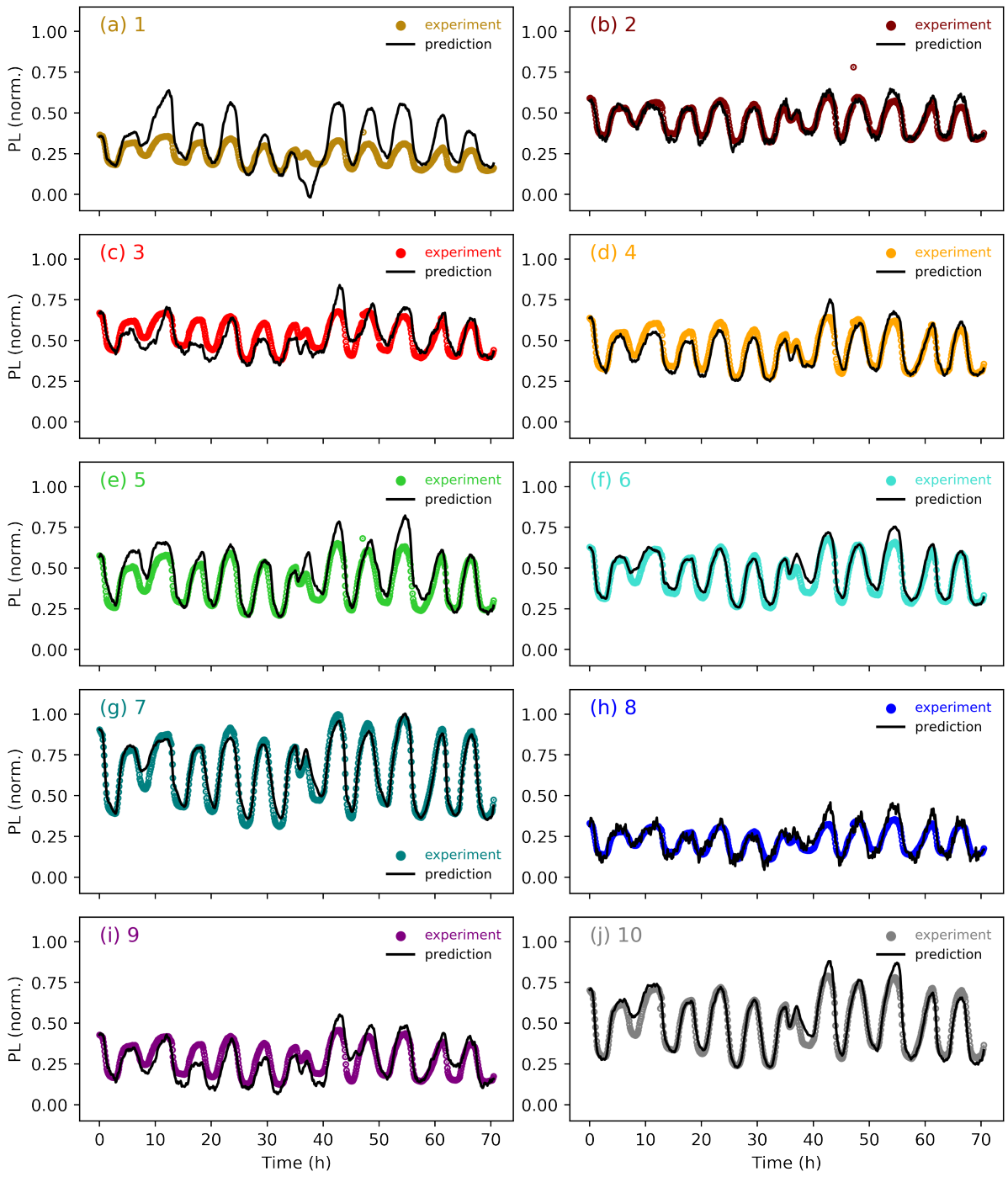

Figure 6.5: **Forecasting temperature-dependent PL using ESN**. Test set predictions (black lines) and experimental data (colored dots) for samples 1-10 as indicated in each subplot (a)-(j). A 25-25-50% train-validation-test split is used for all sample compositions. Temperature and rH are the sole inputs to the network during testing. The ESN also uses past PL values and trends to generate predictions. Average NRMSE is 16.2%

We further refine the predictive performance using a statistical modeling approach: ARIMAX (Auto-Regressive Integrated Moving Average with eXogenous variables).[145] In the clean energy field, variations of auto-regressive moving average models have been employed to create forecasts for wind[142] and PV generation[146] and to predict future electricity prices.[147] Like a linear regression, ARIMAX sets interpretable coefficients during the fitting process, an advantage over black box neural networks like ESN. Each part of the model corresponds to terms in the forecasting equation (see Computational Methods section).[148] Auto-regressive terms (p) are added to incorporate the effects of past PL measurements on the PL at the current time. For example, p=1 adds a term for the PL value at $t-1$ while p=2 adds terms for the PL values at $t-1$ and $t-2$. The integrative parameter (d) corresponds to the order of differencing, where a differenced time series is simply equal to the change between points in the original time series. Moving average terms (q) are similar to auto-regressive terms but relate to the error at past time steps rather than the PL value. Exogenous variables provide additional input to the model and in this case are rH and temperature. See the computational methods (section 6.2.4) for the full ARIMAX equation (Equation 6.5).

Prior to fitting, the (p, d, q) of the ARIMAX model must be set. One common way of determining these values is by deconstructing the time series and visualizing lags between adjacent time steps.[147] Figures 6.6 and 6.7 show the plots used to choose an appropriate (p, d, q). To maintain a composition-agnostic framework as in the linear regression and ESN implementations, we deconstruct only the time series for a single sample and use the results to extrapolate to other compositions. Sample 6 is selected for deconstruction as it has intermediate Cs:FA and Br:I ratios, with a full chemical formula of $(Cs_{3/6}FA_{3/6})Pb(Br_{1/2}I_{5/2})$.

First, the latter 50% of the data is set aside for testing. The training data shows both a long-term downward trend and a strong seasonality (Figure 6.6a). This result is evidence of non-stationarity in the time series, meaning that the mean and variance of the data change over time. For ARIMAX to be effective, we take the first order difference (Figure 6.6b) to obtain a stationary data set. The seasonality is still present in the differenced data, but to keep model complexity low we do not add seasonal components, as these effects will be adequately accounted for by the exogenous temperature variable.

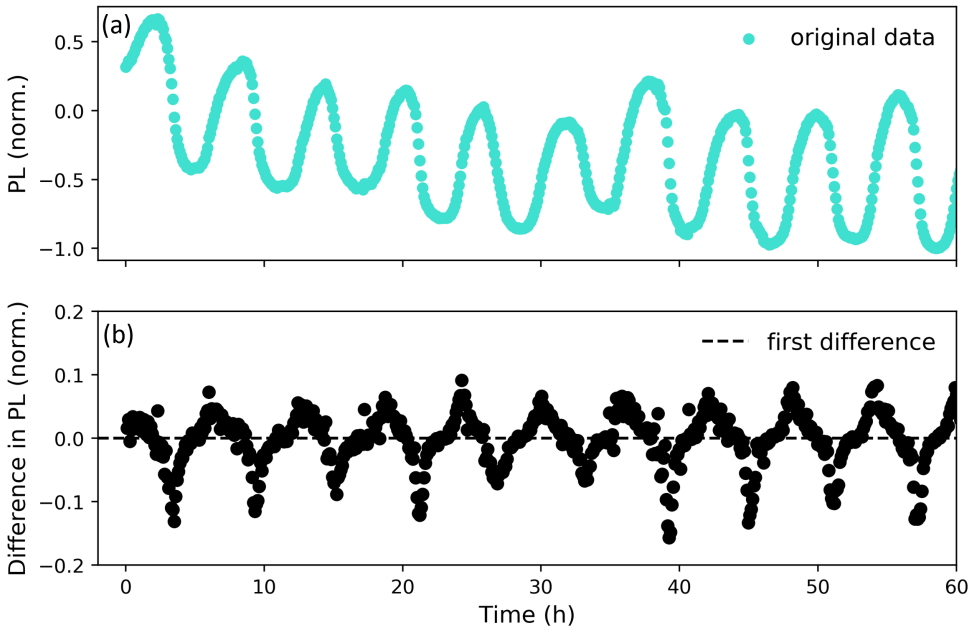

Figure 6.6: **Original and differenced temperature-dependent PL time series for sample 6**. (a) Sample 6 training data after preprocessing. Values are normalized between -1 and 1. A 50-50% train-test split is applied. (b) First order differenced training data. The PL value at the immediately preceding time step is subtracted from each point. The first data point is removed because it has no preceding time step.

To determine the number of auto-regressive and moving average terms to include, we plot the autocorrelation and partial autocorrelation plots for sample 6 differenced training

data (Figure 6.7). The autocorrelations follow the pattern of temperature cycling. Each temperature cycle includes 60 data points, so it is expected to have strong negative autocorrelations at 30 and 90 lags along with strong positive autocorrelations at 60 and 120 lags. However, most of these effects are captured by the exogenous variables. Additionally, the autocorrelation plot includes both direct and indirect effects of lagged data points (for instance, if the PL at lag 2 influences the PL at lag 1 which in turn influences the PL at lag 0, that is an indirect effect). The partial autocorrelation plot (Figure 6.7b) subtracts out the indirect effects, leaving only direct impacts (i.e., the influence of the PL at lag 2 on the PL at lag 0, independent of the PL at lag 1). From this, we can see that only the first two lagged PL values have an impact outside of the 95% confidence interval (blue shaded region). Some later points show partial autocorrelation slightly beyond the shaded region, which we ignore for model simplicity. Based on these observations, we include two auto-regressive terms and zero moving average terms, for a final (p, d, q) of $(2, 1, 0)$.

All 10 samples are fit with ARIMAX $(2, 1, 0)$ models, which are evaluated on the test set data (Figure 6.8) with excellent qualitative accuracy. Although the ARIMAX terms were not optimized for each individual composition, the NRMSE values are similar and the average error is just 7.3%, indicating the flexibility of this computational approach. The time to fit each model is also low (<2 seconds). The ARIMAX function can be interpreted based on the included terms, which are the two exogenous variables (rH, temperature) and two auto-regressive terms (at lag 1 and 2). Therefore, for the differenced time series, highly accurate predictions can be produced based on the environmental conditions at a given time point and from the PL at the two prior time points (which encompass the previous 12 minutes).

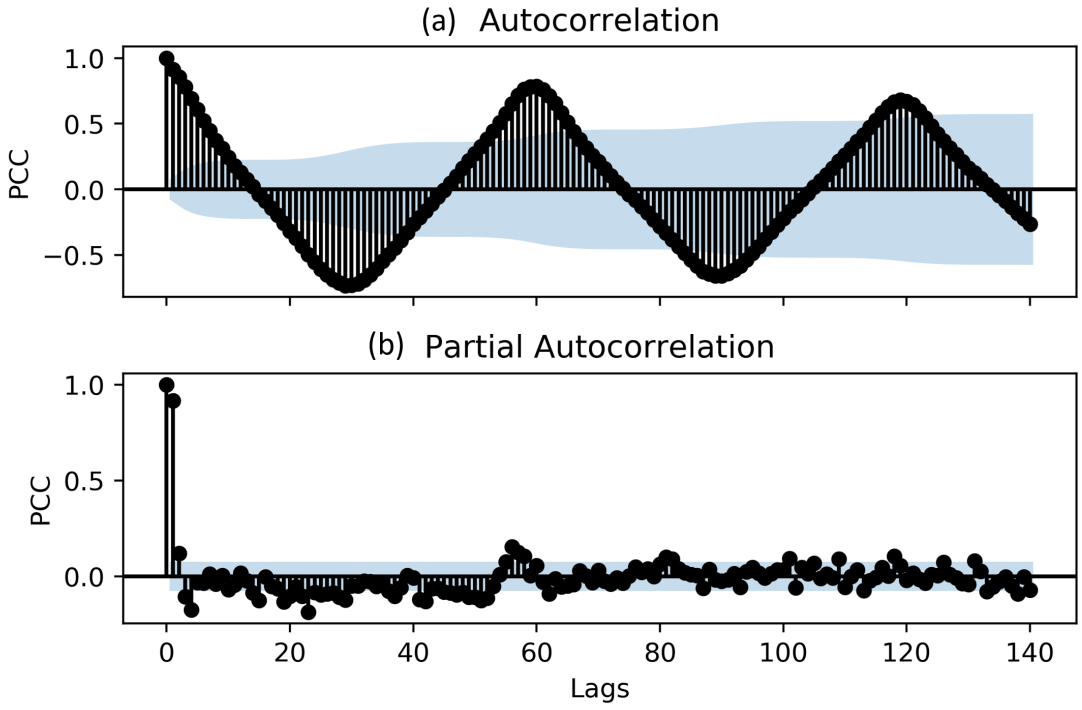

Figure 6.7: **Autocorrelation and partial autocorrelation for the differenced temperature-dependent PL time series**. (a) Pearson correlation coefficient (PCC) between a time point (lag 0) and the 140 preceding time steps in the sample 6 first order differenced training data. Includes both direct and indirect correlations. (b) Direct correlations between a time point and the 140 preceding time steps, with indirect correlations removed. Values at each lag are calculated by subtracting the correlations from all shorter lags (e.g., removing the effect of intervening time steps). The light blue area denotes the 95% confidence interval. Correlations within this interval can be attributed to random fluctuations.

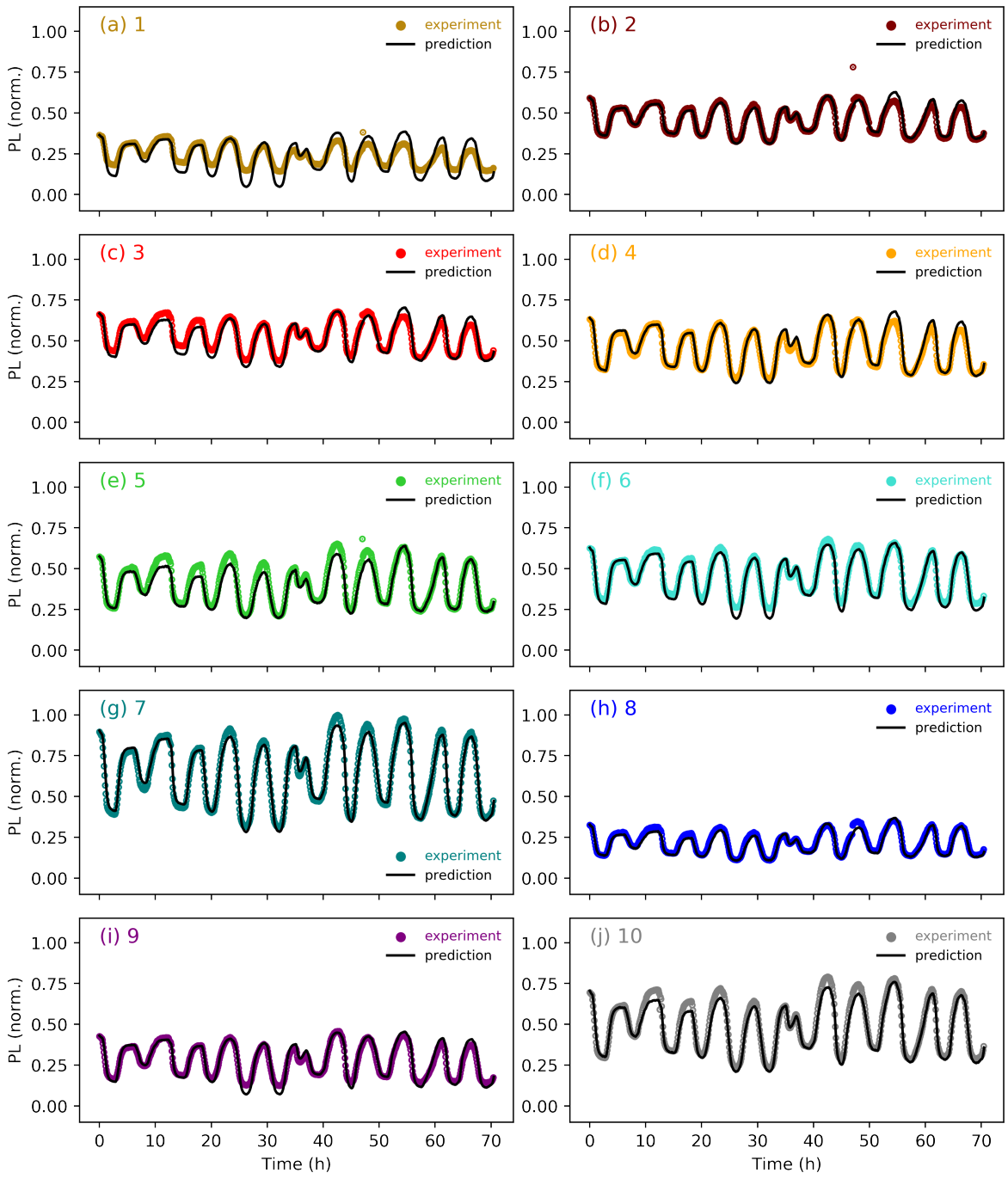

Figure 6.8: **Forecasting temperature-dependent PL using ARIMAX**. Test set predictions (black lines) and experimental data (colored dots) for samples 1-10 as indicated in each subplot (a)-(j). A 50-50% train -test split is used for all sample compositions. Temperature and rH are the sole inputs to the network during testing. The model also includes two auto-regressive terms and one differencing term which use observations at previous time steps. Average NRMSE is 7.3%.

6.3.2 Forecasting rH-dependent PL response

In this Section, we demonstrate the broad applicability of our computational models to various combinations of environmental stressors by applying linear regression, ESN, and ARIMAX to the rH cycling data. The experimental data significantly different from the irregular temperature cycling in that many of the samples show a long-term upward trend which is difficult to predict using simple methods like linear regression and sparsely connected networks with limited memory like the ESN. We omit samples 5 and 10 from computational analysis as saturation of the spectrometer CCD is non-physical and obscures trends in the latter half of the experiment (see Figure 5.7). Following the same training and testing processes as previously, we generate forecasts (Figure 6.9 and 6.11). Heatmaps for ESN hyperparameter tuning are shown in Figure 6.10. The linear regression models present a poor visual fit and have an average NRMSE of 72.5% (Figure 6.9). The ESN performs significantly better with an average of 54.1%. However, this error is still large enough that the ESN completely diverges from the experimental data in some cases (Figure 6.11b, e, f).

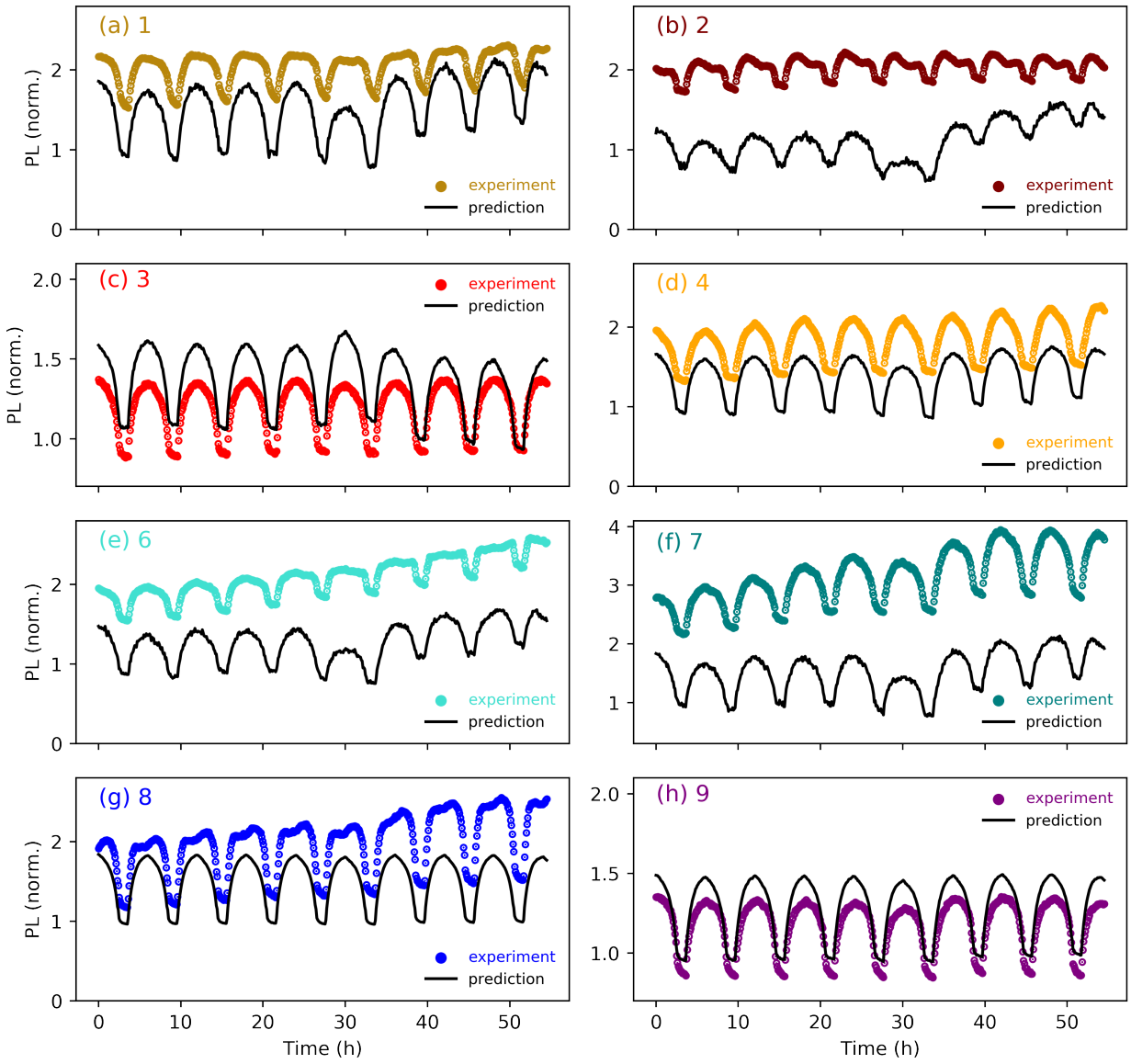

Figure 6.9: **Forecasting rH-dependent PL using linear regression**. Test set predictions (black lines) and experimental data (colored dots) for samples 1-4 and 6-9 as indicated in each subplot (a)-(h). A 50-50% train-test split is used for all sample compositions. Temperature and rH are the sole inputs to the regression during testing. The regression does not account for long-term trends in the data and diverges from the experimental result in most cases. Average NRMSE is 72.5%.

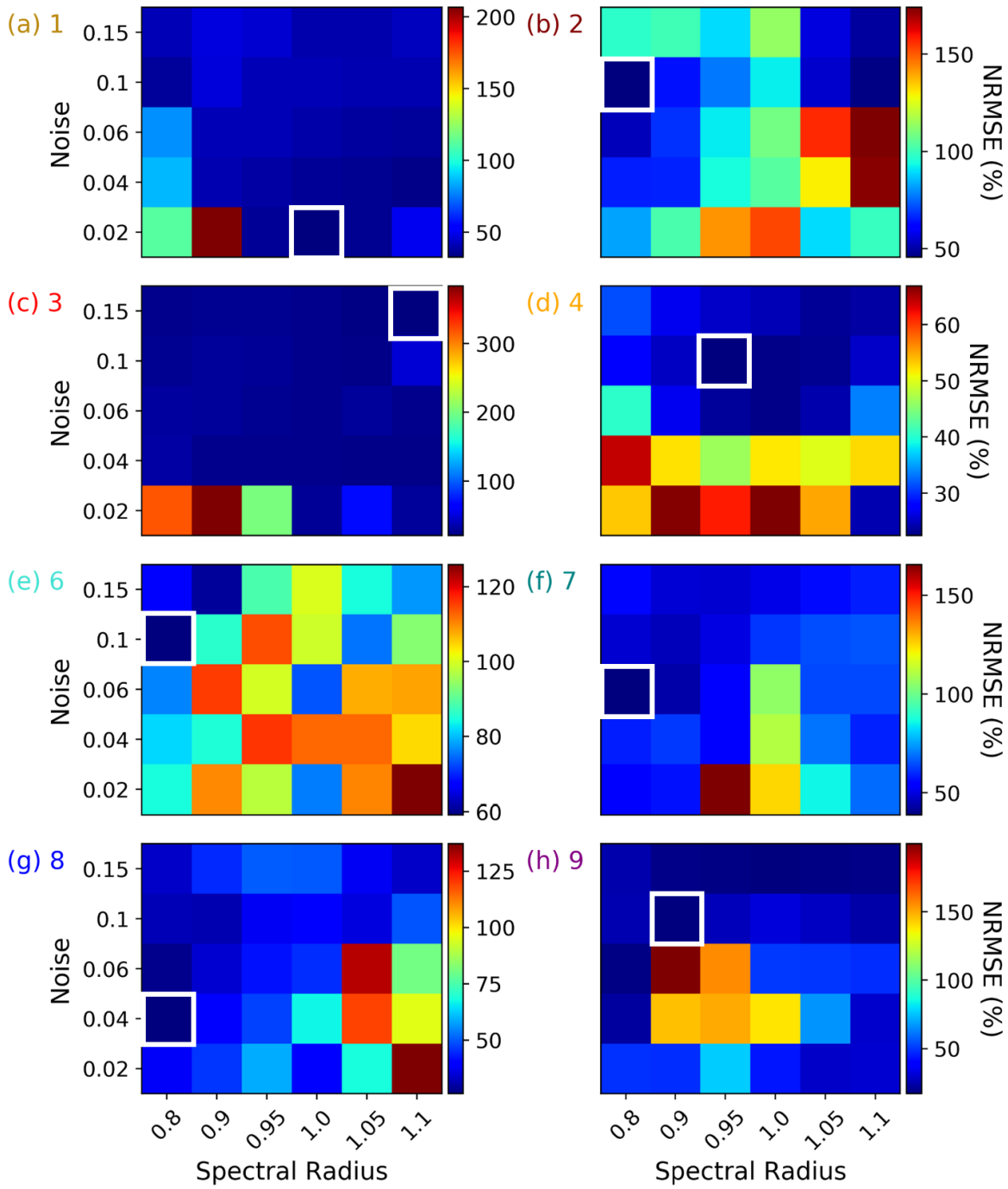

Figure 6.10: **Optimizing ESN hyperparameters for rH-dependent PL with a grid search approach**. Heatmaps for samples 1-4 and 6-9 as indicated on each subplot (a)-(h). The network is trained on each combination of hyperparameters (noise and spectral radius) and the NRMSE is calculated from validation data predictions. The white boxes indicate the hyperparameters selected for each model.

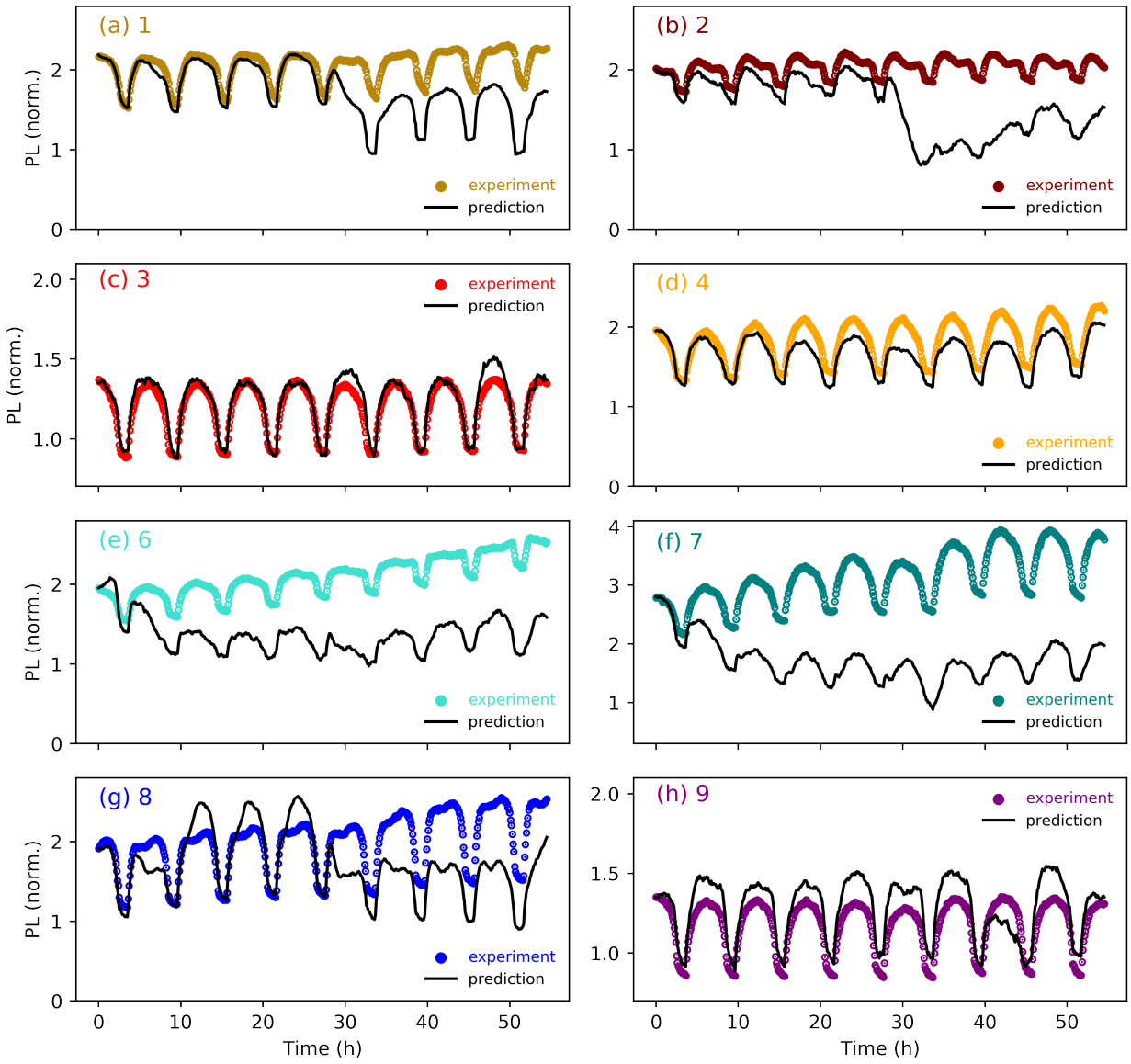

Figure 6.11: **Forecasting rH-dependent PL using ESN**. Test set predictions (black lines) and experimental data (colored dots) for samples 1-4 and 6-9 as indicated in each subplot (a)-(h). A 25-25-50% train-validation-test split is used for all sample compositions. Temperature and rH are the sole inputs to the network during testing. The ESN also uses past PL values and trends to generate predictions but struggles to learn long-term trends and diverges significantly from the experimental results in some cases (a, e, f). Average NRMSE is 54.1%.

To set parameters for the ARIMAX model, we again deconstruct the time series

for sample 6. We add a seasonality component to the algorithm (Seasonal ARIMAX or SARIMAX) since strong long-term trends are present over many rH cycles.[146, 149] The SARIMAX hyperparameters are (P, D, Q, s) where s is the season length – in this case 60 data points (i.e. one 6-hour cycle). (P, D, Q) are equivalent to the ARIMAX (p, d, q) but on the seasonal level, meaning that they are relative to the PL at 60 lags. Taking the first difference of the sample 6 data and applying seasonal differencing (Figure 6.12) effectively creates a stationary time series.

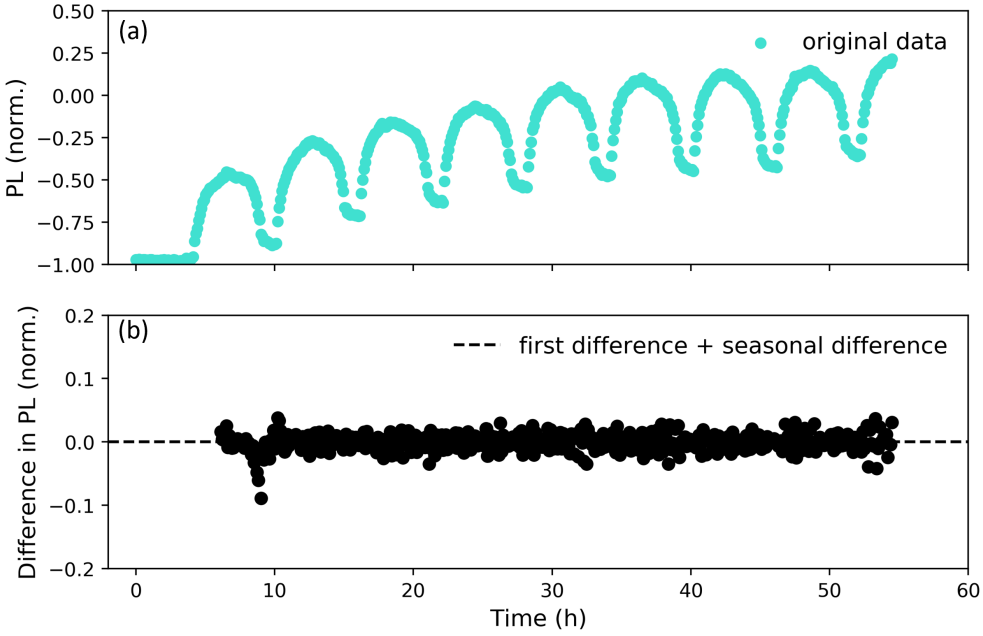

Figure 6.12: **Original and twice-differenced rH-dependent PL time series for sample 6**. (a) Sample 6 training data after preprocessing. Values are normalized between -1 and 1. A 50-50% train-test split is applied. (b) Differenced training data. Two differencing steps are applied. (1) First order differencing: the PL value of the immediately preceding time step is subtracted from each point. The first data point is removed because it has no preceding time step. (2) First order seasonal differencing: the PL value of the time step at lag 60 is subtracted from each point. Lag 60 is selected to match the number of data points in each 6-hour rH cycle. The first 60 data points are removed.

Figure 6.13 shows the autocorrelation and partial autocorrelation for the differenced data. Unlike the differenced temperature cycling data (Figure 6.6), the twice differenced rH cycling data shows negative autocorrelation and partial autocorrelation at lag 1. This is an indication that moving average terms should be introduced.[145] The final SARIMAX selected is $(0, 1, 1)$ $(0, 1, 1, 60)$. The seasonality components increase the computational complexity, and the time to fit the model increases to 60-120 seconds for a 16GB RAM computer. Although significantly greater than the fitting time for the other ML models, this time is still several orders of magnitude lower than the SARIMAX forecasting window (50+ hours). We also caution that exact fitting times depend heavily on the specifications of the PC and how many background processes are running simultaneously. However, the order of magnitude fit time should be consistent across similar devices. The SARIMAX results show excellent visual fit (Figure 6.14) and the average NRMSE is only 10.3%.

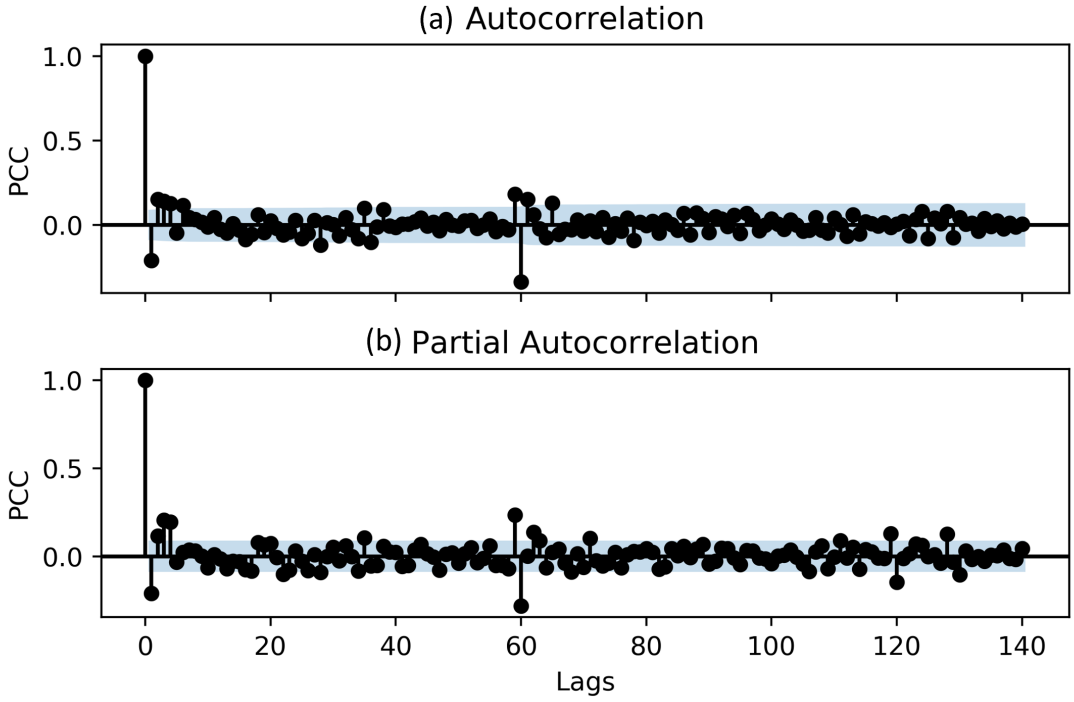

Figure 6.13: **Autocorrelation and partial autocorrelation for the twice-differenced rH-dependent PL time series**. (a) Pearson correlation coefficient (PCC) between a time point (lag 0) and the 140 preceding time steps in the sample 6 differenced training data. Includes both direct and indirect correlations. (b) Direct correlations between a time point and the 140 preceding time steps, with indirect correlations removed. The light blue area denotes the 95% confidence interval. Correlations within this interval can be attributed to random fluctuations.

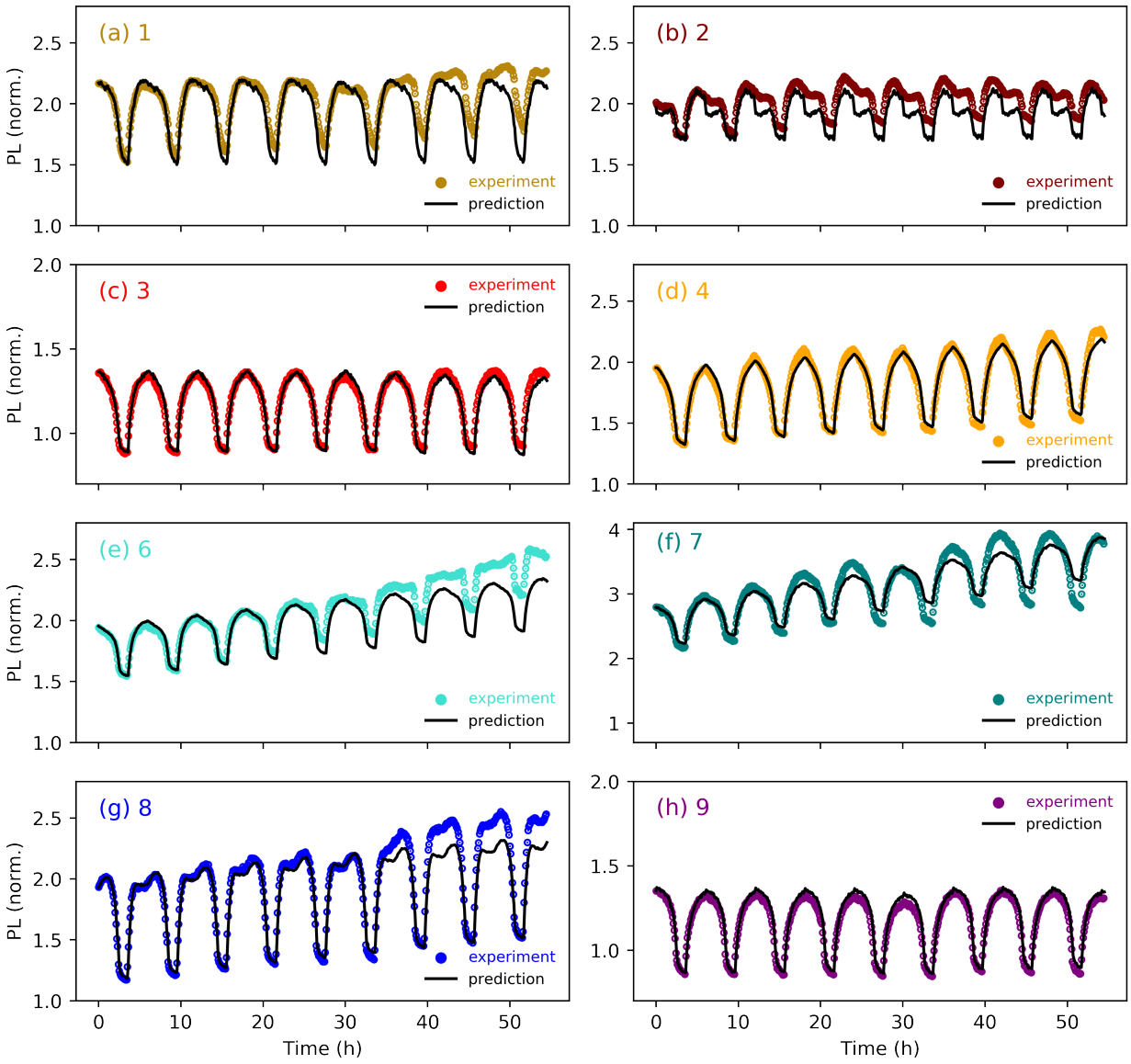

Figure 6.14: **Forecasting temperature-dependent PL using SARIMAX**. Test set predictions (black lines) and experimental data (colored dots) for samples 1-4 and 6-9 as indicated in each subplot (a)-(h). A 50-50% train -test split is used for all sample compositions. Temperature and rH are the sole inputs to the network during testing. The model also includes two differencing steps and two moving average terms which use observations at previous time steps. Average NRMSE is 10.3%.

6.4 Comparison of ML models

A model performance comparison for both the irregular temperature cycling and rH cycling prediction tasks is shown in Figure 6.15. The linear regression models have the highest NRMSE for nearly every sample, followed by the ESN, and finally the (S)ARIMAX. Our results show that linear regression is not an adequate ML approach for non-stationary time series, as expected. The black box nature of neural networks makes analysis of the ESN performance difficult, but the lack of long-term memory in the model is certainly problematic. Other types of RNN could produce higher quality predictions. For example, long short-term memory (LSTM)[46] or gated recurrent unit (GRU)[150] models, which use input and forget gates to remove irrelevant information from the network hidden state while retaining key information. However, the training and hyperparameter tuning process is more complex for these algorithms, and their computational cost must be weighed against any reductions in error.

Some prediction tasks are challenging for every algorithm, specifically sample 1 in the temperature cycling and sample 2 in the rH cycling. For sample 1, we attribute this to the decay in PL over many cycles, a pattern observed strongly in this composition but not in others. The models struggle to identify the uncommon trend, although the ARIMAX still achieves a reasonable error ($<$20%). Physically, the PL loss indicates that irreversible heat-induced degradation occurs in Cs-rich compositions (sample 1 contains the highest proportion of Cs^+). Sample 2 is also Cs-rich and shows unique responses during rH cycling. Even the high-performing SARIMAX model does not perfectly learn the PL peak behavior (Figure 6.14b). The sample 2 pattern has a distinct ridge in PL that occurs in the middle of every

rH cycle. No other sample displays a highly ridged shape, making this another inherently difficult task for any ML algorithm. However, beyond these outlier cases, (S)ARIMAX has excellent predictive capability, <10% NRMSE for temperature cycling tasks and <15% for rH cycling tasks.

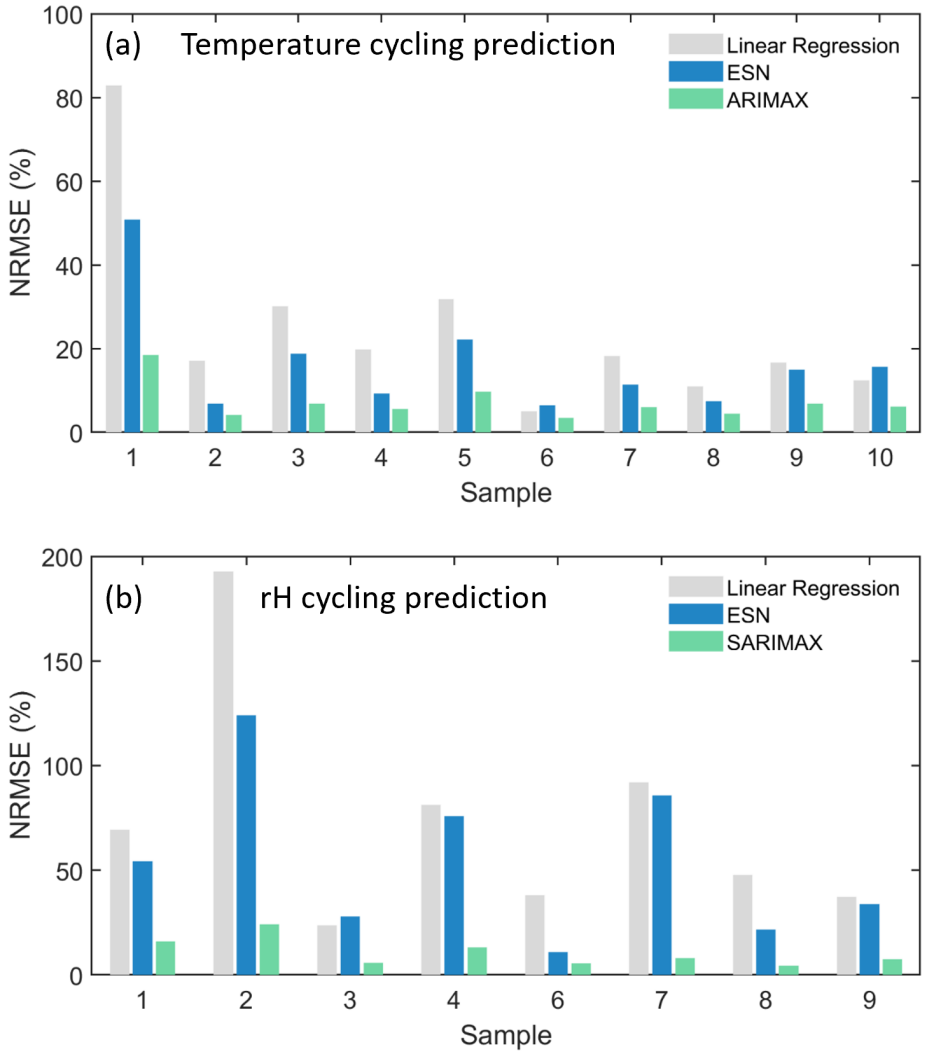

Figure 6.15: **Quantitative comparison of ML algorithms**. NRMSE values of PL forecasts produced by linear regression (gray), ESN (blue), and (S)ARIMAX (green) models. Comparisons are plotted for (a) samples 1-10 during temperature cycling and (b) samples 1-4 and 6-9 during rH cycling.

6.5 Conclusions

In this chapter, we demonstrate the capabilities of ML in forecasting environmental responses in $Cs_yFA_{1-y}Pb(Br_xI_{1-x})_3$ perovskites. Using the temperature and rH cycling data from chapter 5, we train three algorithms: linear regression, ESN, and (S)ARIMAX. We find that all models perform reasonably well on the temperature cycling data, with average NRMSE values of 24.4% (linear regression), 16.2% (ESN), and 7.3% (ARIMAX) over a 70+ hour prediction window (11 day-night cycles). The rH cycling created more non-linear responses in the perovskite films, likely due to the increased complexity of the physical mechanisms involved, including water adsorption and trap state passivation. Patterns in the time series also differed more significantly for the rH cycling, causing lower prediction accuracy for the linear regression (average NRMSE 72.5%) and the ESN (54.1%). We modify the ARIMAX forecasting method slightly by adding seasonality trends and moving average terms to capture the additional complexity in the data. This SARIMAX approach is highly successful and the average prediction NRMSE is only 10.3% over the 50+ hour prediction window (8 day-night cycles). However, the computational cost of adding seasonality terms is substantial, and for environmental stressors with mostly linear PL responses (e.g., temperature), the ARIMAX method is more efficient. In all cases, we use composition-agnostic ML approaches so that human input is only required once. This makes the consistently low (S)ARIMAX error values (<24% for all samples) even more notable.

Our results are extremely promising for future research in perovskite time series forecasting. The generalizability of our methods to multiple compositions can help shorten the time required for compositional tuning, which is currently a major bottleneck in the PSC

design process. We also use PL spectroscopy, a simple, contactless characterization method, exclusively for our models. The high-throughput setup (see Chapter 4) and Python analysis pipelines further simplify acquisition and preprocessing of adequately large datasets for ML. Time series predictions on this data can then serve as a valuable diagnostic tool to easily screen perovskite thin films without the use of expensive, time-consuming measurements. We envision extensions of this work to include other environmental stressors beyond temperature and rH (such as bias, light, and oxygen). Combinations of many stressors can mimic operating conditions in various geographic locations, providing insight into perovskite stability without necessitating lengthy experiments at each individual location.

Chapter 7: Conclusions and Outlook on Perovskite Stability and Machine Learning

In this Thesis, I investigated the effect of two environmental stressors (temperature and rH) on charge carrier recombination dynamics in halide perovskites with varying compositions. To accomplish this, I leveraged standard materials characterization techniques alongside computer science-based tools including high-throughput experimental systems, automated data management and analysis, and ML. Using a custom *in situ* environmental PL setup, I collected over 25,000 spectra (data files), each containing spectrally resolved information that provided physical insight into thermal degradation, moisture-induced passivation, and halide segregation in perovskite thin films. We applied ML to this large data set and developed models that accurately predict future PL output based on environmental conditions and past behavior.

First, we proposed a ML framework for perovskite PV. We review all stages of development: initial compositional screening, material fabrication and optimization, and finally full device design and stability testing. To illustrate our 5-step roadmap, we presented original example projects, which showcase the widespread applicability of ML to different facets of perovskite research and development. This forward-looking perspective seeks to cultivate a synergy between materials science and computer engineering, rejecting random

trial-and-error experimentation in favor of rational, data-driven methods.

To apply the framework to an advanced, large-scale project, a massive data set was required. With this purpose, I designed and built a high-throughput environmental PL system with the capability to collect data from 14 samples during the same experiment. A microelectronics system, coordinated by a Python script that manages a single Arduino, forms the basis for this setup. Using the Arduino-controlled 2-D translation stage and automated data we obtained the tens of thousands of files needed for meaningful ML implementation.

Before the model building, we analyzed and visualized the data and elucidated physical trends across the $Cs_yFA_{1-y}Pb(Br_xI_{1-x})_3$ compositional space, using samples fabricated by the Correa-Baena group at the Georgia Institute of Technology. Ten samples of varied compositions were exposed to temperature and rH cycles which approximated weather during a typical Sacramento summer. Accelerated 6-hour day-night cycles showed that these perovskites are highly sensitive to their environment, both during a single cycle and over the course of many cycles. We found evidence of increased exciton dissociation and non-radiative carrier recombination as samples were heated above room temperature (23°C). Over time, the samples showed both reversible and irreversible degradation, with a strong composition-dependance. FA-rich films were more thermally stable than their Cs-rich counterparts, but the mixed composition $(Cs_{2/6}FA_{4/6})Pb(Br_{1/2}I_{5/2})$ performed best. We confirmed that a Cs^+ content of 10-30% promotes thermal stability by reducing strain in the perovskite structure and optimizing the tolerance factor. Mixed halide compositions also performed well, with small amounts of Br^- suppressing undesired phase changes. Tests after the samples were rested in a dark, inert environment revealed full PL recovery in some compositions, while other compositions recover only 60-70% of their initial absolute PL emission, indicating

irreversible degradation and possible phase changes within the material.

The rH cycling experiment provided further insight into physical processes and carrier dynamics within the perovskite thin films. All compositions displayed PL enhancement due to moisture-induced trap state passivation which reduced instances of non-radiative recombination. Long-term trends showed variability across the compositional space. FA-rich compositions displayed the greatest accumulated PL increases over many rH cycles. Conversely, Cs-rich compositions reached a plateau after 5-10 rH cycles. We also observed peak broadening and PL red shifts, signatures of halide segregation, in many mixed-halide compositions. Our observations evidenced a complex interplay between environment and light emission, which includes both PL-enhancing and PL-reducing mechanisms.

Finally, we linked the environmental PL datasets back to our ML framework. We implemented and compared the accuracy of three time-series forecasting algorithms: linear regression, ESN, and (S)ARIMAX. First, we sorted and pre-processed the data, combining rH, temperature, and PL observations into time-correlated "data points." We then trained and validated the models on the first 50% of each dataset and used the remaining 50% to test their ability to predict the maximum PL value at every time step with only the rH and temperature as inputs. The models obtained average errors of 24.4% (linear regression), 16.6% (ESN) and 7.3% (ARIMAX) on the temperature cycling data. These predictions span over 70+ hours, equivalent to 11 day-night cycles. For the rH cycling, we demonstrated 72.5% (linear regression), 44.0% (ESN), and 10.3% (SARIMAX) error over 50+ hours, representing 8 day-night cycles. For every ML task, we ensured that our methods were composition-agnostic, meaning that the same process could be used for all samples.

The extremely low error for the SARIMAX model is offset by its computational cost and

fitting time, which was 1-2 orders of magnitude longer than that of the ESN. We quantified the consequences of this trade-off by comparing the SARIMAX fitting time to the length of the prediction window. We calculated a 1:1500 ratio between these times, indicating that the fitting process remains highly effective for this task. The ratio could be further optimized by using a computer with >16 GB RAM.

In sum, our results demonstrated the sensitivity of halide perovskites to a multitude of factors – overall composition, site-specific elemental ratios, and environmental conditions (both current and past). Further, we showcased the ability of statistical models like the (S)ARIMAX to extract long-term trends in data and produce accurate predictions for variable compositions without human intervention. Future work could shift to long-term degradation tests under combinations of environmental stressors. Based on our results, mixed-halide, FA-rich compositions with modest amounts of Cs^+ show the most promise for a highly stable performance and eventual commercialization. Specific follow-up experiments of interest include:

(1) Environmental PL on $Cs_yFA_{1-y}Pb(Br_xI_{1-x})_3$ perovskites under simultaneous temperature and rH cycling. Environmental profiles can be selected to mimic diverse climates from around the globe, pinpointing the compositions best suited to each location. ML models can then provide insight into long-term stability considering local weather patterns along with perovskite composition.

(2) Extrapolative ML that can predict PL responses from unseen compositions. This will require data from 30-50 samples to enable computer-generated suggestions of optimal, untested compositions. A feedback loop can couple these predictions with verification experiments to fine-tune the model.

The time series prediction methods presented here can be extended to device level tests as well, where PV figures of merit such as V_{OC}, J_{SC}, fill factor, and efficiency are tracked and forecasted over time. By leveraging high-throughput systems for stability testing, we can obtain data for many samples simultaneously. ML methods can then provide rapid insight into long-term behavior, greatly reducing the time required to vet each device. Furthermore, as PSC are installed in the field, real-time efficiency and power output forecasts can inform homeowner energy use and utility grid management. For example, a warning could be issued when incoming weather conditions are likely to trigger long-term deterioration in the solar cells. Automated systems could then shelter the PSC during the weather event, increasing device lifetimes by ensuring they are not subjected to extreme environmental stress. This is merely one example of the potential that lies ahead in ML-assisted perovskite PV development. Using tools from the fields of data science, robotics, and artificial intelligence, we can capitalize on such opportunities and rationally accelerate the commercialization process of reliable halide perovskite solar cells.

Appendix: A Products of This Research

A.1 Awards and Honors

1. UC Davis Graduate Studies Travel Award	12/2021
2. NSF Graduate Research Fellowship	03/2021
3. Best Poster Award - Conference-wide, 2020 MRS Fall Meeting	12/2020
4. Best Poster Award - Symposium F.EL08/S.CT02, 2020 MRS Fall Meeting	12/2020
5. GEMS Fellowship	09/2020
6. Graduate Assistance in Areas of National Need (GAANN) Fellowship	09/2019
7. Towards Outstanding Postgraduate Students (TOPS) Fellowship	09/2019

A.2 Publications

1. **Srivastava, M.**, Howard, J. M., Gong, T., Dias, M. R. S., Leite, M. S. A machine learning roadmap for perovskite photovoltaics. *Journal of Physical Chemistry Letters*, **12**, 7866-7877 (2021). - **Front Cover**

2. Howard, J. M., Wang, Q., **Srivastava, M.**, Lee, E., Lahoti, R., Gong, T., Abate, A., Leite, M. S. *arXiv pre-prints*, 1-31 (2020).

A.3 Presentations

1. **Srivastava, M.**, Gong, T., Howard, J. M., Leite, M. S. Time-series prediction of perovskite film photoluminescence using machine learning. 2021 MRS Fall Meeting, Boston, MA (11/2021), talk.

2. **Srivastava, M**, Howard, J. M., Gong, T. and Leite, M. S. Advancing metal halide perovskite stability with machine learning. 2021 SPIE Photonics West, Virtual Conference (03/2021), talk.

3. **Srivastava, M.**, Howard, J. M., Gong, T. and Leite, M. S. Machine learning framework for accelerated development of halide perovskites. 2020 MRS Fall Meeting, Virtual Conference (11/2020), poster.

Appendix: B Code Descriptions

B.1 Code used in Chapter 3

In chapter 3, we presented three ML examples. The code and data associated with these examples is available on github (https://github.com/mgsrivastava/ML-perovskites). All code is written in Python and presented in Jupyter notebook format. Here we explain the contents of the notebooks to a non-coding audience, breaking down each part of the process according to our 5-step machine learning roadmap (as described in the main text of chapter 3).

B.1.1 Echo state network for triple-cation PL output

(1) Identify the materials question of interest: The question here is whether we can predict the absolute PL from a triple-cation perovskite thin film based on the ambient humidity level (holding the ambient temperature constant). These predictions would allow us to estimate how well the material would perform in high vs low humidity environments.

(2) Obtain sufficient data for model training: The data for this project was collected using a custom-built environmental sample chamber. PL data was collected in a confocal microscope over three experiments, each lasting 4 hours. This is a small amount of data

for complex ML algorithms like neural networks, so we augment the raw data during the pre-processing step. Note that, in practice, more experimental data is desired for ML implementations (see chapter 5 and 6).

(3) Pre-process the data:

Information about the raw data:

- In total: 720 time-series data points, where each point contains a humidity level and a PL value. Data is in the form of five 4-hour runs of humidity cycling on samples with identical compositions. Each run contains three humidity cycles and 240 data points.

The pre-processing steps are as follows:

- Create a pandas dataframe and load the data.
- Clean the data files (remove gaps, cut to equal duration) and resample such that data points are 15 seconds apart.
- Scale the values for relative humidity (rH) and PL from -1 to 1 (since ML algorithms are sensitive to the relative scale of the features).
- Augment the data using a linear interpolation method. Essentially, this creates several "intermediate" rH-PL runs that are weighted linear combinations of the experimental runs. This routine thus does not introduce any data points outside of the bounds of the raw data. After augmentation, the data set consists of 14400 time-series data points.
- Randomly stitch together the runs, one after another, to create a single (much longer) time-series. This final data set contains over 60 hours of data, and is graphed in the "Data pre-processing" section of this notebook.

(4) Apply feature engineering as needed:

We create additional features for model training:

- Humidity gradient (captures how quickly the humidity is rising or falling)
- Cumulative moisture exposure

(5) Optimize and test the model: The model is constructed using the pyESN open-source implementation of the ESN algorithm. The code is available online in a github repository created by user cknd (https://github.com/cknd/pyESN). The data is split into 80% training and 20% validation sets. Hyperparameters are optimized using a grid search approach, which systematically steps through different hyperparameter values to locate the combination with the lowest validation error. Hyperparameters of interest are:

- Random noise applied to each neuron in the network, serves as a regularization term to mitigate overfitting
- Spectral radius of the recurrent weight matrix which links neurons together

Validation set NRMSE values range from 29.2% (worst case) to 14.3% (best case) depending on hyperparameter selection.

B.1.2 Long short-term memory for MAPI devices

(1) Identify the materials question of interest: The question here is how to forecast long-term degradation in MAPI solar cells under environmental stress (in this case, temperature).

(2) Obtain sufficient data for model training: We use data from the publication: Holzhey, P., et al. A chain is as strong as its weakest link – Stability study of $MAPbI_3$ under light and temperature. *Materials Today* **29**, 10-19, doi:10.1016/j.mattod.2018.10.017 (2019). The authors track solar cell power output over a long time frame (500 hours) for cells held at five different temperatures (-10, 20, 50, 65, and 95°C).

(3) Pre-process the data:

Information about the raw data:

- In total: five 500-hour runs on MAPI solar cell samples, with the temperature held constant throughout each run. Each time-series data point contains the time (in hours) and device power.

The pre-processing steps are as follows:

- Create a pandas dataframe and load the data.
- Clean the data files (cut to equal duration) and resample such that data points are 60 seconds apart.
- Normalize the power data.
- Hold out one entire experimental data file (at 50°C) and set aside for testing.
- Augment the data using a linear interpolation method. Essentially, this creates several "intermediate" temperature-power runs that are weighted linear combinations of the experimental runs. This routine thus does not introduce any data points outside of the bounds of the raw data, and does not include the held out data file. After augmentation, the data set consists of 11000 time-series data points.

- Randomly stitch together the runs, one after another, to create a single (much longer) time-series.
- Split the stitched-together time series into 70% training and 30% validation sets.

(4) Apply feature engineering as needed: We do not use feature engineering in this case.

(5) Optimize and test the model: A long short-term memory (LSTM) model is constructed constructed and trained using the keras deep learning framework. The network architecture consists of:

- Five input units
- A leaky rectified linear unit (ReLU) as the activation function
- A dropout layer to mitigate overfitting
- A dense layer to output the prediction

Interested readers can find more information about each of these layers at https://www.tensorflow.org/api_docs/python/tf/keras/layers. The LSTM is trained over the course of 200 epochs, where each epoch invovles stepping through all of the training and validation data. Finally, the model is evaluated on the unseen test set: the experimental run at 50°C that was held our prior to data augmentation and training. The LSTM predicts the entire 500 hour time-series with an NRMSE of only 5.5%.

B.1.3 Convolutional neural network for HTL conductance

(1) Identify the materials question of interest: The question here is whether we can predict the conductance value for PSC hole-transport layers (Spiro-OMeTAD) based on optical images alone. Such a prediction links optical and electronic properties, and can save time by reducing the number of characterization steps necessary to evaluate each thin film.

(2) Obtain sufficient data for model training: We use data from the publication: MacLeod, B. P., et al. Self-driving laboratory for accelerated discovery of thin-film materials. *Sci Adv* **6** (2020). The authors use high-throughput robotic synthesis and characterization to quickly acquire large amounts of data.

(3) Pre-process the data:

Information about the raw data:

- In total: 2x35=70 samples
- For each sample, there are 7 different I-V data for conductance measurement taken at different location (70x7=490).
- For each sample, there are 3 images for spin-coated Spiro-OMeTAD layer after annealing (70x3=210), taken from different areas of the sample. All the original image files are of the size (4000, 3000) for width and height, respectively.

The pre-processing steps are as follows:

- For each sample, average the 7 different conductance data for labeling.
- Duplicate each conductance data point twice, so they align with the image data.

- Normalize the conductance data.
- Convert the PIL image instances into numpy array.
- Split the data into train and test sets.

(4) Apply feature engineering as needed: We do not use explicit feature engineering, but we do augment the data through random rotations, width and height shifting, flipping, and zooming of the raw data images. This is a very common practice for machine vision tasks, where it is essential to provide the model with representative training data (ideally this will encompass all types of images the model may encounter during later testing and usage).

(5) Optimize and test the model: The convolutional neural network (CNN) is constructed and trained using the keras deep learning framework. The network architecture consists of:

- Three 2D convolution layers (3x3x32, 3x3x64, 3x3x64), each followed by a max pooling layer (2x2)
- Regularization for each convolutional layer to mitigate overfitting
- Two fully connected layers (100 and 64 in size)
- Single-value output layer that predicts conductance for each image

Interested readers can find more information about each of these layers at https://www.tensorflow.org/api_docs/python/tf/keras/layers. The model is trained on 64% of the data. 16% of the data serves as the validation set. Finally, the CNN is evaluated on

the remaining 20% of the data (test set). Our final CNN is able to predict conductance values with an NRMSE of 21% based on dark field images alone, an impossible task for human visual analysis. The CNN_data_analysis notebook contains further visualization of the model results.

B.2 Code used in Chapter 6

In chapter 6, we applied three types of ML algorithms to the environmental PL datasets presented in chapter 5. The code and data associated with these examples is available upon request to the author. All code is written in Python and presented in Jupyter notebook format. Here we explain the contents of the notebooks to a non-coding audience. Steps are in chronological order as presented in the Jupyter notebooks.

B.2.1 Functions and models

This notebook contains data processing and scaling functions as well as the ESN implementation code. The code in this notebook is utilized by both notebook 2 and 3.

B.2.2 Time series forecasts on temperature cycling data

(1) Load and visualize the environmental data (rH, temp): This data was pulled from a sensor placed inside the sample chamber and recorded by the Arduino. We use the plot to determine how much data must be "trimmed" from the beginning and end of the experiment (see Figure 6.1).

(2) Sort and process the data:

Information about the raw data:

- In total: 15,920 data files (1592 per sample, 10 samples).
- Files are in .csv format.
- Each file contains data for a single PL spectrum. There are six columns of data, but we only need the wavelength (third column) and PL intensity (sixth column).

Processing steps are as follows:

- Navigate to the PC directory where the data files are stored.
- Create a pandas dataframe (full_PL_df) which will be populated by all of the data, sorted by sample ID.
- Use pandas to step through each PL .csv file.
  - Drop the unnecessary data columns, retaining only the wavelength and intensity. Store these as a dataframe (PL_df).
  - Label the wavelength vs intensity data with a number (file_num) indicated when it was acquired.
  - Calculate the time at which the spectrum was acquired (in minutes, from the beginning of the experiment).
  - Calculate figures of merit for the wavelength vs intensity data. These are the maximum PL (maxPL), FWHM (fwhm), PL peak location (peak_loc), and the area under the PL curve (peak_area).

  - Add the PL_df, maxPL, fwhm, peak_loc, peak_area, and time_min to the full_PL_df under the appropriate sample ID.

- Once all .csv files have been processed, the full_PL_df is returned. We will use this dataframe extensively for analysis and visualization.

(3) Visualize the data: We plot the first spectrum from all samples to quickly view the relative peak locations and shapes. Next, we visualize the spectral evolution of PL emission by selecting spectra at 0, 10.5, 58, 82, and 137 hours and plotting these for each sample. We also plot the maximum PL value (normalized according to the first point) for each sample along with the temperature profile. Finally, we plot spectra after a 12 day post-experiment rest in a dark, N_2-filled environment. We calculate the recovery % for each sample. See chapter 5 for an analysis of the data trends.

(4) Scale the data: This is the final pre-processing step before ML. We scale the rH, temperature, and PL data such that the values for each are between -1 and 1. We populate a new pandas dataframe for ML purposes. This dataframe contains the following, for each sample:

- The scaled environmental data
- Scaled maximum PL values, time-correlated with the environmental data
- The scaler function used on the PL data

(6) Linear regression: We implement a linear regression model for each sample using a 50-50% train-test split. We use the curve_fit() function from the SciPy open-source Python library for model fitting. Finally, we visualize the testing results (Figure 6.2)

(7) Echo state network: We implement Echo State Network (ESN) neural networks for each sample using a 25-25-50% train-validation-test split. We use the pyESN open-source implementation. The code for pyESN is reproduced in our "functions_and_models" notebook. It is also available online in a github repository created by user cknd (https://github.com/cknd/pyESN).

First, we tune the hyperparameters for each sample. We use a grid search approach to find the optimal spectral radius and noise values, which we store in numpy arrays (min_radius, min_noise). During this process, we use 25% of the data for training and 25% for validation (i.e., to calculate the NRMSE for a given set of hyperparameters). The remaining 50% of data is not used or seen by any of the models. The two lines using the train_test_split() function from the scikit-learn (sklearn) ML library create the three data sets. We visualize the testing results. Using the previously selected hyperparameters, ESN for each sample generate predictions on the test data (Figure 6.5).

(8) ARIMAX: Several steps are required to train the ARIMAX. Refer to chapter 6 for detailed discussion and analysis of each step. Brief descriptions are provided below.

- Visualize the seasonal decomposition of the sample 6 data
- Plot the original and first-differenced sample 6 data
- Plot the autocorrelation (acf) and partial autocorrelation (pacf) for the first-differenced sample 6 data
- Based on the acf and pacf, we select model order (p, d, q) to be (2, 1, 0)

We then fit ARIMAX (2, 1, 0) models on the training data for each sample. We use a 50-50%

train-test split. Finally, we evaluate and visualize the test set performance of the ARIMAX models (Figure 6.8).

(9) Model comparison: We print the list of test errors for each model on all samples. We also calculate and print the average error for each model. See Figure 6.15a for visual comparison.

B.2.3 Time series forecasts on rH cycling data

(1) Load and visualize the environmental data (rH, temp):

Identical procedure as used for temperature cycling data (Appendix B.2.2).

(2) Sort and process the data:

Identical procedure as used for temperature cycling data (Appendix B.2.2).

(3) Visualize the data: We plot the first spectrum from all samples to quickly view the relative peak locations and shapes. Next, we visualize the spectral evolution of PL emission by selecting spectra at 0, 32, 63, 92, 122, and 143 hours and plotting these for each sample. We also plot the maximum PL value (normalized according to the first point) for each sample along with the temperature profile.

(4) Scale the data:

Identical procedure as used for temperature cycling data (Appendix B.2.2).

(6) Linear regression:

Identical procedure as used for temperature cycling data (Appendix B.2.2). See Figure 6.9 for test set predictions.

(7) Echo state network:

Identical procedure as used for temperature cycling data (Appendix B.2.2). See Figure 6.11 for test set predictions.

(8) SARIMAX: Several steps are required to train the SARIMAX. Refer to chapter 6 for detailed discussion and analysis of each step. Brief descriptions are provided below.

- Visualize the seasonal decomposition of the sample 6 data
- Plot the original and first-differenced sample 6 data
- Plot the autocorrelation (acf) and partial autocorrelation (pacf) for the first-differenced sample 6 data
- Based on the acf and pacf, we select model order (p, d, q)(P, D, Q, s) to be (0, 1, 1)(0, 1, 1, 60)

We then fit SARIMAX (0, 1, 1)(0, 1, 1, 60) models on the training data for each sample. We use a 50-50% train-test split. Finally, we evaluate and visualize the test set performance of the SARIMAX models (Figure 6.14).

(9) Model comparison: We print the list of test errors for each model on all samples. We also calculate and print the average error for each model. See Figure 6.15b for visual comparison.

Bibliography

[1] O. Wallach, "Race to net zero: Carbon neutral goals by country," 2021. Accessed: December 8, 2021.

[2] "Electric power annual 2020," report, U.S. Department of Energy, 2020.

[3] M. S. Chowdhury, K. S. Rahman, T. Chowdhury, N. Nuthammachot, K. Techato, M. Akhtaruzzaman, S. K. Tiong, K. Sopian, and N. Amin, "An overview of solar photovoltaic panels' end-of-life material recycling," *Energy Strategy Reviews*, vol. 27, 2020.

[4] A. K. Jena, A. Kulkarni, and T. Miyasaka, "Halide perovskite photovoltaics: Background, status, and future prospects," *Chemical Reviews*, vol. 119, no. 5, pp. 3036–3103, 2019.

[5] J. Cao and F. Yan, "Recent progress in tin-based perovskite solar cells," *Energy Environmental Science*, vol. 14, no. 3, pp. 1286–1325, 2021.

[6] E. L. Unger, L. Kegelmann, K. Suchan, D. Sörell, L. Korte, and S. Albrecht, "Roadmap and roadblocks for the band gap tunability of metal halide perovskites," *Journal of Materials Chemistry A*, vol. 5, no. 23, pp. 11401–11409, 2017.

[7] M. V. Khenkin, E. A. Katz, A. Abate, G. Bardizza, J. J. Berry, C. Brabec, F. Brunetti, V. Bulović, Q. Burlingame, A. Di Carlo, R. Cheacharoen, Y.-B. Cheng, A. Colsmann, S. Cros, K. Domanski, M. Dusza, C. J. Fell, S. R. Forrest, Y. Galagan, D. Di Girolamo, M. Grätzel, A. Hagfeldt, E. von Hauff, H. Hoppe, J. Kettle, H. Köbler, M. S. Leite, S. Liu, Y.-L. Loo, J. M. Luther, C.-Q. Ma, M. Madsen, M. Manceau, M. Matheron, M. McGehee, R. Meitzner, M. K. Nazeeruddin, A. F. Nogueira, Odabaşı, A. Osherov, N.-G. Park, M. O. Reese, F. De Rossi, M. Saliba, U. S. Schubert, H. J. Snaith, S. D. Stranks, W. Tress, P. A. Troshin, V. Turkovic, S. Veenstra, I. Visoly-Fisher, A. Walsh, T. Watson, H. Xie, R. Yıldırım, S. M. Zakeeruddin, K. Zhu, and M. Lira-Cantu, "Consensus statement for stability assessment and reporting for perovskite photovoltaics based on isos procedures," *Nature Energy*, vol. 5, no. 1, pp. 35–49, 2020.

[8] M. Green, E. Dunlop, J. Hohl-Ebinger, M. Yoshita, N. Kopidakis, and X. Hao, "Solar cell efficiency tables (version 57)," *Progress in Photovoltaics: Research and Applications*, vol. 29, no. 1, pp. 3–15, 2020.

[9] N. Aristidou, I. Sanchez-Molina, T. Chotchuangchutchaval, M. Brown, L. Martinez, T. Rath, and S. A. Haque, "The role of oxygen in the degradation of methylammonium lead trihalide perovskite photoactive layers," *Angew Chem Int Ed Engl*, vol. 54, no. 28, pp. 8208–12, 2015.

[10] M. Abdelsamie, J. Xu, K. Bruening, C. J. Tassone, H. Steinrück, and M. F. Toney, "Impact of processing on structural and compositional evolution in mixed metal halide perovskites during film formation," *Advanced Functional Materials*, vol. 30, p. 2001752, 2020.

[11] N. Phung, A. Al-Ashouri, S. Meloni, A. Mattoni, S. Albrecht, E. L. Unger, A. Merdasa, and A. Abate, "The role of grain boundaries on ionic defect migration in metal halide perovskites," *Advanced Energy Materials*, vol. 10, no. 20, p. 1903735, 2020.

[12] A. M. A. Leguy, Y. Hu, M. Campoy-Quiles, M. I. Alonso, O. J. Weber, P. Azarhoosh, M. van Schilfgaarde, M. T. Weller, T. Bein, J. Nelson, P. Docampo, and P. R. F. Barnes, "Reversible hydration of ch3nh3pbi3 in films, single crystals, and solar cells," *Chemistry of Materials*, vol. 27, no. 9, pp. 3397–3407, 2015.

[13] R. L. Milot, G. E. Eperon, H. J. Snaith, M. B. Johnston, and L. M. Herz, "Temperature-dependent charge-carrier dynamics in ch3nh3pbi3 perovskite thin films," *Advanced Functional Materials*, vol. 25, no. 39, pp. 6218–6227, 2015.

[14] R. E. Beal, N. Z. Hagström, J. Barrier, A. Gold-Parker, R. Prasanna, K. A. Bush, D. Passarello, L. T. Schelhas, K. Brüning, C. J. Tassone, H.-G. Steinrück, M. D. McGehee, M. F. Toney, and A. F. Nogueira, "Structural origins of light-induced phase segregation in organic-inorganic halide perovskite photovoltaic materials," *Matter*, vol. 2, no. 1, pp. 207–219, 2020.

[15] Q. Wang, N. Phung, D. Di Girolamo, P. Vivo, and A. Abate, "Enhancement in lifespan of halide perovskite solar cells," *Energy Environmental Science*, vol. 12, no. 3, pp. 865–886, 2019.

[16] Z. Song, C. L. McElvany, A. B. Phillips, I. Celik, P. W. Krantz, S. C. Watthage, G. K. Liyanage, D. Apul, and M. J. Heben, "A technoeconomic analysis of perovskite solar module manufacturing with low-cost materials and techniques," *Energy Environmental Science*, vol. 10, no. 6, pp. 1297–1305, 2017.

[17] S. E. Sofia, H. Wang, A. Bruno, J. L. Cruz-Campa, T. Buonassisi, and I. M. Peters, "Roadmap for cost-effective, commercially-viable perovskite silicon tandems for the current and future pv market," *Sustainable Energy Fuels*, vol. 4, no. 2, pp. 852–862, 2020.

[18] S. Tang, S. Huang, G. J. Wilson, and A. Ho-Baillie, "Progress and opportunities for cs incorporated perovskite photovoltaics," *Trends in Chemistry*, vol. 2, no. 7, pp. 638–653, 2020.

[19] Y. An, C. A. R. Perini, J. Hidalgo, A.-F. Castro-Méndez, J. N. Vagott, R. Li, W. A. Saidi, S. Wang, X. Li, and J.-P. Correa-Baena, "Identifying high-performance and durable methylammonium-free lead halide perovskites via high-throughput synthesis and characterization," *Energy Environmental Science*, vol. 14, no. 12, pp. 6638–6654, 2021.

[20] T. Kirchartz, J. A. Márquez, M. Stolterfoht, and T. Unold, "Photoluminescence-based characterization of halide perovskites for photovoltaics," *Advanced Energy Materials*, vol. 10, p. 1904134, 2020.

[21] L. M. Herz, "Charge-carrier mobilities in metal halide perovskites: Fundamental mechanisms and limits," *ACS Energy Letters*, vol. 2, no. 7, pp. 1539–1548, 2017.

[22] N. J. Jeon, J. H. Noh, W. S. Yang, Y. C. Kim, S. Ryu, J. Seo, and S. I. Seok, "Compositional engineering of perovskite materials for high-performance solar cells," *Nature*, vol. 517, no. 7535, pp. 476–80, 2015.

[23] A. Sharenko and M. F. Toney, "Relationships between lead halide perovskite thin-film fabrication, morphology, and performance in solar cells," *J Am Chem Soc*, vol. 138, no. 2, pp. 463–70, 2016.

[24] M. L. Petrus, K. Schutt, M. T. Sirtl, E. M. Hutter, A. C. Closs, J. M. Ball, J. C. Bijleveld, A. Petrozza, T. Bein, T. J. Dingemans, T. J. Savenije, H. Snaith, and P. Docampo, "New generation hole transporting materials for perovskite solar cells: Amide-based small-molecules with nonconjugated backbones," *Advanced Energy Materials*, vol. 8, no. 32, p. 1801605, 2018.

[25] F. Bella, G. Griffini, J. Correa-Baena, G. Saracco, M. Graetzel, A. Hagfeldt, S. Turri, and C. Gerbaldi, "Improving efficiency and stability of perovskite solar cells with photocurable fluoropolymers," *Science*, vol. 354, no. 6309, pp. 203–206, 2016.

[26] N. Arora, M. I. Dar, A. Hinderhofer, F. Schreiber, S. M. Zakeeruddin, and M. Graetzel, "Perovskite solar cells with cuscn hole extraction layers yield stabilized efficiencies greater than 20no. 6364, pp. 768–771, 2017.

[27] M. Srivastava, J. M. Howard, T. Gong, M. Rebello Sousa Dias, and M. S. Leite, "Machine learning roadmap for perovskite photovoltaics," *J Phys Chem Lett*, vol. 12, no. 32, pp. 7866–7877, 2021.

[28] X. Ma, Z. Tao, Y. Wang, H. Yu, and Y. Wang, "Long short-term memory neural network for traffic speed prediction using remote microwave sensor data," *Transportation Research Part C: Emerging Technologies*, vol. 54, pp. 187–197, 2015.

[29] J. J. Titano, M. Badgeley, J. Schefflein, M. Pain, A. Su, M. Cai, N. Swinburne, J. Zech, J. Kim, J. Bederson, J. Mocco, B. Drayer, J. Lehar, S. Cho, A. Costa, and E. K. Oermann, "Automated deep-neural-network surveillance of cranial images for acute neurologic events," *Nature Medicine*, vol. 24, no. 9, pp. 1337–1341, 2018.

[30] D. Liu, J. Wang, and H. Wang, "Short-term wind speed forecasting based on spectral clustering and optimised echo state networks," *Renewable Energy*, vol. 78, pp. 599–608, 2015.

[31] Y. C. Sun, G. Szucs, and A. R. Brandt, "Solar pv output prediction from video streams using convolutional neural networks," *Energy Environmental Science*, vol. 11, no. 7, pp. 1811–1818, 2018.

[32] S. M. Ruffing and G. K. Venayagamoorthy, "Short to medium range time series prediction of solar irradiance using an echo state network," in *2009 15th International Conference on Intelligent System Applications to Power Systems*, pp. 1–6, IEEE.

[33] S. Morando, S. Jemei, R. Gouriveau, N. Zerhouni, and D. Hissel, "Fuel cells remaining useful lifetime forecasting using echo state network," in *2014 IEEE Vehicle Power and Propulsion Conference (VPPC)*, pp. 1–6, IEEE.

[34] D. Liu, W. Xie, H. Liao, and Y. Peng, "An integrated probabilistic approach to lithium-ion battery remaining useful life estimation," *IEEE Transactions on Instrumentation and Measurement*, vol. 64, no. 3, pp. 660–670, 2015.

[35] K. A. Severson, P. M. Attia, N. Jin, N. Perkins, B. Jiang, Z. Yang, M. H. Chen, M. Aykol, P. K. Herring, D. Fraggedakis, M. Z. Bazant, S. J. Harris, W. C. Chueh, and R. D. Braatz, "Data-driven prediction of battery cycle life before capacity degradation," *Nature Energy*, vol. 4, no. 5, pp. 383–391, 2019.

[36] Y. Zhang, Q. Tang, Y. Zhang, J. Wang, U. Stimming, and A. A. Lee, "Identifying degradation patterns of lithium ion batteries from impedance spectroscopy using machine learning," *Nature Communications*, vol. 11, no. 1, p. 1706, 2020.

[37] D. P. Tabor, L. M. Roch, S. K. Saikin, C. Kreisbeck, D. Sheberla, J. H. Montoya, S. Dwaraknath, M. Aykol, C. Ortiz, H. Tribukait, C. Amador-Bedolla, C. Brabec, B. Maruyama, K. A. Persson, and A. Aspuru-Guzik, "Accelerating the discovery of materials for clean energy in the era of smart automation," *Nature Reviews Materials*, vol. 3, pp. 5–20, 2018.

[38] J.-P. Correa-Baena, K. Hippalgaonkar, J. van Duren, S. Jaffer, V. R. Chandrasekhar, V. Stevanovic, C. Wadia, S. Guha, and T. Buonassisi, "Accelerating materials development via automation, machine learning, and high-performance computing," *Joule*, vol. 2, no. 8, pp. 1410–1420, 2018.

[39] S. Sun, N. T. P. Hartono, Z. D. Ren, F. Oviedo, A. M. Buscemi, M. Layurova, D. X. Chen, T. Ogunfunmi, J. Thapa, S. Ramasamy, C. Settens, B. L. DeCost, A. G. Kusne, Z. Liu, S. I. P. Tian, I. M. Peters, J. Correa-Baena, and T. Buonassisi, "Accelerating photovoltaic materials development via high-throughput experiments and machine-learning-assisted diagnosis," *Joule*, vol. 3, no. 6, pp. 1437–1451, 2019.

[40] E. Alpaydin, *Introduction to Machine Learning*. Cambridge, MA: The MIT Press, 4th ed., 2020.

[41] S. B. Kotsiantis, "Supervised machine learning: A review of classification techniques," *Informatica*, vol. 31, pp. 249–268, 2007.

[42] G. Hinton and T. J. Sejnowski, *Unsupervised Learning: Foundations of Neural Computation*. Cambridge, MA: The MIT Press, 1999.

[43] S. Haykin, *Neural Networks and Learning Machines*. Upper Saddle River, NJ: Pearson Prentice Hall, 3rd ed., 2009.

[44] R. Yamashita, M. Nishio, R. K. G. Do, and K. Togashi, "Convolutional neural networks: An overview and application in radiology," *Insights Imaging*, vol. 9, no. 4, pp. 611–629, 2018.

[45] H. Jaeger and H. Haas, "Harnessing nonlinearity: Predicting chaotic systems and saving energy in wireless communication," *Science*, vol. 304, no. 5667, pp. 78–80, 2004.

[46] S. Hochreiter and J. Schmidhuber, "Long short-term memory," *Neural computation*, vol. 9, no. 8, pp. 1735–1780, 1997.

[47] T. DeVries and G. W. Taylor, "Dataset augmentation in feature space." 2017.

[48] F. Oviedo, Z. Ren, S. Sun, C. Settens, Z. Liu, N. T. P. Hartono, S. Ramasamy, B. L. DeCost, S. I. P. Tian, G. Romano, A. Gilad Kusne, and T. Buonassisi, "Fast and interpretable classification of small x-ray diffraction datasets using data augmentation and deep neural networks," *npj Computational Materials*, vol. 5, no. 1, pp. 1–9, 2019.

[49] J. M. Howard, Q. Wang, E. Lee, R. Lahoti, T. Gong, M. Srivastava, A. Abate, and M. S. Leite, "Quantitative predictions of moisture-driven photo-emission dynamics in metal halide perovskites via machine learning," *arXiv e-prints*, 2020.

[50] T. G. Dietterich, *Ensemble Methods in Machine Learning*. Berlin: Springer, 2000.

[51] K. T. Butler, D. W. Davies, H. Cartwright, O. Isayev, and A. Walsh, "Machine learning for molecular and materials science," *Nature*, vol. 559, no. 7715, pp. 547–555, 2018.

[52] A. Y.-T. Wang, R. J. Murdock, S. K. Kauwe, A. O. Oliynyk, A. Gurlo, J. Brgoch, K. A. Persson, and T. D. Sparks, "Machine learning for materials scientists: An introductory guide toward best practices," *Chemistry of Materials*, vol. 32, no. 12, pp. 4954–4965, 2020.

[53] C. Chen, Y. Zuo, W. Ye, X. Li, Z. Deng, and S. P. Ong, "A critical review of machine learning of energy materials," *Advanced Energy Materials*, vol. 10, no. 8, p. 1903242, 2020.

[54] W. A. Saidi, W. Shadid, and I. E. Castelli, "Machine-learning structural and electronic properties of metal halide perovskites using a hierarchical convolutional neural network," *npj Computational Materials*, vol. 6, no. 1, pp. 1–7, 2020.

[55] J. M. Howard, E. M. Tennyson, B. R. A. Neves, and M. S. Leite, "Machine learning for perovskites' reap-rest-recovery cycle," *Joule*, vol. 3, no. 2, pp. 325–337, 2019.

[56] B. P. MacLeod, F. G. L. Parlane, T. D. Morrissey, F. Hase, L. M. Roch, K. E. Dettelbach, R. Moreira, L. P. E. Yunker, M. B. Rooney, J. R. Deeth, V. Lai, G. J. Ng, H. Situ, R. H. Zhang, M. S. Elliot, T. H. Haley, D. J. Dvorak, A. Aspuru-Guzik, J. E. Hein, and C. P. Berlinguette, "Self-driving laboratory for accelerated discovery of thin-film materials," *Science Advances*, vol. 6, p. eaaz8867, 2020.

[57] M. Lira-Cantú, "Perovskite solar cells: Stability lies at interfaces," *Nature Energy*, vol. 2, no. 7, p. 17115, 2017.

[58] C. Kim, G. Pilania, and R. Ramprasad, "Machine learning assisted predictions of intrinsic dielectric breakdown strength of abx3 perovskites," *The Journal of Physical Chemistry C*, vol. 120, no. 27, pp. 14575–14580, 2016.

[59] J. Schmidt, J. Shi, P. Borlido, L. Chen, S. Botti, and M. A. L. Marques, "Predicting the thermodynamic stability of solids combining density functional theory and machine learning," *Chemistry of Materials*, vol. 29, no. 12, pp. 5090–5103, 2017.

[60] Y. Yu, X. Tan, S. Ning, and Y. Wu, "Machine learning for understanding compatibility of organic–inorganic hybrid perovskites with post-treatment amines," *ACS Energy Letters*, vol. 4, no. 2, pp. 397–404, 2019.

[61] J. A. Christians, P. A. Miranda Herrera, and P. V. Kamat, "Transformation of the excited state and photovoltaic efficiency of ch3nh3pbi3 perovskite upon controlled exposure to humidified air," *J Am Chem Soc*, vol. 137, no. 4, pp. 1530–8, 2015.

[62] M. I. Asghar, J. Zhang, H. Wang, and P. D. Lund, "Device stability of perovskite solar cells – a review," *Renewable and Sustainable Energy Reviews*, vol. 77, pp. 131–146, 2017.

[63] P. Raccuglia, K. C. Elbert, P. D. F. Adler, C. Falk, M. B. Wenny, A. Mollo, M. Zeller, S. A. Friedler, J. Schrier, and A. J. Norquist, "Machine-learning-assisted materials discovery using failed experiments," *Nature*, vol. 533, pp. 73–77, 2016.

[64] E. J. Topol, "High-performance medicine: The convergence of human and artificial intelligence," *Nature Medicine*, vol. 25, no. 1, pp. 44–56, 2019.

[65] K. Takahashi, L. Takahashi, I. Miyazato, and Y. Tanaka, "Searching for hidden perovskite materials for photovoltaic systems by combining data science and first principle calculations," *ACS Photonics*, vol. 5, no. 3, pp. 771–775, 2018.

[66] G. Pilania, A. Mannodi-Kanakkithodi, B. P. Uberuaga, R. Ramprasad, J. E. Gubernatis, and T. Lookman, "Machine learning bandgaps of double perovskites," *Scientific Reports*, vol. 6, p. 19375, 2016.

[67] J. Li, B. Pradhan, S. Gaur, and J. Thomas, "Predictions and strategies learned from machine learning to develop high-performing perovskite solar cells," *Advanced Energy Materials*, vol. 9, no. 46, p. 1901891, 2019.

[68] Q. Xu, Z. Li, M. Liu, and W. J. Yin, "Rationalizing perovskites data for machine learning and materials design," *J. Phys. Chem. Lett.*, vol. 9, pp. 6948–6954, 2018.

[69] S. G. Javed, A. Khan, A. Majid, A. M. Mirza, and J. Bashir, "Lattice constant prediction of orthorhombic abo3 perovskites using support vector machines," *Computational Materials Science*, vol. 39, no. 3, pp. 627–634, 2007.

[70] S. Chen, Y. Hou, H. Chen, X. Tang, S. Langner, N. Li, T. Stubhan, I. Levchuk, E. Gu, A. Osvet, and C. J. Brabec, "Exploring the stability of novel wide bandgap perovskites by a robot based high throughput approach," *Advanced Energy Materials*, vol. 8, no. 6, p. 1701543, 2018.

[71] R. W. Epps, M. S. Bowen, A. A. Volk, K. Abdel-Latif, S. Han, K. G. Reyes, A. Amassian, and M. Abolhasani, "Artificial chemist: An autonomous quantum dot synthesis bot," *Adv Mater*, vol. 32, no. 30, p. e2001626, 2020.

[72] K. Higgins, S. M. Valleti, M. Ziatdinov, S. V. Kalinin, and M. Ahmadi, "Chemical robotics enabled exploration of stability in multicomponent lead halide perovskites via machine learning," *ACS Energy Letters*, vol. 5, no. 11, pp. 3426–3436, 2020.

[73] T. Leijtens, K. Bush, R. Cheacharoen, R. Beal, A. Bowring, and M. D. McGehee, "Towards enabling stable lead halide perovskite solar cells; interplay between structural, environmental, and thermal stability," *J. Mater. Chem. A*, vol. 5, no. 23, pp. 11483–11500, 2017.

[74] T. A. Berhe, W.-N. Su, C.-H. Chen, C.-J. Pan, J.-H. Cheng, H.-M. Chen, M.-C. Tsai, L.-Y. Chen, A. A. Dubale, and B.-J. Hwang, "Organometal halide perovskite solar cells: Degradation and stability," *Energy Environmental Science*, vol. 9, no. 2, pp. 323–356, 2016.

[75] K. Domanski, E. A. Alharbi, A. Hagfeldt, M. Grätzel, and W. Tress, "Systematic investigation of the impact of operation conditions on the degradation behaviour of perovskite solar cells," *Nature Energy*, vol. 3, no. 1, pp. 61–67, 2018.

[76] R. J. Stoddard, W. A. Dunlap-Shohl, H. Qiao, Y. Meng, W. F. Kau, and H. W. Hillhouse, "Forecasting the decay of hybrid perovskite performance using optical transmittance or reflected dark-field imaging," *ACS Energy Letters*, vol. 5, no. 3, pp. 946–954, 2020.

[77] J. M. Howard, E. M. Tennyson, S. Barik, R. Szostak, E. Waks, M. F. Toney, A. F. Nogueira, B. R. A. Neves, and M. S. Leite, "Humidity-induced photoluminescence hysteresis in variable cs/br ratio hybrid perovskites," *J. Phys. Chem. Lett.*, vol. 9, no. 12, pp. 3463–3469, 2018.

[78] G. Forestier, F. Petitjean, H. A. Dau, G. I. Webb, and E. Keogh, "Generating synthetic time series to augment sparse datasets," in *2017 IEEE International Conference on Data Mining (ICDM)*, pp. 865–870, IEEE.

[79] C. Oh, S. Han, and J. Jeong, "Time-series data augmentation based on interpolation," *Procedia Computer Science*, vol. 170, pp. 64–71, 2020.

[80] T. Eslami, V. Mirjalili, A. Fong, A. R. Laird, and F. Saeed, "Asd-diagnet: A hybrid learning approach for detection of autism spectrum disorder using fmri data," *Front. Neuroinform.*, vol. 13, p. 70, 2019.

[81] B. K. Iwana and S. Uchida, "An empirical survey of data augmentation for time series classification with neural networks," *arXiv e-prints*, 2020.

[82] G. Grancini, C. Roldán-Carmona, I. Zimmermann, E. Mosconi, X. Lee, D. Martineau, S. Narbey, F. Oswald, F. De Angelis, M. Graetzel, and M. K. Nazeeruddin, "One-year stable perovskite solar cells by 2d/3d interface engineering," *Nature Communications*, vol. 8, p. 15684, 2017.

[83] J. A. Christians, P. Schulz, J. S. Tinkham, T. H. Schloemer, S. P. Harvey, B. J. Tremolet de Villers, A. Sellinger, J. J. Berry, and J. M. Luther, "Tailored interfaces of unencapsulated perovskite solar cells for >1,000 hour operational stability," *Nature Energy*, vol. 3, no. 1, pp. 68–74, 2018.

[84] C. Tao, S. Neutzner, L. Colella, S. Marras, A. R. Srimath Kandada, M. Gandini, M. D. Bastiani, G. Pace, L. Manna, M. Caironi, C. Bertarelli, and A. Petrozza, "17.6planar perovskite solar cells," *Energy Environmental Science*, vol. 8, no. 8, pp. 2365–2370, 2015.

[85] M. Chen, M. G. Ju, H. F. Garces, A. D. Carl, L. K. Ono, Z. Hawash, Y. Zhang, T. Shen, Y. Qi, R. L. Grimm, D. Pacifici, X. C. Zeng, Y. Zhou, and N. P. Padture, "Highly stable and efficient all-inorganic lead-free perovskite solar cells with native-oxide passivation," *Nature Communications*, vol. 10, no. 1, p. 16, 2019.

[86] W. Tress, K. Domanski, B. Carlsen, A. Agarwalla, E. A. Alharbi, M. Graetzel, and A. Hagfeldt, "Performance of perovskite solar cells under simulated temperature-illumination real-world operating conditions," *Nature Energy*, vol. 4, no. 7, pp. 568–574, 2019.

[87] R. Guo, M. V. Khenkin, G. E. Arnaoutakis, N. A. Samoylova, J. Barbé, H. K. H. Lee, W. C. Tsoi, and E. A. Katz, "Initial stages of photodegradation of mapbi3 perovskite: Accelerated aging with concentrated sunlight," *Solar RRL*, vol. 4, no. 2, p. 1900270, 2019.

[88] G. Divitini, S. Cacovich, F. Matteocci, L. Cinà, A. Di Carlo, and C. Ducati, "In situ observation of heat-induced degradation of perovskite solar cells," *Nature Energy*, vol. 1, no. 2, p. 15012, 2016.

[89] P. Holzhey, P. Yadav, S.-H. Turren-Cruz, A. Ummadisingu, M. Grätzel, A. Hagfeldt, and M. Saliba, "A chain is as strong as its weakest link – stability study of mapbi3 under light and temperature," *Materials Today*, vol. 29, pp. 10–19, 2019.

[90] D. Bryant, N. Aristidou, S. Pont, I. Sanchez-Molina, T. Chotchunangatchaval, S. Wheeler, J. R. Durrant, and S. A. Haque, "Light and oxygen induced degradation limits the operational stability of methylammonium lead triiodide perovskite solar cells," *Energy Environmental Science*, vol. 9, no. 5, pp. 1655–1660, 2016.

[91] J. Huang, S. Tan, P. D. Lund, and H. Zhou, "Impact of h2o on organic–inorganic hybrid perovskite solar cells," *Energy Environ. Sci.*, vol. 10, no. 11, pp. 2284–2311, 2017.

[92] M. C. Schubert, L. E. Mundt, D. Walter, A. Fell, and S. W. Glunz, "Spatially resolved performance analysis for perovskite solar cells," *Advanced Energy Materials*, p. 1904001, 2020.

[93] L. Collins, M. Ahmadi, J. Qin, Y. Liu, O. S. Ovchinnikova, B. Hu, S. Jesse, and S. V. Kalinin, "Time resolved surface photovoltage measurements using a big data capture approach to kpfm," *Nanotechnology*, vol. 29, no. 44, p. 445703, 2018.

[94] J. Kirman, A. Johnston, D. A. Kuntz, M. Askerka, Y. Gao, P. Todorović, D. Ma, G. G. Privé, and E. H. Sargent, "Machine-learning-accelerated perovskite crystallization," *Matter*, vol. 2, no. 4, pp. 938–947, 2020.

[95] N. Taherimakhsousi, B. P. MacLeod, F. G. L. Parlane, T. D. Morrissey, E. P. Booker, K. E. Dettelbach, and C. P. Berlinguette, "Quantifying defects in thin films using machine vision," *npj Computational Materials*, vol. 6, no. 1, p. 111, 2020.

[96] N. Shahcheraghi, V. J. Keast, A. R. Gentle, M. D. Arnold, and M. B. Cortie, "Anomalously strong plasmon resonances in aluminium bronze by modification of the electronic density-of-states," *J. Phys. Condens. Matter*, vol. 28, no. 40, p. 405501, 2016.

[97] S. K. Suram, Y. Xue, J. Bai, R. Le Bras, B. Rappazzo, R. Bernstein, J. Bjorck, L. Zhou, R. B. van Dover, C. P. Gomes, and J. M. Gregoire, "Automated phase mapping with agilefd and its application to light absorber discovery in the v-mn-nb oxide system," *ACS Comb. Sci.*, vol. 19, no. 1, pp. 37–46, 2017.

[98] J. W. Bai, Y. X. Xue, J. Bjorck, R. Le Bras, B. Rappazzo, R. Bernstein, S. K. Suram, R. B. van Dover, J. M. Gregoire, and C. P. Gomes, "Phase-mapper: Accelerating materials discovery with ai," *AI Magazine*, vol. 39, no. 1, pp. 15–26, 2018.

[99] O. Voznyy, L. Levina, J. Z. Fan, M. Askerka, A. Jain, M.-J. Choi, O. Ouellette, P. Todorović, L. K. Sagar, and E. H. Sargent, "Machine learning accelerates discovery of optimal colloidal quantum dot synthesis," *ACS Nano*, vol. 13, no. 10, pp. 11122–11128, 2019.

[100] F. Ren, L. Ward, T. Williams, K. J. Laws, C. Wolverton, J. Hattrick-Simpers, and A. Mehta, "Accelerated discovery of metallic glasses through iteration of machine learning and high-throughput experiments," *Science Advances*, vol. 4, no. 4, p. eaaq1566, 2018.

[101] K. Yao, R. Unni, and Y. Zheng, "Intelligent nanophotonics: Merging photonics and artificial intelligence at the nanoscale," *Nanophotonics*, vol. 8, no. 3, pp. 339–366, 2019.

[102] W. Ma, F. Cheng, and Y. Liu, "Deep-learning-enabled on-demand design of chiral metamaterials," *ACS Nano*, vol. 12, no. 6, pp. 6326–6334, 2018.

[103] K. P. Goetz, A. D. Taylor, F. Paulus, and Y. Vaynzof, "Shining light on the photoluminescence properties of metal halide perovskites," *Advanced Functional Materials*, vol. 30, no. 23, 2020.

[104] Y. Yamada, T. Nakamura, M. Endo, A. Wakamiya, and Y. Kanemitsu, "Photocarrier recombination dynamics in perovskite ch3nh3pbi3 for solar cell applications," *J Am Chem Soc*, vol. 136, no. 33, pp. 11610–3, 2014.

[105] S. D. Stranks, V. M. Burlakov, T. Leijtens, J. M. Ball, A. Goriely, and H. J. Snaith, "Recombination kinetics in organic-inorganic perovskites: Excitons, free charge, and subgap states," *Physical Review Applied*, vol. 2, no. 3, 2014.

[106] S. Meloni, G. Palermo, N. Ashari-Astani, M. Grätzel, and U. Rothlisberger, "Valence and conduction band tuning in halide perovskites for solar cell applications," *Journal of Materials Chemistry A*, vol. 4, no. 41, pp. 15997–16002, 2016.

[107] G. E. Eperon, S. D. Stranks, C. Menelaou, M. B. Johnston, L. M. Herz, and H. J. Snaith, "Formamidinium lead trihalide: a broadly tunable perovskite for efficient planar heterojunction solar cells," *Energy Environmental Science*, vol. 7, no. 3, 2014.

[108] Z. Li, M. Yang, J.-S. Park, S.-H. Wei, J. J. Berry, and K. Zhu, "Stabilizing perovskite structures by tuning tolerance factor: Formation of formamidinium and cesium lead iodide solid-state alloys," *Chemistry of Materials*, vol. 28, no. 1, pp. 284–292, 2015.

[109] A. Amat, E. Mosconi, E. Ronca, C. Quarti, P. Umari, M. K. Nazeeruddin, M. Gratzel, and F. De Angelis, "Cation-induced band-gap tuning in organohalide perovskites: interplay of spin-orbit coupling and octahedra tilting," *Nano Lett*, vol. 14, no. 6, pp. 3608–16, 2014.

[110] R. Comin, G. Walters, E. S. Thibau, O. Voznyy, Z.-H. Lu, and E. H. Sargent, "Structural, optical, and electronic studies of wide-bandgap lead halide perovskites," *Journal of Materials Chemistry C*, vol. 3, no. 34, pp. 8839–8843, 2015.

[111] J. H. Noh, S. H. Im, J. H. Heo, T. N. Mandal, and S. I. Seok, "Chemical management for colorful, efficient, and stable inorganic-organic hybrid nanostructured solar cells," *Nano Lett*, vol. 13, no. 4, pp. 1764–9, 2013.

[112] W. Rehman, R. L. Milot, G. E. Eperon, C. Wehrenfennig, J. L. Boland, H. J. Snaith, M. B. Johnston, and L. M. Herz, "Charge-carrier dynamics and mobilities in formamidinium lead mixed-halide perovskites," *Adv Mater*, vol. 27, no. 48, pp. 7938–44, 2015.

[113] B. Chen, P. N. Rudd, S. Yang, Y. Yuan, and J. Huang, "Imperfections and their passivation in halide perovskite solar cells," *Chem Soc Rev*, vol. 48, no. 14, pp. 3842–3867, 2019.

[114] M. A. Green, "Silicon solar cells: state of the art," *Philos Trans A Math Phys Eng Sci*, vol. 371, no. 1996, p. 20110413, 2013.

[115] D. Luo, R. Su, W. Zhang, Q. Gong, and R. Zhu, "Minimizing non-radiative recombination losses in perovskite solar cells," *Nature Reviews Materials*, vol. 5, no. 1, pp. 44–60, 2019.

[116] A. Zakutayev, C. M. Caskey, A. N. Fioretti, D. S. Ginley, J. Vidal, V. Stevanovic, E. Tea, and S. Lany, "Defect tolerant semiconductors for solar energy conversion," *J Phys Chem Lett*, vol. 5, no. 7, pp. 1117–25, 2014.

[117] M. H. Du, "Density functional calculations of native defects in ch3nh3pbi3: Effects of spin-orbit coupling and self-interaction error," *J Phys Chem Lett*, vol. 6, no. 8, pp. 1461–6, 2015.

[118] J. Kang and L. W. Wang, "High defect tolerance in lead halide perovskite cspbbr3," *J Phys Chem Lett*, vol. 8, no. 2, pp. 489–493, 2017.

[119] Y. Rakita, I. Lubomirsky, and D. Cahen, "When defects become 'dynamic': halide perovskites: a new window on materials?," *Materials Horizons*, vol. 6, no. 7, pp. 1297–1305, 2019.

[120] S. Rudin, T. L. Reinecke, and B. Segall, "Temperature-dependent exciton linewidths in semiconductors," *Phys Rev B Condens Matter*, vol. 42, no. 17, pp. 11218–11231, 1990.

[121] U.-G. Jong, C.-J. Yu, G.-C. Ri, A. P. McMahon, N. Harrison, P. R. F. Barnes, and A. Walsh, "Influence of water intercalation and hydration on chemical decomposition and ion transport in methylammonium lead halide perovskites," *Journal of Materials Chemistry A*, vol. 6, no. 3, pp. 1067–1074, 2018.

[122] Y. Tian, M. Peter, E. Unger, M. Abdellah, K. Zheng, T. Pullerits, A. Yartsev, V. Sundstrom, and I. G. Scheblykin, "Mechanistic insights into perovskite photoluminescence enhancement: light curing with oxygen can boost yield thousandfold," *Phys Chem Chem Phys*, vol. 17, no. 38, pp. 24978–87, 2015.

[123] H.-H. Fang, S. Adjokatse, H. Wei, J. Yang, G. R. Blake, J. Huang, J. Even, and M. A. Loi, "Ultrahigh sensitivity of methylammonium lead tribromide perovskite single crystals to environmental gases," *Science Advances*, vol. 2, no. 7, p. e1600534, 2016.

[124] D. Meggiolaro, S. G. Motti, E. Mosconi, A. J. Barker, J. Ball, C. Andrea Riccardo Perini, F. Deschler, A. Petrozza, and F. De Angelis, "Iodine chemistry determines the defect tolerance of lead-halide perovskites," *Energy Environmental Science*, vol. 11, no. 3, pp. 702–713, 2018.

[125] P. Nikolaev, D. Hooper, F. Webber, R. Rao, K. Decker, M. Krein, J. Poleski, R. Barto, and B. Maruyama, "Autonomy in materials research: a case study in carbon nanotube growth," *npj Computational Materials*, vol. 2, no. 1, 2016.

[126] Y. An, J. Hidalgo, C. A. R. Perini, A.-F. Castro-Méndez, J. N. Vagott, K. Bairley, S. Wang, X. Li, and J.-P. Correa-Baena, "Structural stability of formamidinium- and cesium-based halide perovskites," *ACS Energy Letters*, vol. 6, no. 5, pp. 1942–1969, 2021.

[127] M. Saliba, T. Matsui, J. Y. Seo, K. Domanski, J. P. Correa-Baena, M. K. Nazeeruddin, S. M. Zakeeruddin, W. Tress, A. Abate, A. Hagfeldt, and M. Gratzel, "Cesium-containing triple cation perovskite solar cells: improved stability, reproducibility and high efficiency," *Energy Environ Sci*, vol. 9, no. 6, pp. 1989–1997, 2016.

[128] M. Gratzel, "The rise of highly efficient and stable perovskite solar cells," *Acc Chem Res*, vol. 50, no. 3, pp. 487–491, 2017.

[129] Y. Wang, X. Quintana, J. Kim, X. Guan, L. Hu, C.-H. Lin, B. T. Jones, W. Chen, X. Wen, H. Gao, and T. Wu, "Phase segregation in inorganic mixed-halide perovskites: from phenomena to mechanisms," *Photonics Research*, vol. 8, no. 11, 2020.

[130] W. Ahmad, J. Khan, G. Niu, and J. Tang, "Inorganic cspbi3perovskite-based solar cells: A choice for a tandem device," *Solar RRL*, vol. 1, no. 7, 2017.

[131] J.-W. Lee, D.-H. Kim, H.-S. Kim, S.-W. Seo, S. M. Cho, and N.-G. Park, "Formamidinium and cesium hybridization for photo- and moisture-stable perovskite solar cell," *Advanced Energy Materials*, vol. 5, no. 20, 2015.

[132] J. Correa-Baena, M. Saliba, T. Buonassisi, M. Graetzel, A. Abate, W. Tress, and A. Hagfeldt, "Promises and challenges of perovskite solar cells," *Science*, vol. 358, pp. 739–744, 2017.

[133] Y. P. Varshni, "Temperature dependence of the energy gap in semiconductors," *Physica*, vol. 34, no. 1, pp. 149–154, 1967.

[134] J. Even, L. Pedesseau, M. A. Dupertuis, J. M. Jancu, and C. Katan, "Electronic model for self-assembled hybrid organic/perovskite semiconductors: Reverse band edge electronic states ordering and spin-orbit coupling," *Physical Review B*, vol. 86, no. 20, 2012.

[135] J. Y. Yang and M. Hu, "Temperature-induced large broadening and blue shift in the electronic band structure and optical absorption of methylammonium lead iodide perovskite," *J Phys Chem Lett*, vol. 8, no. 16, pp. 3720–3725, 2017.

[136] J. Troughton, N. Gasparini, and D. Baran, "Cs0.15fa0.85pbi3 perovskite solar cells for concentrator photovoltaic applications," *Journal of Materials Chemistry A*, vol. 6, no. 44, pp. 21913–21917, 2018.

[137] G. Niu, H. Yu, J. Li, D. Wang, and L. Wang, "Controlled orientation of perovskite films through mixed cations toward high performance perovskite solar cells," *Nano Energy*, vol. 27, pp. 87–94, 2016.

[138] N. C. Park, W. W. Oh, and D. H. Kim, "Effect of temperature and humidity on the degradation rate of multicrystalline silicon photovoltaic module," *International Journal of Photoenergy*, vol. 2013, pp. 1–9, 2013.

[139] S. Mekhilef, R. Saidur, and M. Kamalisarvestani, "Effect of dust, humidity and air velocity on efficiency of photovoltaic cells," *Renewable and Sustainable Energy Reviews*, vol. 16, no. 5, pp. 2920–2925, 2012.

[140] 2020.

[141] L. Meng, J. You, and Y. Yang, "Addressing the stability issue of perovskite solar cells for commercial applications," *Nature Communications*, vol. 9, no. 1, p. 5265, 2018.

[142] M. A. Chitsazan, M. Sami Fadali, and A. M. Trzynadlowski, "Wind speed and wind direction forecasting using echo state network with nonlinear functions," *Renewable Energy*, vol. 131, pp. 879–889, 2019.

[143] H. Hu, L. Wang, L. Peng, and Y.-R. Zeng, "Effective energy consumption forecasting using enhanced bagged echo state network," *Energy*, vol. 193, p. 116778, 2020.

[144] M. Lukoševičius, *A Practical Guide to Applying Echo State Networks*, pp. 659–686. Berlin, Heidelberg: Springer Berlin Heidelberg, 2012.

[145] G. Tunnicliffe Wilson, "Time series analysis: Forecasting and control,5th edition, by george e. p. box, gwilym m. jenkins, gregory c. reinsel and greta m. ljung, 2015. published by john wiley and sons inc., hoboken, new jersey, pp. 712. isbn: 978-1-118-67502-1," *Journal of Time Series Analysis*, vol. 37, pp. n/a–n/a, 2016.

[146] S. I. Vagropoulos, G. I. Chouliaras, E. G. Kardakos, C. K. Simoglou, and A. G. Bakirtzis, "Comparison of sarimax, sarima, modified sarima and ann-based models for short-term pv generation forecasting," in *2016 IEEE International Energy Conference (ENERGYCON)*, pp. 1–6.

[147] J. Contreras, R. Espinola, F. J. Nogales, and A. J. Conejo, "Arima models to predict next-day electricity prices," *IEEE Transactions on Power Systems*, vol. 18, no. 3, pp. 1014–1020, 2003.

[148] P. Newbold, "Arima model building and the time series analysis approach to forecasting," *Journal of Forecasting*, vol. 2, no. 1, pp. 23–35, 1983.

[149] S. C. Hillmer and G. C. Tiao, "An arima-model-based approach to seasonal adjustment," *Journal of the American Statistical Association*, vol. 77, no. 377, pp. 63–70, 1982.

[150] K. Cho, B. v. Merrienboer, Gülçehre, D. Bahdanau, F. Bougares, H. Schwenk, and Y. Bengio, "Learning phrase representations using rnn encoder decoder for statistical machine translation," in *EMNLP*.